INFORMATION TO USERS

The most advanced technology has been used to photograph and reproduce this manuscript from the microfilm master. UMI films the text directly from the original or copy submitted. Thus, some thesis and dissertation copies are in typewriter face, while others may be from any type of computer printer.

The quality of this reproduction is dependent upon the quality of the copy submitted. Broken or indistinct print, colored or poor quality illustrations and photographs, print bleedthrough, substandard margins, and improper alignment can adversely affect reproduction.

In the unlikely event that the author did not send UMI a complete manuscript and there are missing pages, these will be noted. Also, if unauthorized copyright material had to be removed, a note will indicate the deletion.

Oversize materials (e.g., maps, drawings, charts) are reproduced by sectioning the original, beginning at the upper left-hand corner and continuing from left to right in equal sections with small overlaps. Each original is also photographed in one exposure and is included in reduced form at the back of the book.

Photographs included in the original manuscript have been reproduced xerographically in this copy. Higher quality 6" x 9" black and white photographic prints are available for any photographs or illustrations appearing in this copy for an additional charge. Contact UMI directly to order.

UMI

University Microfilms International
A Bell & Howell Information Company
300 North Zeeb Road, Ann Arbor, MI 48106-1346 USA
313/761-4700 800/521-0600

Order Number 9108122

Growth and electronic properties of selected bimetallic interfaces

Jiang, Liqiang, Ph.D.

City University of New York, 1990

U·M·I
300 N. Zeeb Rd.
Ann Arbor, MI 48106

17

GROWTH AND ELECTRONIC PROPERTIES OF SELECTED BIMETALLIC INTERFACES

by

Liqiang Jiang

A dissertation submitted to the Graduate Faculty in Physics in partial fulfillment of the requirement for the degree of Doctor of Philosophy, City University of New York.

1990

This manuscript has been read and accepted for the Graduate Faculty in Physics in satisfaction of the dissertation requirement for the degree of Doctor of Philosophy.

Arthur C. Damask

September 7, 1990
Date

Arthur C. Damask
Chair of Examining Committee

September 11, 1990
Date

Joseph Krieger Joseph Krieger
Executive Officer

Myron Strongin Myron Strongin

Leonard I. Roellig

Marten L. denBoer

Steve M. Heald Steve M Heald

Supervisory Committee

The City University of New York

ABSTRACT

GROWTH AND ELECTRONIC PROPERTIES OF SELECTED BIMETALLIC INTERFACES

Liqiang Jiang

Advisor: Dr. Myron Strongin

The growth and electronic properties of selected bimetallic interfaces are studied using AES, LEED, LEIS and photoemission. A more systematic understanding of complex interfacial phenomena is obtained by simple models based on energetics. It is found that Rh agglomerates on Ta(110) but grows layer by layer on Mo(110) which has less lattice mismatch. A transition from the Kurdjumov-Sachs to the Nishiyama-Wassermann orientation is observed for the first time during the growth of Rh(111) monolayer on Mo(110). It is demonstrated that alloying may occur even at 300 K if the surface energy of the overlayer is higher than the substrate and the bonding of the metal pair is strong, as in the case of Pd/Al and Nb/Pd.

The direction of electronic charge transfer between an adatom and a metallic substrate is shown to be determined by the sign of $J=(I+A)/2-\phi$, where A and I are the affinity and ionization level of the adatom and ϕ is the substrate work function. This criterion enables a unified understanding of the work function trends of the various systems studied in this thesis as well as other systems that have not been explained previously. Although both Nb and Pd surfaces readily adsorb CO, the alloy surface obtained by depositing 1 ML Nb on Pd is found to be inert to CO adsorption at 300 K. Further evidence is found for the strong correlation between the density of states near the Fermi level and CO adsorption, or more generally, catalytic properties of bimetallic systems. Together this work has lead to deeper insight into interface formation and the crucial role of electronic structure in surface chemistry.

Acknowledgements

I gratefully thank my advisor Myron Strongin for his guidance, research support and for offering me many stimulating suggestions while encouraging a high level of independence.

I would like to thank Arthur Damask and his family for many valuable advices and great concern for my education and personal growth. I am also indebted to members of my supervisory committee for their helpful insights.

I benefited a lot from many discussions and collaborations with Mark Ruckman who also read and made many critical suggestions to most of my writings.

Special thanks go to Fran Loeb who has been always giving me so much help for all kinds of problems throughout this thesis work.

I am also grateful to Arthur Viescus and Steve Hulbert for their experted assistance in computer programming, and to John and Ray Raynis for their excellent technical support.

I cannot come to this far without the support of my family. My wife Wenrui Geng has made most of the drawings in this thesis and has always been a great inspiration in my life. My parents, my sister and my brothers have put my education as a family priority over the last decade. I am immensely grateful to all of you for your love and encouragement.

CONTENTS

List of Tables

List of Figures

Chapter 1. Introduction

The primary objective of this thesis is to gain a more systematic understanding about the factors controlling thin film growth, the geometrical and electronic structure of bimetallic interfaces and their relationship with chemisorptive and catalytic properties. This is accomplished by combining various surface-sensitive techniques along with a high pressure reaction cell to study several carefully selected and *in-situ* prepared systems.

The introduction of surfaces and interfaces breaks the three-dimensional periodicity of solids in one direction and leads to structural changes and localized electronic states. Gaining a proper understanding of these effects is not only of academic interest in low-dimensional physics at a fundamental level, but is also important in modifying the surface to obtain desired magnetic, catalytic or corrosion resistive properties. The behavior of a single interface has great implications for the formation of artificial superlattices which have recently received increasing interest due to their unusual properties, and opened up new possibilities for physics, chemistry, and materials science. For uniformity, layer-by-layer [Frank-van der Merwe (FM)] growth is desirable. However, growth studies reveal that many materials will not grow in FM mode on certain other layers, especially for the growth of material B on material A when A grows in FM mode on B. The information about these limitations in "atomic engineering" can therefore provide guidance for the design and fabrication of exotic artificial multilayer or superlattice devices.

Starting with the pioneering work of Frank and van der Merwe,[1] studies of the energetics of epitaxial growth, including phenomenological methods, Monte Carlo simulations, and molecular-dynamics simulations, have provided an important basis for dealing with growth modes, relative orientation, stability, and various other structural properties pertaining to surfaces, interfaces, and superlattices.[2] The predictive power of these models are often limited by the fact that many parameters involved in the theories are not known very well. Recently first principles calculations have been performed for Pd-Nb and Ag-Nb systems and the behavior of Pd and Ag on Nb(110) have been understood successfully.[3] On the other hand, controversial theoretical predictions are common place. For example, a surface state of Rh(100) is predicted at 0.2 eV below E_F by Gay *et al.*[4] but at 1.5 eV above E_F by Feibelman *et al.*[5] Recent experimental work[6] confirmed the former. Clearly further experimental work is needed to provide additional data for the refining of theory. Although theories seem very helpful in terms of understanding what has happened, the lack of a unifying theme makes it still difficult, at present, to predict the structural and electronic properties of a given interface, and each system needs individual attention. A series of experiments have been designed in this thesis to gain new insight into the nature of bimetallic interface, and to test and challenge various ideas and theories which might explain and predict the properties of surfaces and thin films.

The structure and electronic properties of an overlayer are determined by the reduced dimensionality and the overlayer-substrate interaction. The Pd/Al system has attracted the interest of many researchers because the lack of a strong overlayer-substrate *d*-*d* interaction suggests that it might be a model two-dimensional system. Several reports[7] have appeared in the literature claiming that a Pd monolayer on Al resembles an unsupported Pd layer. The *d* shell of Pd atom is filled but the *d* band in Pd metal is not filled because of the crossing of Pd 4*d* and 5*s* levels due to the Pd-Pd interaction in the solid. The empty substrate *d* band in the Pd/Al system allows a close examination of the evolution of the Pd *d* band as Pd grows from a single atom to a three dimensional solid.

The Pd on Nb(110) or Ta(110) system has been studied in some detail during the last decade and interesting hydrogen uptake,[8] structural and electronic[9] properties have been found. This thesis extends those earlier studies in three directions. First, the deuteration reaction of propylene (C_3H_6) and D-H exchange over Pd/Ta(110) at relatively high pressures is performed to study the catalytic properties and their relationship with geometrical and electronic structure. Second, the reverse system Nb/Pd is investigated. As mentioned earlier, high quality superlattice formation requires FM growth of both A on B and B on A. However, most publications have been dealt with late and noble transition metals on early transition (refractory) metals. The reverse are rarely studied, especially the high Z refractory metal overlayers, probably because of the difficulty in preparing clean thin films of these high-melting point and highly reactive materials. Third, the growth of Rh on Ta(110) and Mo(110) is studied to investigate the trends in electronic properties and the effects of lattice mismatch. These topics have been approached experimentally by using a combination of Auger electron spectroscopy (AES), low energy electron diffraction (LEED), low energy ion scattering (LEIS) and photoemission spectroscopy (PES). In addition to high pressure reactions, the adsorption of CO has been used as a probe of the surface activity.

This thesis is organized as follows. First, I will give an overview of the experimental techniques, followed by a discussion of the basic theories of the growth of thin film and the orientations at fcc(111)/bcc(110) interfaces. I will also introduce a simple criterion for the direction of electronic charge transfer between an adatom and a metallic substrate which will be used throughout the thesis to understand the initial work function changes due to adsorption. Then I will move on to the studies of Pd/Al which disprove the previous conclusion[7] of SK growth for this system and demonstrate that alloying may occur even at room temperature when a high surface energy metal is grown on a low surface energy metal and the bonding of the metal pair is strong. This idea is further supported by the alloying of Nb/Pd(111), which is also understood by comparing to the first principles calculations available for this system.[3] The dominant role of electronic effects on chemisorptive properties is stressed by comparing the similar electronic structure and weakened CO adsorption of the alloy surface obtained by depositing 1 ML Nb on Pd(111) and the surface of a Pd monolayer on Nb(110). Next the study is extended to Rh which has one less *d* electron than Pd. I will show that Rh agglomerates on Ta(110) but grows layer by layer on Mo(110) which has less lattice mismatch with Rh(111). A novel orientation transition is observed for the first time during the growth of Rh on Mo(110) near 1 ML and the possible mechanisms are discussed in terms of second-layer effects, grain boundary interactions and finite-size effects. Finally the results are summarized and some general conclusions are drawn.

Chapter 2. Experimental Techniques

To study a well characterized surface at an atomic level, the composition of the surface must remain essentially constant over the duration of an experiment. The arrival rate of molecules per square meter from a gas of density n and with an average velocity v is

$$\Gamma = \frac{1}{4} nv = \frac{P}{\sqrt{2\pi mkT}} = 3.51\text{x}10^{22}\text{x}\frac{P}{\sqrt{mT}}, \tag{2.1}$$

where T is the temperature in K, P is the pressure in Torr, and m is the molecular weight in atomic unit. For CO at T=300 K and a Mo(110) surface, 1 ML=1.4x10^{15} atoms/cm^2,

$$\Gamma = 2.7\text{x}10^5 P \text{ (ML/s)}. \tag{2.2}$$

It is clear that the reduction of incidental contamination to less than ten percent of a monolayer during an experimental time of an hour requires background pressures of 10^{-10} Torr or better.

The widely used unit in adsorption studies is *Langmuir* (L) defined as 1 L≡10^{-6} Torr sec exposure. Using Eq. (2.2), 1 L corresponds to 0.27 ML exposure for CO at room temperature. Exposures of 20 L are used in the CO adsorption studies discussed in this thesis, they correspond to 5.4 ML exposures and are found to be enough to saturate the surfaces.

2.1 Sample Preparation

2.1.1 Single Crystal Substrates

The single-crystal samples used in this thesis are prepared in three different ways: (1) recrystallizing a polycrystalline foil by pulse heating; (2) epitaxial growth of a film on a single-crystal substrate; (3) cutting from a raw single crystal.

Ta(110) substrates were prepared by recrystallizing 0.001 in.-thick Ta foils by pulse heating to 2000 °C for several seconds. The foils were initially annealed at about 1000 °C in 10^{-6} Torr oxygen for 1 hour to remove carbon. The sample temperature was measured by an optical pyrometer. High temperature heating in UHV not only gets rid of the oxygen but also produces visible single-crystal grains in the (110) orientation as shown by LEED examinations. The advantage of using a single-crystal foil is the ease of mounting and in control the temperature. The problem is that warping as well as thermal faceting sometimes occur due to high temperature pulsing.

Pd(111) substrates were prepared by epitaxial growth of Pd(111) films on Ta(110). This is based on previous studies which show that Pd grows layer-by-layer on Ta(110) and a thick Pd film exhibits (111) orientation[10]. The advantages of epitaxial growth is that it is quick and has the capability of *in-situ* preparation of sandwich samples. The problem is limited smoothness and usable times.

The Mo(110) substrate was a 10-mm-diameter 2-mm-thick disk cut from a raw single crystal, then mechanically polished and chemically cleaned. It was spot welded to two Ta wires which were attached to two threaded Mo posts and fixed by Mo nuts. On the back of the crystal, a W filament, shielded by a can made of Ta foil which also had some focusing effect, was wrapped around the other two Mo posts and could be adjusted and fixed by Mo nuts. The four posts were supported by a Mo plate which was mounted on an XYZ manipulator with three axes of rotation. During electron-beam bombardment heating, the sample potential was raised to 2 kV and the power was varied by changing the filament current. An infrared pyrometer was used to monitor the sample temperature. The crystal was cleaned by heating at 1000 °C in 10^{-6} Torr oxygen to remove carbon, followed by flashing to 1700 °C in UHV to remove oxygen. These cleaning procedures were repeated until AES and UPS could not detect any C, O or other impurities and a sharp LEED pattern was obtained. One of the advantages of using a single-crystal sample is the ease of achieving a large, atomically flat and well-defined surface.

2.1.2 Thin Film Epitaxy

Thin films are usually prepared by thermal evaporation or sputtering. The deposition rate was measured by AES or a quartz-crystal thickness monitor. Sputtering deposition is suitable for the growth of compound or non-conducting films. DC sputtering has been used to make high T_c superconducting films. This was done by floating the target at -2kV with the grounded substrate ~1" away. A discharge between the target and the substrate can then be started by filling the chamber with Ar to 0.05 Torr. The Ar^+ will be accelerated to the target and sputter the atoms which will be deposited on the substrate. This thesis concerns mostly thin metal films which can be grown by thermal evaporation either through resistive or electron beam heating.

A. Resistive Heating Methods

Solid materials vaporize when heated to high enough temperature. The vapor flux onto a substrate is the most widely used method to grow thin films. The vapor pressure for a reasonable evaporation rate of 1 ML/min is on the order of 10^{-8} Torr. The chamber pressure during evaporation should be in low 10^{-10} Torr range in order to grow clean thin films and this requires thorough outgassing prior to evaporation. For low-melting point materials such as Cu, Ag, Au, Al and Pd, resistive heating a W basket containing the evaporant is usually used. The current ranges from 5-20 A depending on the basket size, the evaporated material and geometry. For highly reactive materials such as alkali metals, resistively heated commercial getter sources are used. For materials with higher melting points such as Rh, resistive heating a wire of the evaporant material is sometimes used, but the lifetime of this method is short because the wire simply breaks after several uses. This happened in trials of Rh evaporation. Resistively heating a W basket containing Rh wire lasts longer, but the outgassing is huge and takes a long time to complete so that evaporation in the low 10^{-10} Torr range is hard. I found that resistive heating of a 0.015" W wire with 0.01" Rh wire wrapped around it at a current of ~10 A is a good compromise. Long lifetime and low evaporation pressure ($\Delta P<2\times10^{-10}$ Torr) can be achieved in this way for Rh, and it is believed to work for similar materials as well.

B. Electron Beam Evaporator

For very high melting-point materials such as Nb, Ta or W, it is difficult to achieve a good evaporation rate using the resistive heating method. Electron-beam bombardment heating is suitable to evaporate this kind of materials. To fit an existing Vacuum Generator (VG) EG-2 electron-beam evaporator to our UHV chamber, a water-cooled hearth was made and welded to a 8" OD flange which also had a 2-3/4"-OD flange adapter port to provide the electrical connections. The filament and the totally electrostatic focusing assembly from the EG-2 e-beam evaporator were mounted on this hearth with the top surface of the screen 6 mm above the hearth for the best focus at a 1- mm diameter spot. The whole system is shown in Fig. 1. A Temscal CV-8 15kV1.5A power supply was used to run this gun for evaporation. A Universal Voltronics BRE-2.5-200 power supply was used to outgas the gun by biasing the filament at -1.1 kV relative to ground and grounding the filament shield, screen and hearth. The CV-8 was used only as a current source during outgassing by supplying a filament current of ~8 A to get an emission current of about 90 mA with the water-cooling interlock bypassed and the HV left off because it starts up at -5 kV. The outgassing lasted 10-30 minutes and was usually done before-, during- and right after baking, as well as when the chamber was first cooled down, to ensure a low evaporation pressure.

During the evaporation of Nb or Ta, the screen was biased at -9 kV relative to ground and the filament was floated to the screen through an isolation transformer. The evaporant temperature or evaporation rate are controlled by regulating the filament current to about 6 A for Nb or Ta with an emission current ~30 mA. The water-cooling was interlocked to the power supply and the trip point was set at 30 GPH (2.3 l/min).

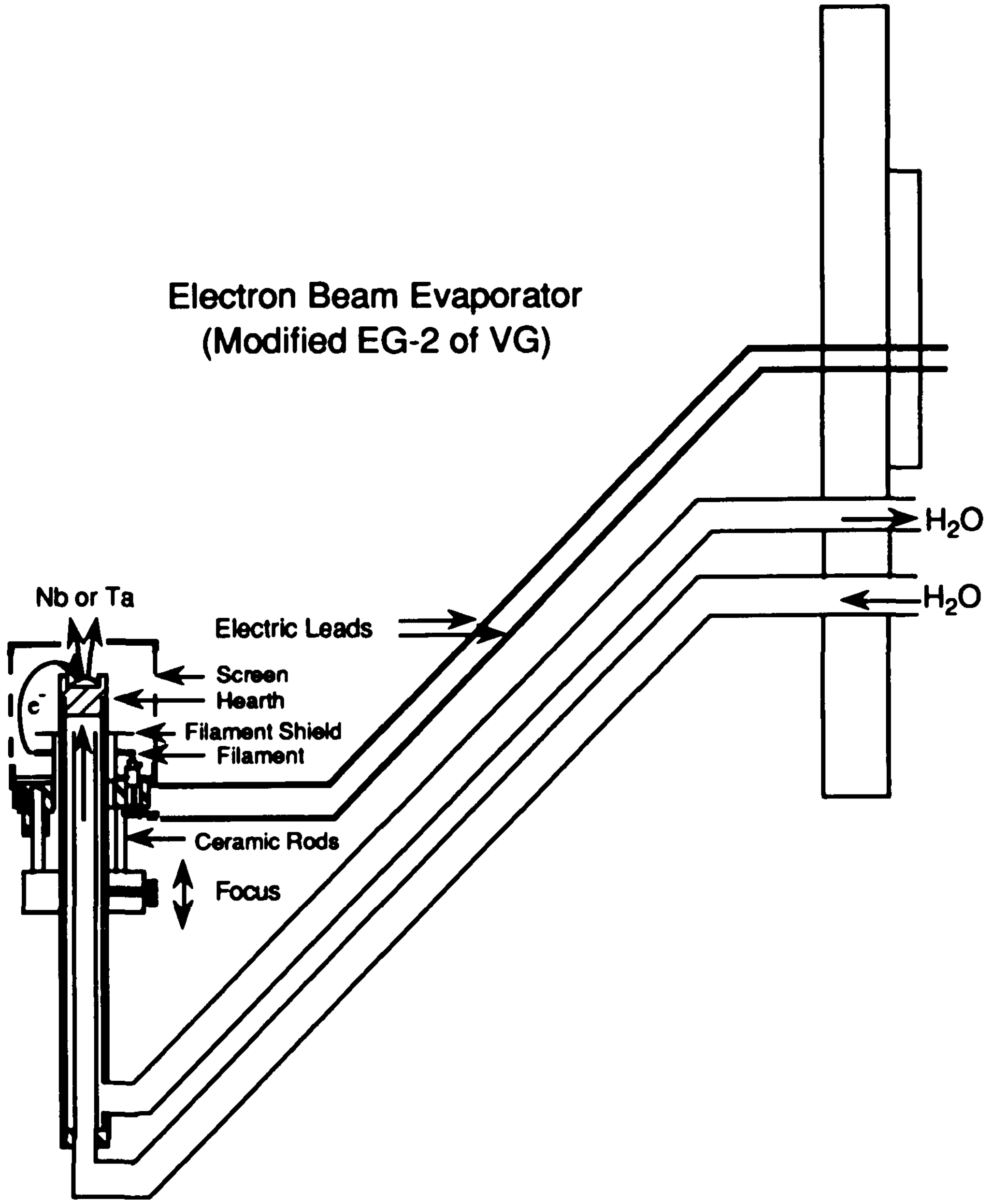

Figure 1. Schematics of the e-beam evaporator used for Nb or Ta deposition.

2.2 Sample Characterization

A wide variety of surface-sensitive techniques was used in this thesis in a combined way, trying to get a complete picture of the atomic geometry, electronic structure and chemical properties of bimetallic interfaces. In this section, the characterization methods are discussed in the order of electron, ion and neutral detection with emphasis on the physical principles behind these techniques and why they can yield the desired information. To avoid overlap, examples are given only for those aspects of the techniques which are not illustrated in the following chapters.

2.2.1 LEED, AES and PES

A feature common to LEED, AES and PES is the detection of electrons scattered or emitted from the surface. These techniques serve as surface science probes because electrons with 10-1000 eV kinetic energy ($E-E_F$) have a very short mean free path in solids. The surface sensitivity of electrons is illustrated in the so called "universal curve" of inelastic mean free path versus electron kinetic energy[11] (Fig. 2) which can be understood as follows. Single-particle excitations are responsible for the scattering at low energies and above the plasmon energy (typically 10-15 eV), the energy losses are dominated by plasmon creation which slowly becomes weaker as the energy increases. This mechanism of valence band electron excitation is the key to the universality because the electron density in the valence band is nearly a constant for most materials[12] - about 0.25 electrons/$Å^3$. It should be noted that the curve represents the surface sensitivity for normal takeoff angles. Therefore the surface sensitivity can be enhanced, not only by choosing an electron energy corresponding to the curve minimum, but also by detecting electrons at an angle θ by a factor of $\sec\theta$. The intrinsic surface sensitivity and its tunability by varying energy and angle offer great possibilities for applying these electronic techniques to study surface and interface phenomena. In the following, the basic principles of LEED, AES and PES are discussed separately to show how they can be used to determine the surface structure, composition and electronic structure respectively.

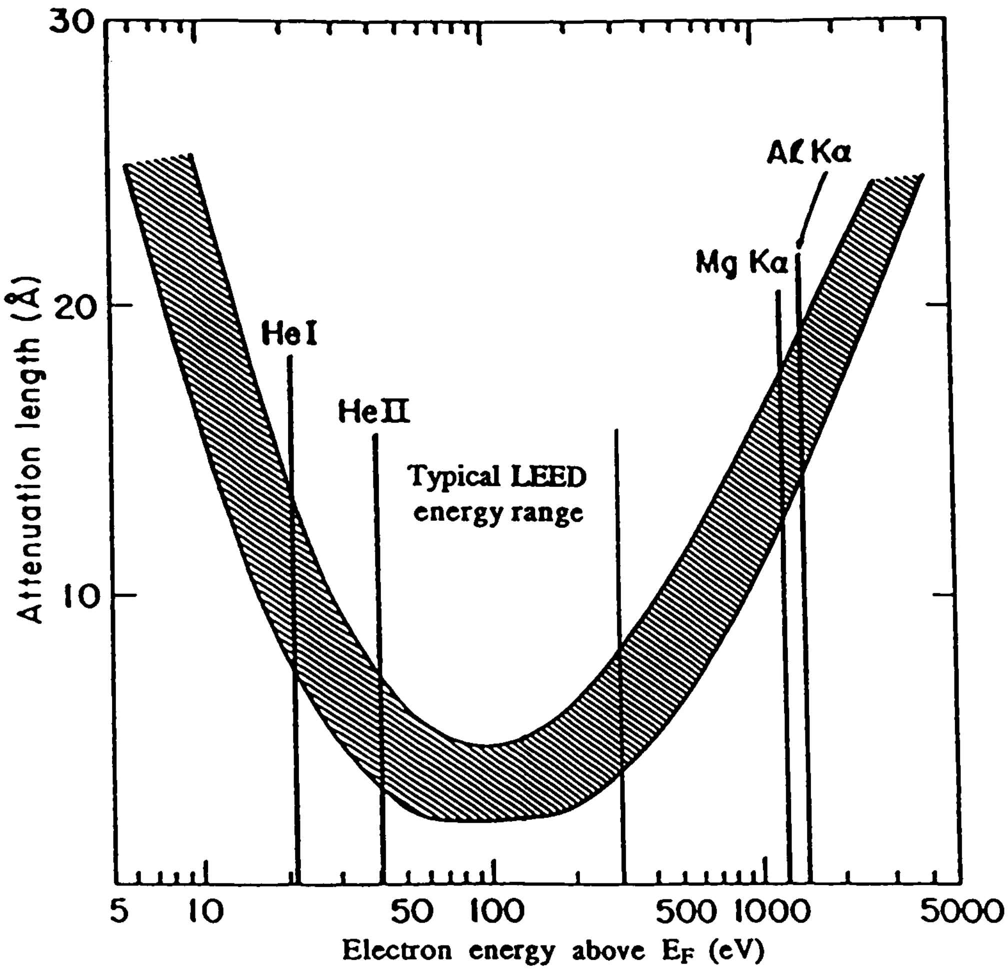

Figure 2. The universal curve of electron attenuation length versus kinetic energy in various heavy metals.

A. LEED

With E expressed in eV defined as the electron energy above the Fermi level, the electron wavelength in Å is given by

$$\lambda = \sqrt{\frac{150.4}{E}} \qquad (2.3)$$

For energies between 30 and 300 eV which are typically used in LEED, the wavelength is comparable to the lattice spacing of most crystals. The electron mean free path in this energy range falls into the broad minimum of the "universal curve" which corresponds to about two or three atomic layers. Both the penetration of the primary beam and the escape of the outgoing electrons are therefore limited to the surface region. This surface sensitivity and the suitable wavelength are the basic reasons why LEED is widely used as a probe of surface geometrical structure.

For a two-dimensional real-space lattice described by two lattice vectors **a** and **b**, the corresponding reciprocal lattice can be constructed from basic vectors $\mathbf{a}^*$ and $\mathbf{b}^*$ defined by

$$\mathbf{a}^* = \frac{\mathbf{b} x \mathbf{n}}{\mathbf{a}\cdot\mathbf{b} x \mathbf{n}} \qquad \mathbf{b}^* = \frac{\mathbf{n} x \mathbf{a}}{\mathbf{a}\cdot\mathbf{b} x \mathbf{n}} \qquad (2.4)$$

where **n** is a unit vector normal to the surface. Any vector relating two reciprocal lattice points must take the form:

$$\mathbf{g}_{hk} = h\mathbf{a}^* + k\mathbf{b}^*. \qquad (2.5)$$

Diffraction from two-dimensional lattice must satisfy the two Laue conditions:

$$\begin{aligned} \mathbf{a}\cdot\Delta\mathbf{k} &= h\lambda \\ \mathbf{b}\cdot\Delta\mathbf{k} &= k\lambda \end{aligned} \qquad (2.6)$$

and these can be solved whenever

$$\Delta \mathbf{k} = \mathbf{k} - \mathbf{k}_0 = \lambda \mathbf{g}_{hk} \tag{2.7}$$

where $\mathbf{k}$ and $\mathbf{k}_0$ are unit vectors along the incident and diffracted beam respectively. This means that there is a direct correspondence between the observed diffraction pattern and the reciprocal lattice of the surface.

Experimentally it is desirable to determine the real-space lattice based on the reciprocal lattice as indicated by LEED. Therefore the following relations are derived from Eq. (2.4),

$$|\mathbf{a}| = \frac{1}{|\mathbf{a}^*| \cdot \sin \alpha^*}$$

$$\alpha = \pi - \alpha^* \qquad \text{or} \qquad \sin \alpha = \sin \alpha^* \tag{2.8}$$

and this is illustrated in Fig. 3.

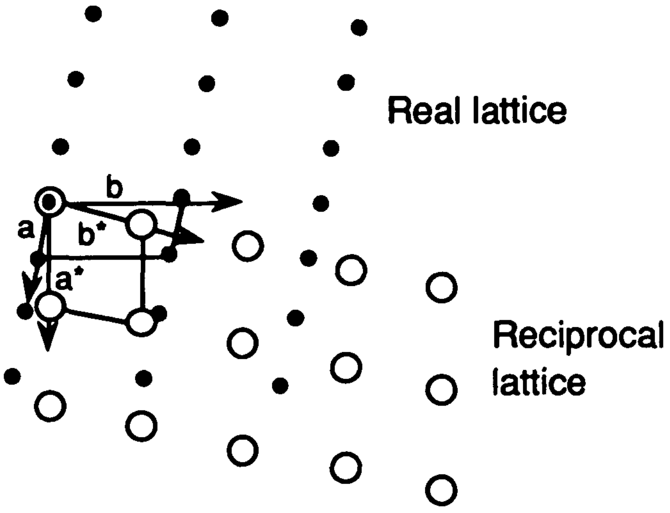

Figure 3. Relationship between real lattice and reciprocal lattice.

In studies of overlayer structures, sometimes more than one domain may exist on the surface. Each domain corresponds to a unique orientation and is symmetrically equivalent with regard to the substrate. If the domain sizes are small compared with the coherence length of the incident electron beam ξ, interference may occur between the diffracted waves from different regions. However, more often the domains are much larger than ξ, but smaller than the total beam area and the resulting diffraction pattern will be a superposition of the patterns that would be expected from each domain individually[13]. ξ can be estimated from the divergence and energy spread of the electron beam by[14]

$$\xi = \frac{2\pi}{\delta(\Delta k_{||})} \tag{2.9}$$

because the diffraction condition is

$$\Delta k_{||} = k \left| \sin\theta_o - \sin\theta_i \right| = \frac{2\pi}{a} \tag{2.10}$$

where a is the surface periodicity. Taking the partial derivatives gives

$$\xi_\theta = \frac{\lambda}{\cos\theta_o \delta\theta} \qquad \xi_E = \frac{2aE}{\delta E} \tag{2.11}$$

Using typical values of λ=1 Å, $\cos\theta_o$=1 and $\Delta\theta=10^{-2}$ rad gives ξ_θ=100 Å, while for ΔE=0.5 eV, E=100 eV and a=2.5 Å gives ξ_E=1000 Å. It is therefore evident that the angular and not the energy broadening determines the coherence length.

A Varian four-grid LEED optics system was used in this thesis for the determination of surface structure. The electron gun is operated at a beam voltages of 40-240 V with corresponding beam currents of 0.5-3 μA. The screen voltage varies from 3-8 kV and was usually set at 6 kV for high spot intensity and low background.

B. AES

When the electrons at core level E_A are knocked out either by incident electrons or photons, electrons at a shallower level E_B may fill the core hole to lower the system energy. This transition may be either radiative so that photons with an energy of $h\nu = E_A - E_B$ are emitted, or nonradiative so that the released energy is transferred to the electrons at an energy level E_C, which gives rise to the emission of Auger electrons with a kinetic energy of

$$E_{KE} = E_A - E_B - E_C - U \qquad (2.12)$$

where U is the hole-hole interaction energy. These two processes are schematically shown in Fig. 4.

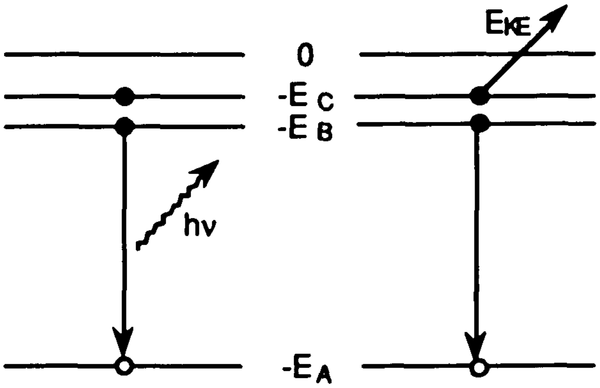

Figure 4. Radiative and Auger transitions after the creation of a core hole.

Photon emission is of little interest in surface science because of the long mean free path of photon in solids. Since the excitation beam is also generally deeply penetrating, it gives rise to a bulk analytic tool. By contrast, Auger emission can be considered as an internal photoemission and the low kinetic energy Auger electrons have short mean free path, making AES a surface sensitive probe. Since collections of fingerprint spectra for essentially all elements and some compounds exist for the purposes of species identification, AES is a powerful tool for surface composition analysis. Thin film coverage and growth morphology can be determined by detailed analysis of AES peak intensity variation with deposition time.

Because of the intense and steeply sloping background in the energy distribution of secondary electrons, it can be extremely difficult to observe Auger peak in a normal pulse counting mode. By superimposing a modulation on the energy scan and taking the output through a lock-in amplifier, the Auger spectrum can be obtained in the more usual differential form. This mode suppresses the large secondary background and turns a single peak into a positive and a negative excursion. The Auger intensity is usually defined by the peak-to-peak height. Figure 5 shows some typical Auger spectra obtained with a single pass cylindrical mirror analyzer (CMA). The primary electron energy is 2 keV and the beam current is 150 μA while the electron multiplier voltage is at 1.2 kV and the peak-to-peak modulation is 2 V. The positive excursion part of the peak is much weaker than the negative part in the Al spectrum due to the broad loss tail of the undifferentiated Auger peak. For this reason, it is common to label peak energies in AES as the energy of the largest negative excursion in the differentiated spectrum. In the spectrum of 6 ML Al/Ni, a chemically shifted Al peak is clearly seen in addition to the peak corresponding to Al metal. The AES peak positions thus can indicate different chemical environments and provide a way to identify surface species. The electron mean free path for the energy range in Fig. 5 is near the minimum of the "universal curve" which is about 2 or 3 layers. The still quite strong Ni peak in the 6 ML Al/Ni spectrum thus indicates significant interdiffusion at the Al/Ni interface.

The AES data presented in the rest of this thesis were obtained with a PHI double pass CMA operated at a channeltron voltage (CV) of 1.35 kV. The internal coaxial electron gun supplied 2 keV energy electrons with an emission current of 1 mA and a sample to ground current of ~3 μA. The lock-in output was first digitized by a V-F converter and then counted by a scaler in a CAMAC system and finally stored in an IBM PC.

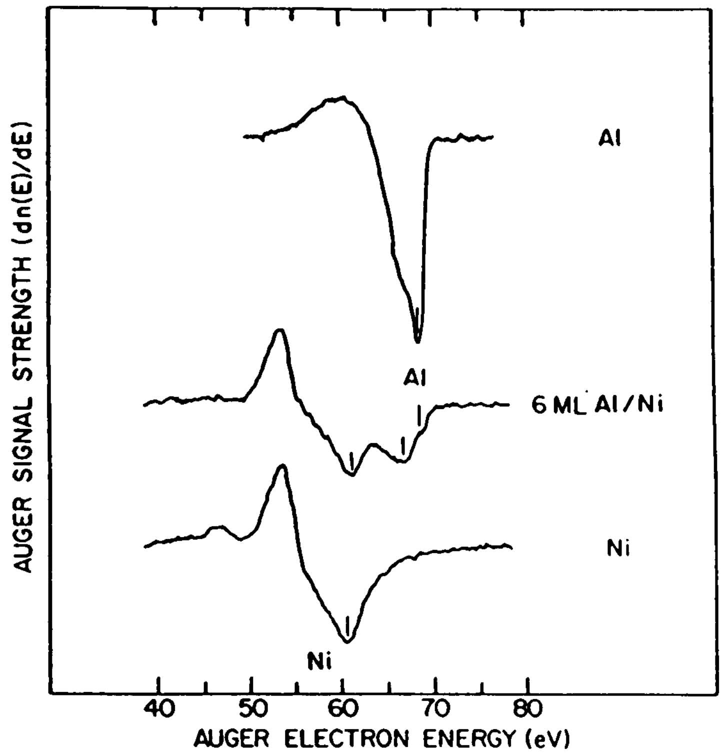

Figure 5. Derivative Auger spectra of Al, Ni and 6 ML Al/Ni.

C. PES

The kinetic energy of the photoelectron is described by the conservation of energy

$$E_k = h\nu - E_B - \phi \qquad (2.13)$$

where $h\nu$, E_B and ϕ are the incident photon energy, the binding energy of the initial state relative to the Fermi level (E_F) and the sample work function respectively. The initial states are referenced to E_F because the sample and electron analyzer may have different local vacuum levels due to work function differences but their Fermi levels line up when the sample is grounded.

The 'three-step model' of photoemission is widely used in interpreting experimental data and involves three independent processes[15]: photoabsorption, transport of the excited electron to the surface, and the escape of the photoelectron into vacuum. The photoemission intensity from primary electrons with an energy E above Fermi level can then be factorized into a distribution function of photoexcited electrons P(E), a transmission function T(E) and a escape function D(E)

$$I(E) = P(E)T(E)D(E). \qquad (2.14)$$

Assuming that the inelastic scattering is characterized by a finite electron mean free path $\lambda(E)$, T(E) is given by

$$T(E) = \frac{\int_0^\infty e^{-x/\lambda(E)} e^{-x/\lambda_{ph}(\nu)} dx}{\int_0^\infty e^{-x/\lambda_{ph}(\nu)} dx} = \frac{\lambda(E)}{\lambda(E) + \lambda_{ph}(\nu)} \qquad (2.15)$$

where $\lambda_{ph}(\nu)$ is the photon attenuation length which is about 10^3 - 10^4 Å for X-rays. Escape is possible only for those electrons with normal kinetic energy component higher than the work function ϕ and this defines an escape cone with an opening angle of θ_c

relative to the surface normal, $\cos\theta_c=(\phi/E)^{1/2}$. For an isotropic distribution of electrons inside the solid, D(E) is then given by

$$D(E) = \begin{cases} \dfrac{\int_0^{\theta_c} 2\pi\sin\theta d\theta}{4\pi} = \dfrac{1}{2}\left[1 - \sqrt{\dfrac{\phi}{E}} \right], & E > \phi \\ 0, & E \leq \phi. \end{cases} \qquad (2.16)$$

P(E) is given by the golden-rule expression of the transition probability between an initial state with a binding energy E_B and a final state with an energy E above Fermi level[16]

$$P(E) = \frac{1}{h}\left(\frac{2\pi e}{mc}\right)^2 \left| \langle f \mid A\cdot\mathbf{p} \mid i \rangle \right|^2 \delta(E - E_B - h\nu) \qquad (2.17)$$

Both D(E) and T(E) are smooth functions of E beyond the low-energy cutoff and although they may distort the energy distribution of photoexcited electrons, they are not expected in themselves to give rise to structures in I(E). In general P(E) depends strongly on the density of each of the two states involved as well as the coupling between them. Now if the coupling varies slowly with energy and if the final state density (usually a continuum of free electron states) is fairly flat, then the photoelectron energy spectrum should simply show the energy distribution of occupied electronic states of the surface shifted up in energy by an amount of hv. Since the atomic photoionization cross sections are well tabulated for most electronic levels of essentially all elements at various photon energies commonly used in photoemission,[17] an examination of photoemission intensity variation with photon energy allows the identification of the character of states in photoemission spectra. Synchrotron radiation is very powerful in this aspect because of its continues energy tunability. For example, the energy dependence of photoemission spectra of $YBa_2Cu_3O_{9-\delta}$ has shown the mostly O character of the states near E_F and this suggests that the charge carrier in high T_c superconductors is the O hole.[18]

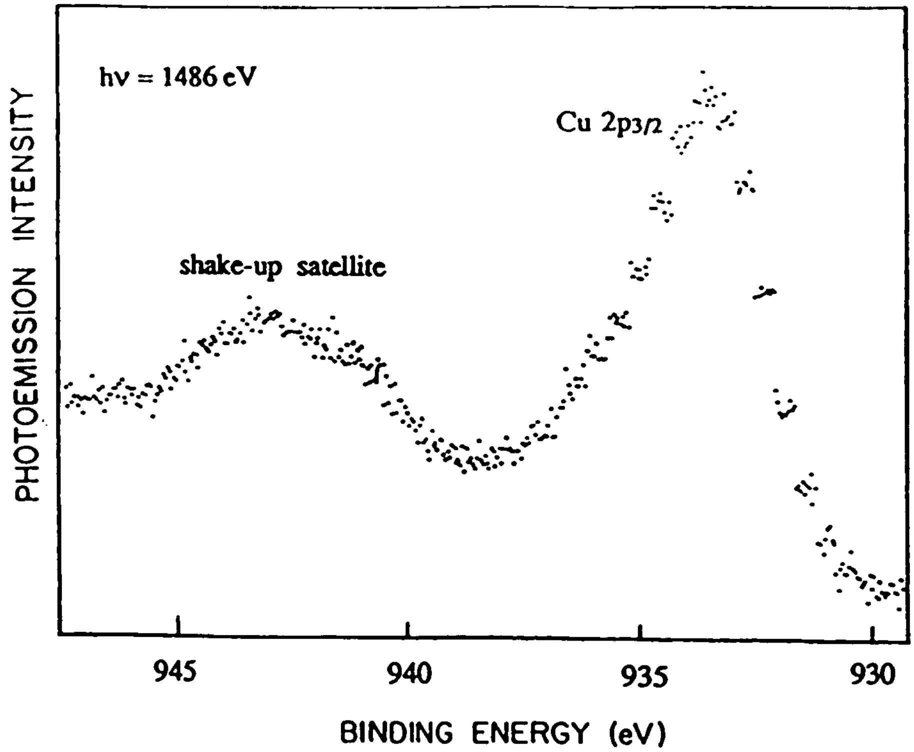

Figure 6. Cu $2p_{3/2}$ core level spectrum for $La_{0.9}Sr_{0.1}CuO_4$ showing the existence of shake-up satellite.

The above single-electron interpretation of photoemission is complicated by the so called 'many-body' effects. When a core hole is created by photoionisation, other electrons relax to lower energy states to screen the hole partially and thereby make more energy available to the outgoing photoelectrons. On the other hand, photoemission process is rapid (10^{-16} sec) and the valid 'sudden' approximation in which the perturbation is switched on momentarily may yield final states in which an electron is in an excited bound state, or another electron is ejected into the continuum of unbound states above vacuum level. Such processes leave less energy for the emitted photoelectrons and give rise to lower kinetic energy satellites which are usually referred to as shake-up and shake-off for an excitation to a bound state and to the continuum respectively. These intrinsically 'many-body' effects add additional power to PES in some cases. As an example, Fig. 6 shows the Cu $2p_{3/2}$ core level spectrum obtained with Al Kα radiation for a $La_{0.9}Sr_{0.1}CuO_4$ superconductor. The shake-up satellite seen in this spectrum is also observed for CuO but is not seen for either pure Cu metal or Cu_2O. This satellite is due to the excitation to the unoccupied 3*d* states which are not available for Cu metal or Cu_2O because of their filled *d* band. Thus the spectrum in Fig. 6 identified the 2^+ valence of Cu in $La_{0.9}Sr_{0.1}CuO_4$, which is important to the understanding of its superconductivity.

It should be noted that shake-up or shake-off satellites are localized and this can be used to distinguish satellites from collective losses such as plasmon creation. The satellite in Fig. 6 is not due to plasmon losses because it is not seen in the O 1*s* core level spectrum of the same sample. Plasmon loss features are often seen in materials such as Al, Mg and Na in which plasmons are weakly damped. Figure 7 shows a plasmon feature associated with Na 2*p* core level obtained with 75 eV synchrotron radiation and a VG angle-resolved analyzer at normal emission position. The plasmon feature disappeared after dosing ~200-L of NH_3 at 80 K. A close examination of the disappearance of plasmon losses and the Fermi level has been used to study the metal-nometal transition of the solid NH_3-Na system.[19]

The experimental setup of PES used in this thesis is quite conventional. A high intensity differentially pumped gas discharge lamp supplied photons at fixed energies of HeI (21.2 eV), HeII (40.8 eV), and NeI (16.8 eV). The HeI line is always stronger than HeII, but reasonably strong HeII emission can be achieved by reducing the helium gas pressure to a value obtained just before the discharge shutoff which is characterized by a bluish florescence. The lamp is usually operated at 1 kV and 50-70 mA. The photoelectrons are analyzed by a PHI double pass CMA which was operated at a CV of 2.5-2.7 kV and a pass energy (PE) of 10-15 eV for hν = 21.2 or 16.8 eV, and a CV of 2.9-3 kV and PE of 25-50 eV for hν = 40.8 and 1486.7 eV (supplied by a PHI X-ray source with Al anode). Part of the photoemission work was conducted at the synchrotron light source in which case either an angle-resolving VG or a VSW hemispherical analyzer was used.

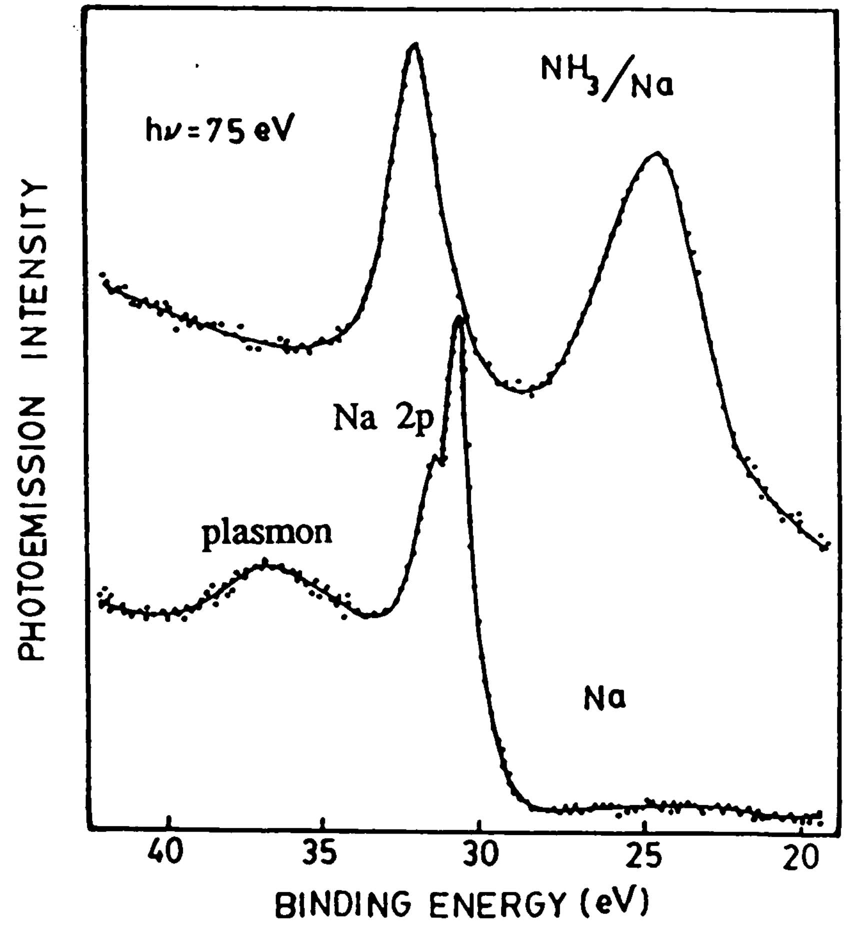

Figure 7. Na $2p$ core level spectra for Na and NH_3/Na.

2.2.2 Low Energy Ion Scattering Spectroscopy (LEIS)

It can be seen from the "universal curve" that the best surface sensitivity using electron detecting techniques is about 2 or 3 atomic layers. For many surface problems, an unambiguous analysis of the topmost layer only is needed which is impossible by electron spectroscopies because of their averaging over several atomic layers. A surface specificity of only one atomic layer is particularly useful in growth studies, surface alloy formation and segregation, etc and it can be achieved by low energy inert gas ion scattering spectroscopy.

Figure 8 shows a schematic of the scattering of an ion from a surface atom. Due to the small deBroglie wavelength of ion, quantum-mechanical effects can be neglected and the interaction can be treated classically. Using energy and momentum conservation, the following equation can be easily derived for $M_2 > M_1$,

$$\frac{E_1}{E_0} = \left[\frac{\cos\theta + \sqrt{\left(\frac{M_2}{M_1}\right)^2 - \sin^2\theta}}{1 + \frac{M_2}{M_1}}\right]^2 . \qquad (2.18)$$

Since the energy of the scattered ion for a fixed scattering angle depends only on the mass ratio $A = M_2/M_1$, an energy spectrum gives a direct picture of the surface composition.

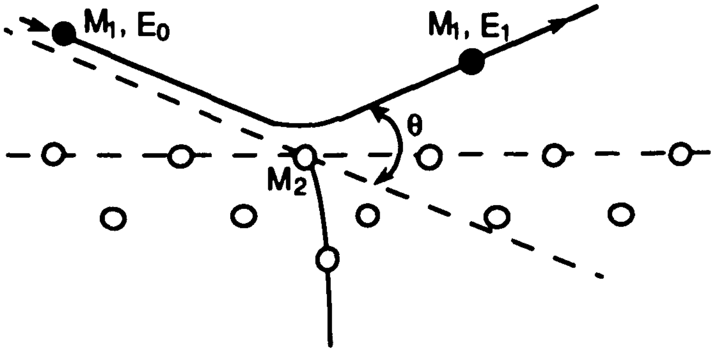

Figure 8. Schematics of the ion-surface atom collision.

The ability to resolve different mass numbers on the surface is related to the energy width of the scattered peaks which depend on the energy and angular resolution of the experimental arrangement. Partial differentiation of E_1 with respect to M_2 in Eq. (2.18) gives the mass resolving power

$$\left(\frac{M_2}{\Delta M_2}\right) = \left(\frac{E_1}{\Delta E_1}\right)\frac{2A}{A+1}\left[\frac{A + \sin^2\theta - \cos\theta\left(A^2 - \sin^2\theta\right)^{\frac{1}{2}}}{A^2 - \sin^2\theta + \cos\theta\left(A^2 - \sin^2\theta\right)^{\frac{1}{2}}}\right]. \qquad (2.19)$$

Eq. (2.19) shows that better mass resolution can be achieved at larger scattering angle and smaller A. It should be noted that ΔE_1 in Eq. (2.19) is the total energy width which results from the combination of the primary beam energy spread and angular divergence, analyzer internal energy resolution and collecting angle.

Multiple scattering effects may also be seen in LEIS spectrum, especially for alkali ion scattering or when neutral atoms are also analyzed in noble gas ion scattering. When scattering into an angle θ is composed of two single scattering events each through angle $\theta/2$, the energy of the double scattered ion can be easily derived by successively applying equation (2.19) as

$$\frac{E_2}{E_0} = \left[\frac{\cos\frac{\theta}{2} + \left(A^2 - \sin^2\frac{\theta}{2}\right)^{\frac{1}{2}}}{1 + A}\right]^4. \qquad (2.20)$$

Although the energetics of the scattering process are independent of the ion-atom interaction potential V(r), the scattering cross-sections do depend on V(r). In the LEIS energy range (~0.2-10 keV), V(r) is usually taken to be a purely repulsive Coulomb potential between nuclei with electron screening described by the Moliere approximation to the Thomas-Fermi screening function between atoms of atomic numbers Z_1 and Z_2

$$V(r) = \frac{Z_1 Z_2 e^2}{r}\varphi\left(\frac{r}{a}\right)$$

$$\varphi(x) = 0.35e^{-0.3x} + 0.55e^{-1.2x} + 0.1e^{-6x}. \qquad (2.21)$$

The commonly used screening length a, was proposed by Firsov and is given by[20]

$$a = \frac{0.4685}{(\sqrt{Z_1} + \sqrt{Z_2})^{2/3}}\ \text{Å} \quad . \tag{2.22}$$

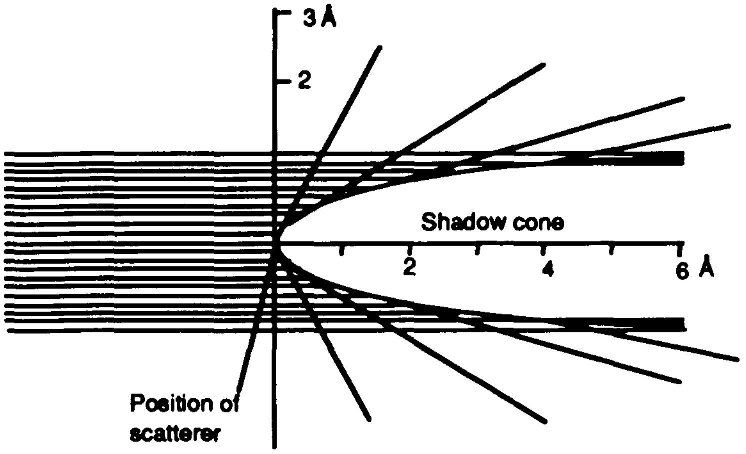

Figure 9. Scattering trajectories for 1 keV He$^+$ ion scattering from an O atom showing the existence of shadow cone.

Using the above potential, the relationship of scattering angle and impact parameter b can be calculated. The repulsive interaction between the incident ion and the target atom leads to a region behind the target into which no ion can penetrate, i.e., the atom casts a shadow. This is illustrated in Fig. 9 where a set of ion trajectories, calculated by Woodruff and Delchar[14] for 1 keV He$^+$ ions scattered by an O atom, are plotted. At a typical interatomic spacing in a solid of ~2 Å behind the scatterer, the width of the shadow cone is slightly larger than 1.5 Å. This means that in an ion scattering study under these conditions the top layer atoms will typically shadow much of the second layer and all the deeper layers. A universal expression for r/r_c as a function of r_c/a has been obtained by Oen.[21] Here r and a are the shadow cone radius and screening length. The shadow cone radius r_c for an unscreened Coulomb potential is given by

$$r_c = 2\sqrt{\frac{Z_1 Z_2 e^2 l}{E_o}} \tag{2.23}$$

where l is the distance behind the target atom.

The extreme surface sensitivity of noble gas LEIS is the result of the strong neutralization of scattered ions in addition to the broad shadow cone radius. The ionization energy for noble gas is much larger than the work function of most solids. Thus, tunneling of electrons from the substrate to the ion is very probable, leading to a high ion neutralization probability and only a small fraction $<10^{-2}$ of all particles survive the scattering as ions.[22] The large cross section (~1 Å^2) and shadow cone radius (~1 Å) guarantee that most ions never get past the top atomic layer. Those do are not only blocked (blocking effects) by the shadowing of top layer atoms during the exit process but are also quickly neutralized by electron capture and will not contribute to the experimental signal if only charged particles are collected at the detector. The strong neutralization of noble gas ions also suppresses multiple scattering and thus simplifies the use of LEIS for compositional analysis.

While the energy spectra of scattered ions gives the composition of the top atomic layer, the angular scans can lead to structural determination via shadow effects. The basic idea is illustrated in Fig. 10 which shows a side view of the surface. Large angle (θ near 180°) scattering can be observed only when an atom is hit with an impact parameter near zero. Significant scattering can be seen at large angle of incidence (ψ) of the ion beam relative to the surface. However, if ψ is lowered to below a certain critical angle ψ_c, defined as the angle where each atom just disappears in the shadow of its neighbor, all the surface atoms will be hidden in the shadow of their neighbors, the backscattered ion signal will rapidly diminish, and all ions are scattered through smaller angles. The experimentally determined ψ_c can then be related to the shadow cone radius r at a distance l from the target atom and the interatomic distance d by simple geometry:

$$r = d \sin\psi_c$$
$$l = d \cos\psi_c \qquad (2.24)$$

These relations can be used to obtain surface structure for a known shadow cone radius, or for a surface with known structure, to obtain the shadow cone radius and information on the potential acting between the ion and the surface atom. Since the neutralization probability of noble gas ions is high and can be handled only qualitatively at present, enhanced sensitivity and reduced primary ion beam current ~nA (therefore low surface damage) can be achieved by the detection of neutrals using a time-of-flight technique, or the use of alkali ions which have much less neutralization because their low ionization potentials are close to the work function of most metals.

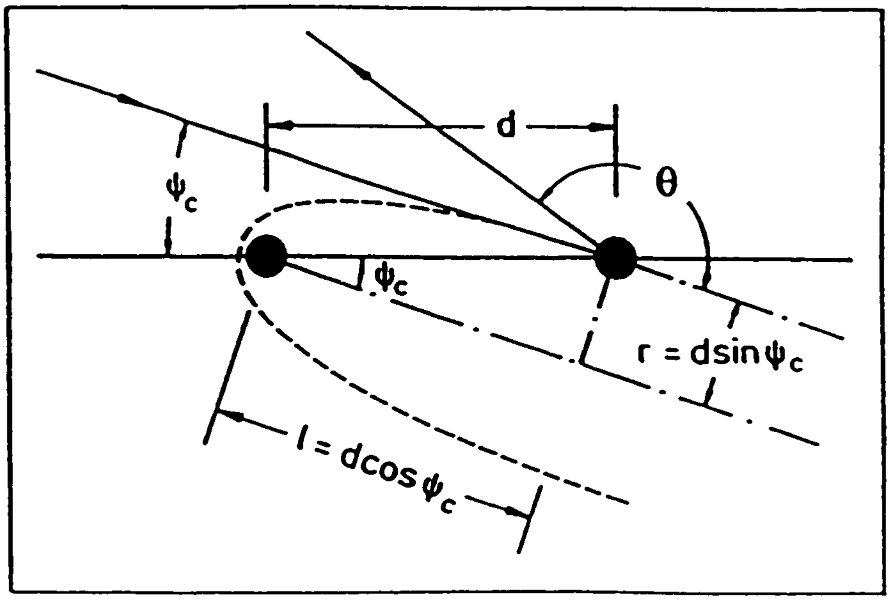

Figure 10. Principle of surface geometry determination by large-angle ion scattering.

The power of LEIS is its top-layer specificity. LEIS is used in this thesis to characterize the composition of the top surface layer whenever there is a doubt about the complete covering of the substrate by 1 ML of the overlayer. Since it is done usually in combination with AES, UPS and LEED, it is convenient to modify the double pass CMA used for AES and UPS so that it can be used to analyze ions for LEIS. This is shown schematically in Fig. 11. The battery box shown by the dashed square is added to define the pass energy and to attract ions into the channeltron, both with reversed polarity. A removable stainless steel shield in front of the CMA, with an opening angle of ~30° and its center line in the plane spaned by the incident ion beam and the CMA axis, defines a scattering angle of ~150°. The PHI double pass CMA controller in XPS mode with the same data acquisition program for XPS can then be used for LEIS with scan from high to low ion energies because the CMA retarding grid acts as an accelerating grid for ions.

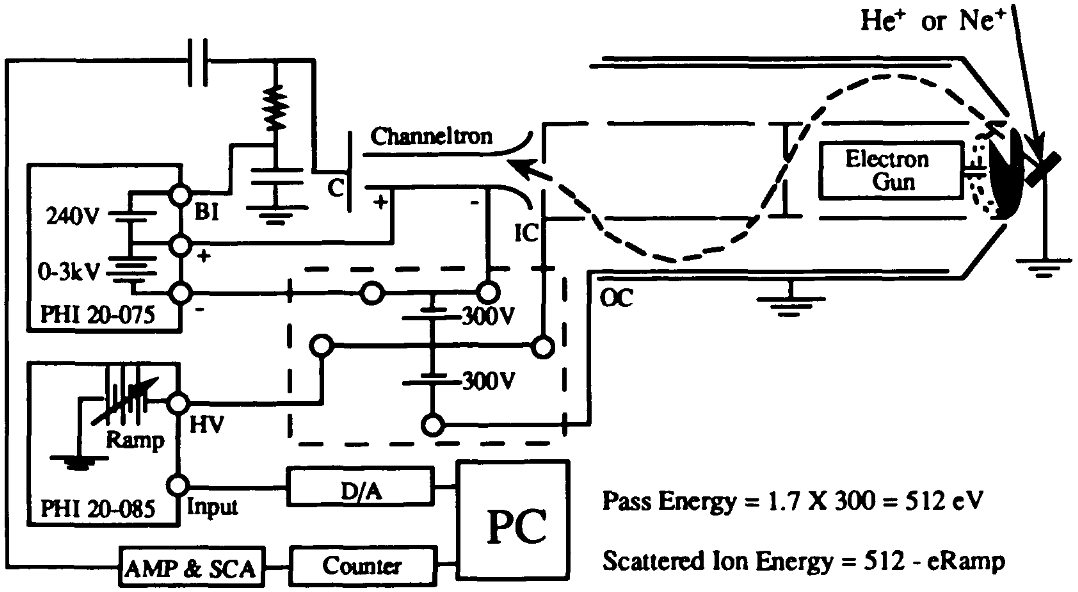

Pass Energy = 1.7 X 300 = 512 eV

Scattered Ion Energy = 512 - eRamp

Figure 11. Schematics of LEIS setup using a CMA.

The primary ion beam was supplied by a differentially pumped PHI ion gun. Since the shadow cone radius increases with Z_1 and decreases with E_o, lower energy and heavier incident ions yield far more surface specific scattering data than higher energy and lighter ions. Heavier incident ions can also yield higher mass resolution but it can damage the surface more seriously. He^+ or Ne^+ ions were used as a compromise to resolve the metal features under study while minimizing surface damage during a reasonable experimental time of about 1 minute. It is also important to know what kind of operating pressure is needed. The mean free path of ion can be written as

$$l = \frac{1}{\sqrt{2}n\pi d^2} = \frac{kT}{\sqrt{2}\pi P d^2} . \qquad (2.25)$$

Using d of 2.2 and 3.2 Å for He and Ne respectively, and T=300 K in Eq. (2.25), we have

$$l = \frac{1.3\text{x}10^{-4}}{P(\tau)} \text{ m for He and } l = \frac{0.6\text{x}10^{-4}}{P(\tau)} \text{ m for Ne.}$$

Therefore the He or Ne pressure should be lower than $1\text{x}10^{-4}$ τ in order to have a mean free path larger than ~1 m, which is required for the ions to reach the sample and to be detected without extra scattering events. The ion gun was operated at 500 eV energy and 20 mA emission current with a pressure of ~$2\text{X}10^{-6}$ τ in the main chamber and ~$4\text{X}10^{-5}$ τ in the ionization chamber. Surface damage (sputtering) was checked by taking consecutive spectra of the metal monolayer under these conditions. Negligible damage was seen for ion scattering with He^+, but damage was observable, as indicated by the changes in the ratio of substrate and overlayer signals, in the third scan of the energy spectra with Ne^+. The main contribution to the energy width of the scattering peaks in this setup comes from the primary ion beam energy spread. A Wien filter as an energy filter will be necessary to improve the mass resolution.

2.2.3 TPD and high pressure reactions

A. TPD (Temperature Programmed Desorption)

The stability of an overlayer and how strongly an adsorbed molecule is bonded to a surface are important questions in surface science. Although it can be approached by carefully examining what is on the surface using PES, AES, LEIS, LEED and their variation with temperature, this question is often resolved in a more direct and quantitative way by monitoring what comes off the surface and at what temperature by TPD.

For an atomic or molecular adsorbate, the desorption rate will depend linearly on the surface coverage θ and the desorption is called first order. For a dissociatively adsorbed diatomic molecule, the desorption may involve the recombination of the dissociated atoms and thus second order desorption becomes possible with a desorption rate proportional to the square of θ. Following Redhead[23], the desorption rate may be generally described by an Arrhenius equation

$$-\frac{d\theta}{dt} = \theta^n \nu_n \exp(-E_d/RT) \qquad (2.26)$$

where the rate constant ν_n can be thought as the attempt frequency, E_d and n are the desorption energy and the order of desorption respectively. Mass conservation requires

$$c\frac{S}{V}\frac{d\theta}{dt} = \frac{p-p_0}{\tau} + \frac{dp}{dt} \qquad (2.27)$$

where c is a constant, S and V are the sample area and the chamber volume respectively, p and p_0 are the pressure during desorption and the steady-state pressure respectively, and τ is the gaseous species mean residence time which is inversely proportional to the system pumping speed.

TPD is usually conducted in a flow condition at high pumping speed, τ→0 and thus,

$$\frac{d\theta}{dt} = \frac{V}{c\tau S}(p-p_o) \propto \Delta p \quad . \qquad (2.28)$$

A TPD spectrum is a plot of the partial pressure rise, Δp, as measured by a mass spectrometer versus temperature T which is usually varied linearly with time t. For a ramp rate β=dT/dt, the peak desorption temperature T_m can be determined from d(Δp)/dT=0 or $d^2\theta/dt^2=0$ [Eq. (2.28)] which gives

$$\frac{E_d}{RT_m^2} = \frac{n\theta_m^{n-1}\nu_n}{\beta}\exp(-E_d/RT_m) \quad . \qquad (2.29)$$

For first order desorption, n=1,

$$\frac{E_d}{RT_m^2} = \frac{\nu_1}{\beta}\exp(-E_d/RT_m) \quad ; \qquad (2.30)$$

for second order desorption n=2,

$$\frac{E_d}{RT_m^2} = \frac{2\theta_m\nu_2}{\beta}\exp(-E_d/RT_m) \quad . \qquad (2.31)$$

Generally a second order desorption curve is fairly symmetric about T_m so that the coverage θ_m at T_m is just half of the initial coverage θ_o.[14] Thus

$$\frac{E_d}{RT_m^2} = \frac{\theta_o\nu_2}{\beta}\exp(-E_d/RT_m) \qquad (2.32)$$

for second order desorption. These equations allow one to determine E_d, ν_n and the desorption order from measurements of the dependence of T_m on β and θ_o. Recent progress includes the derivation of rate equations using the lattice-gas model, which is particularly successful in describing zero-order desorption[24].

Figure 12 shows the CO TPD spectrum for initial saturation coverage of CO on Ta covered by a Pd overlayer. The 10 K/s linear temperature ramp was provided by a LAMBDA LT-801 programmable power supply controlled by the RHK TM310 TEMPERATURE PROGRAMER. The CO partial pressure was measured by a UTI-100C quadruple mass analyzer operated at a filament current of 2 mA and an amplifier sensitivity of 10^{-8} AMP. The analyzer head (ionizer) was caped by a stainless steel can so that only a 4 mm diameter hole faced the sample center to reduce background due to the sample edge and support. Based on the peak desorption temperature of 390 K and assuming first order kinetics with $v_1=10^{13}$ s^{-1}, a desorption energy of 24 kcal/mole was obtained by solving Eq. (2.30), which is significantly less than the value of 34 kcal/mole for Pd(111) single crystal.

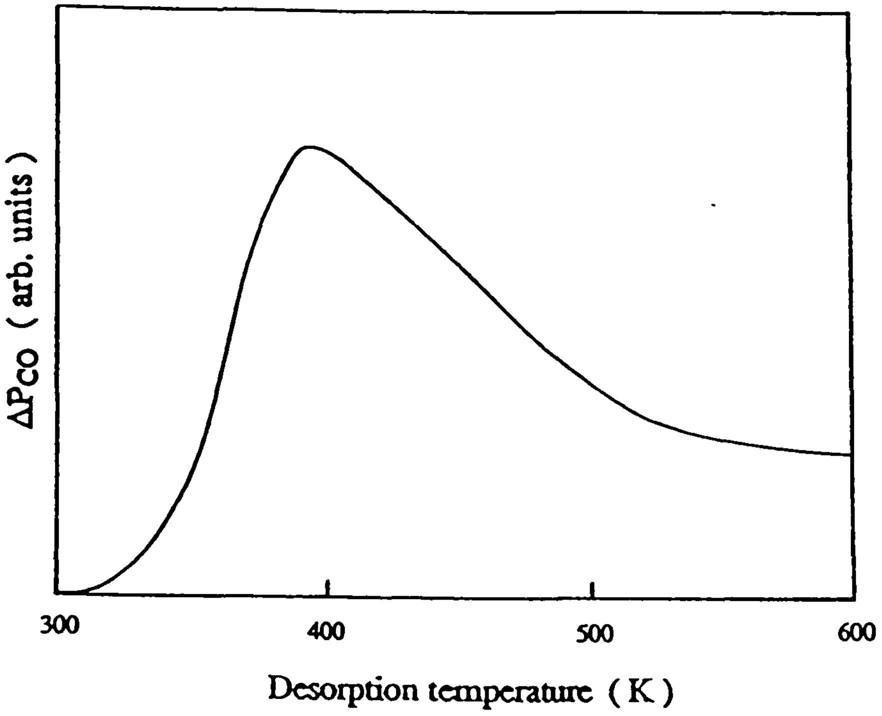

Figure 12. CO TPD spectrum for initial saturation coverage of CO on Ta covered by a Pd overlayer.

B. High Pressure Reaction

The surface science techniques discussed in previous sections were mostly used to study materials in UHV systems. Clearly to transfer what we learned using these techniques in the lab to industrial applications, work at higher pressures is necessary to provide the link between UHV and air. This is attempted in this thesis by studying catalytic reactions over Pd films on Ta at pressures in the Torr range.

The experiments were performed in a UHV surface analysis chamber combined with a high pressure reaction cell. The Ta foil was cleaned in the UHV chamber and coated on both sides with Pd films of the same thickness, as checked by AES. The sample was then lifted into the reaction cell, heated to 300 °C and maintained at this temperature throughout the reaction to enhance the reaction rate while suppressing the enormous hydrogen uptake which may ruin the sample by forming a hydride. The sample holder and support were kept at liquid nitrogen temperature to reduce their effects on the reaction. Propylene (C_3H_6) and deuterium (D_2) were premixed at 1:100 ratio to 1.5 atmospheres in the gas manifold and the mixture was then introduced into the reaction cell to a pressure of 0.1 Torr, as measured by a capacitance manometer (MKS-390 Pressure Transducer with a 270B Signal Conditioner/Readout). A small fraction of the gas in the reaction cell was leaked into the UHV chamber (Ion pump valved off and turbo pump on) to a pressure of $2.4X10^{-8}$ Torr. The reaction products were analyzed by a computer interfaced UTI-100C mass spectrometer which was set at the lowest possible ionization voltage and filament current to minimize cracking and ionization induced reactions. This was further assured by looking at C_3HD_7 and C_3D_8 formation. To make sure that C_3HD_7 and are C_3D_8 are not produced in the mass spectrometer ionizer, same mixture of C_3H_6 and D_2 was introduced from gas manifold directly into the UHV chamber (keep the sample in the reaction cell) to the same pressure of $2.4X10^{-8}$ Torr, and indeed no C_3HD_7 and C_3D_8 were formed in this way.

Some preliminary results are shown in Fig. 13 where the relative reaction rate, measured by the total peak area of C_3HD_7 and C_3D_8 normalized to that for clean Ta, is plotted as a function of Pd coverage. The reaction rate is low on pure Ta because Ta is too reactive and the hydrogen or carbon species are strongly chemisorbed on the surface, blocking the sites available for dissociation. On the other hand, the reaction rate for a Pd monolayer on Ta is low because the surface is too inactive. The strong hybridization between the orbitals of the Pd monolayer and Ta substrate results in a noble-metal like surface electronic structure which is quite different from either Ta or bulk Pd. In fact the surface is inert to CO adsorption at room temperature.[25] This demonstrates the importance of electronic effects on surface reactivity in a catalytic reaction at relatively high pressures. The ten fold increase in reaction rate near 0.7 ML are most naturally understood in terms of geometrical effects such as island edges where the local bonding orbitals might be quite unique. It is interesting to note that Berlowitz *et al.*[26] have found a similar trend in studying the catalytic dehydrogenation reaction converting cyclohexane (C_6H_{12}) to benzene (C_6H_6) over Cu/Ru(0001). While the reaction rate is low on both the clean Ru surface and 1 ML Cu/Ru, the relative catalytic activity increases by a factor of 11 at ~3/4 ML of Cu on Ru(0001). They interpret this effect by emphasizing that the two metals may cooperatively catalyze different steps of the reaction at this submonolayer coverage.

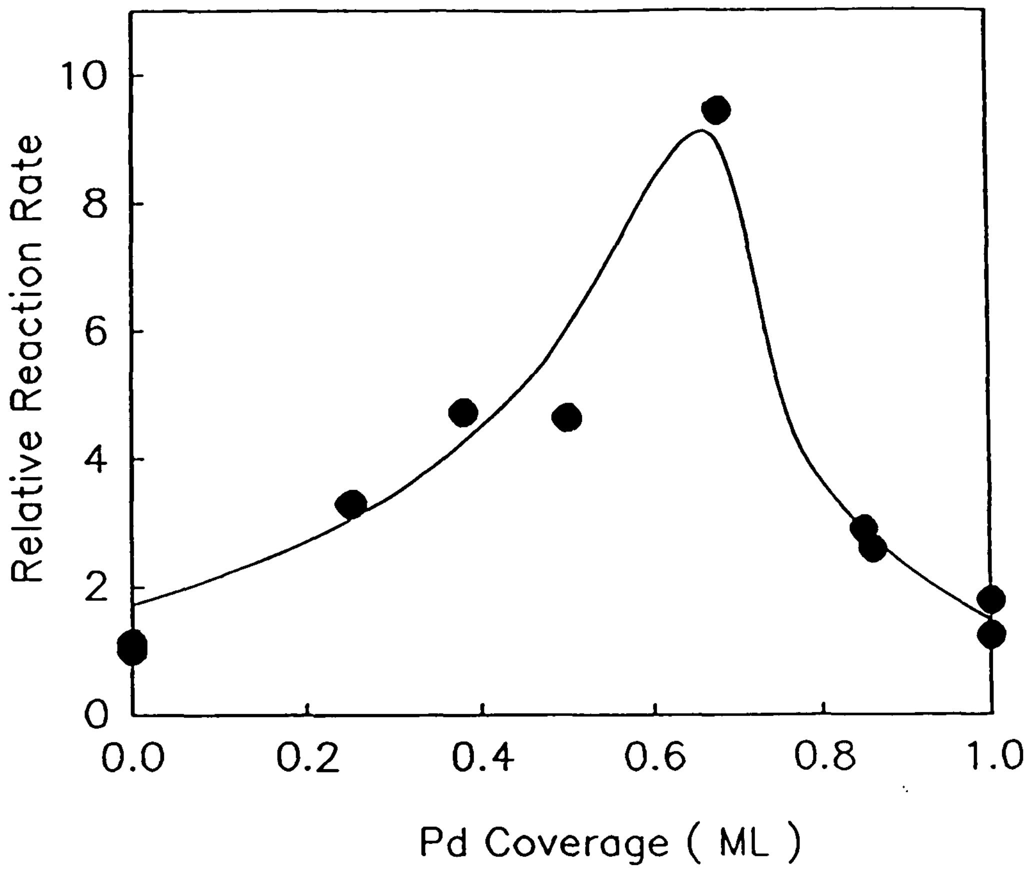

Figure 13. Relative reaction rate of the deuteration of C_3H_6 and H-D exchange over various coverages of Pd/Ta.

Chapter 3. Theoretical Aspects

3.1 Thin film growth modes.

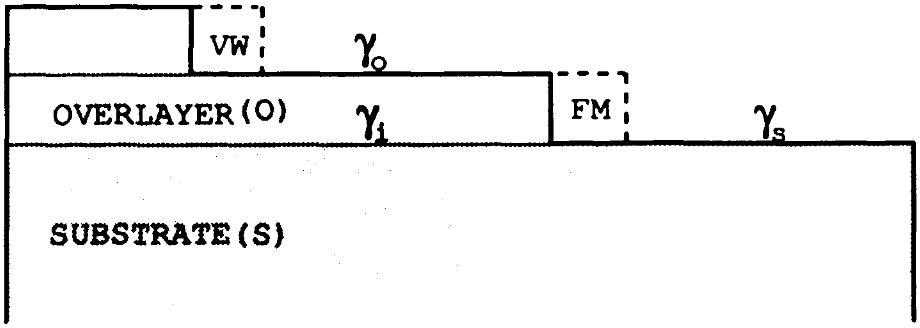

Figure 14. Substrate and two growing monolayers terminating at FM and VW illustrating the growth criteria.

It is generally recognized that thin films grow by one of three mechanisms: "three-dimensional islands" or the Vomer-Weber (VW), "layer-by-layer" or the Frank-van der Merwe (FM), and "layer-plus-three dimensional islands" or the Stranski-Krastanov (SK) mode, depending on the relative magnitudes of surface energies γ_o, γ_s of the overlayer and substrate respectively, and of the interface energy γ_i. If the free energy of the overlayer-substrate system is less when an additional adatom is added at FM rather than at VW in Fig. 14, two-dimensional growth will be preferred. Bauer's criteria[27] are thus obtained and it may be summarized as follows:

$$\Delta E = \gamma_o - \gamma_s + \gamma_i \begin{cases} \leq 0, & \text{FM} \\ > 0, & \text{VW} \end{cases} \tag{3.1}$$

where the equality may represent the growth of a material on itself. When $\Delta E \leq 0$ is satisfied initially followed by $\Delta E > 0$ at a certain thickness, SK mode occurs which corresponds to initial FM growth followed by VW type growth. If γ_i is large and negative, and compounds or alloys of the two metals exist with a large heat of formation, then interdiffusion and compound or alloy formation may occur at the interface, even at room temperature. This mode of growth is not well recognized and the tendency is higher if $\gamma_o > \gamma_s$ as will be illustrated in the following chapter.

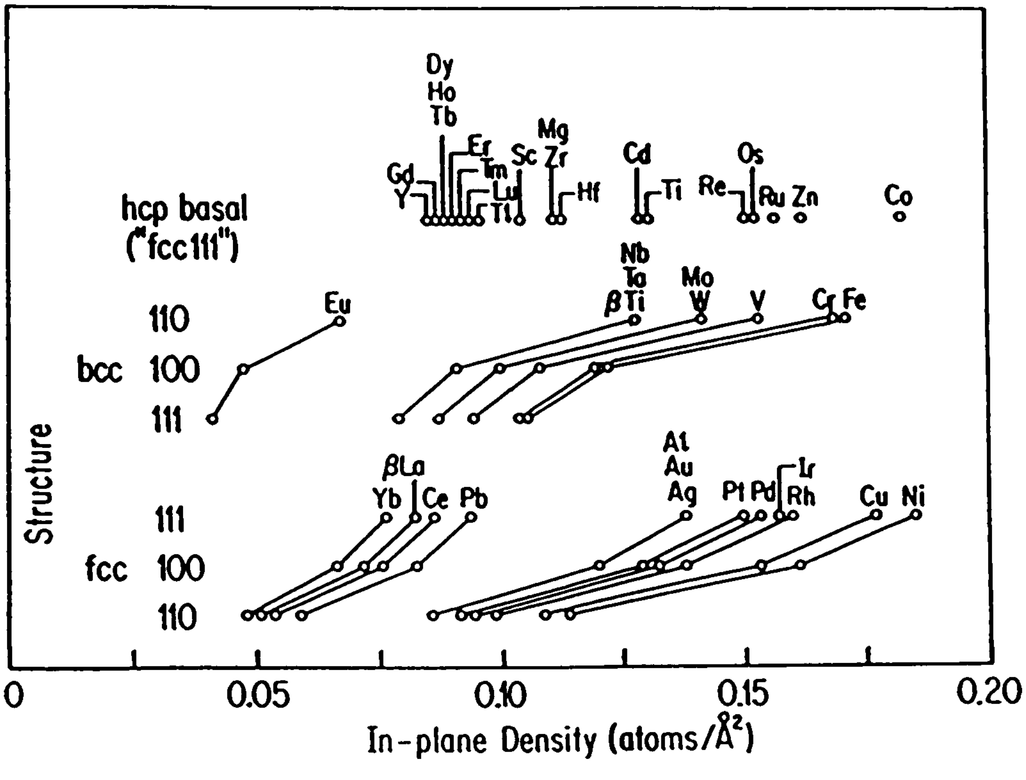

Figure 15. In-plane density of atoms for various orientations of typical fcc and bcc metals as well as the hcp basal plane.

In Eq. (3.1), γ_i also contains the structural distortion energy due to lattice mismatch at the interface. The mismatch of the in-plane density of atoms (N) can provide an average measure of the lattice mismatch if the overlayer and substrate have different structures. The fcc(111)/bcc(110) interfaces are the major concern of this thesis and N can be calculated using the inverse of the unit cell area S,

$$N = \frac{1}{S} = \begin{cases} \dfrac{1}{\frac{\sqrt{3}}{2}\left(\frac{a_{fcc}}{\sqrt{2}}\right)^2} = \dfrac{4}{\sqrt{3}\,a_{fcc}^2}, & \text{fcc(111)} \\ \dfrac{1}{\frac{a_{bcc}}{\sqrt{2}}a_{bcc}} = \dfrac{\sqrt{2}}{a_{bcc}^2}, & \text{bcc(110)} \end{cases} \tag{3.2}$$

where a_{fcc} and a_{bcc} are the lattice constants of the fcc and bcc elements respectively. Figure 15 plots N for various orientations of typical fcc and bcc metals as well as the hcp basal plane to serve as a guide to interfacial lattice mismatch.

Experimental surface energies are often not obtained much more directly than semiempirical estimates and are only well tabulated for liquid metals. According to Mezey and Giber[28], the sublimation of a solid can be imagined to consist of two parts. First, by breaking up all the bonds between the atoms, a mole of solid is changed into a monatomic perfect gas of noninteracting atoms compressed to the solid volume V_s. Secondly, this hypothetical system is allowed to expand to the perfect gas volume V=RT/P in an isothermal process. The energy needed in the first part H_i, can be considered as the molar internal free enthalpy. The enthalpy change of the second process can be obtained from the following known thermodynamic equation:

$$H_v = RT\ln(V_s/V). \tag{3.3}$$

Then H_i can be determined from the molar heat of sublimation H_s as follows:

$$H_i = H_s + RT\ln(RT/PV_s). \tag{3.4}$$

Surface-creating is a bond-cutting process and the surface energy can be related to H_i by counting the differences in bond numbers:

$$\gamma \equiv \frac{\alpha_i H_i}{A} = \frac{1}{A}\frac{\sqrt{z_b} - \sqrt{z_1}}{\sqrt{z_b}} H_i = \frac{\sqrt{z_b} - \sqrt{z_1}}{A\sqrt{z_b}} \left(H_s + RT\ln\frac{RT}{PV_s} \right) \tag{3.5}$$

where A is the molar surface area, z_b and z_1 are the coordination numbers (defined as the sum of the first neighbor number and half of the second neighbor number) of the bulk and first layer respectively. The calculated values of α_i are 0.231, 0.147 and 0.293 for the (100), (110) and (111) faces of the bcc structure, and 0.163, 0.225 and 0.163 for the (100), (110) and (111) faces of the fcc structure respectively. The average values of α_i, based on experimental data of γ for a number of polycrystalline metals, are 0.197 and 0.205 for bcc and fcc metals respectively. Both values compare favorably with the geometrical averages of the two lowest index theoretical values of 0.184 and 0.192 respectively.

Bauer's criteria can give good general guidelines although its predictive power is often limited for two reasons: (1) the bulk γ_0 values are not good approximations for a monolayer whose electronic structure can be strongly modified by the interaction with the substrate, (2) the interface energy is poorly known even for interfaces between bulk crystals.

Recently total energy multilayer and slab calculations have been performed to calculate surface and interface energies from first-principles[3]. In the case of a multilayer system A_nB_n, there are no free surfaces. Expressing γ_i in terms of pure interface energy ξ and structural distortion energy, ΔE is then given by

$$2n\Delta E = 2\xi + n\left(\Delta E^A_{str} + \Delta E^B_{str}\right)$$

or

$$\Delta E = \frac{\xi}{n} + \frac{1}{2}\left(\Delta E^A_{str} + \Delta E^B_{str}\right). \tag{3.6}$$

The structural energies can be determined at the limit of infinitely thick layers where,

$$\Delta E = \frac{1}{2}\left(\Delta E^{A}_{str} + \Delta E^{B}_{str}\right) \qquad \text{as } n \to \infty. \tag{3.7}$$

The interface energy can then be derived from Eq. (3.6) given the structural energies and ΔE which can be determined by band structure calculations.

Table I. Surface energies of selected metals γ (J/m^2)

	Ag	Al	Pd	Rh	Nb	Ta	Mo
Semiempirical (Polycrystalline)	1.38	1.15	2.17	2.94	3.10	3.09	2.96
First Principles (110) surface	1.40		2.5		2.9		

Multilayer calculation is a bulk technique and surface energies can not be calculated in this way. Surface effects can be investigated by calculating the total energies of a n-layer slab of metal B with and without a layer of metal A on each side (slab calculation). The adhesion energy of A on B, defined as the difference in energy between a B surface covered by a monolayer of A and a bare B surface plus a ball of bulk metal A, can be written as

$$\Delta E = \frac{1}{2}E\,(AB_nA) - \frac{1}{2}E\,(B_n) - E_{bulk}\,(A) \tag{3.8}$$

The bulk energy E_{bulk} can be determined by calculating the total energies for slabs of various thickness (typically seven and nine layers) assuming that the total energy for an n-layer slab of an elemental metal is given by:

$$E(n) = nE_{bulk} + 2\gamma. \tag{3.9}$$

ΔE and the surface energy, γ can then be determined from first principles. The surface energies of the (110) surface of Ag, Pd and Nb calculated in this way and of the polycrystalline surfaces derived from semiempirical calculations at T=0 for several metals relevant to this thesis are given in Table I. Reasonable agreement between the two methods can be seen.

Multilayer calculations indicate that the Ag-Nb(110) interface energy is positive, consistent with the nonbonding nature of the Ag-Nb bulk phase diagram. Slab calculations show a adhesion energy of Ag on Nb(110) of -0.3 eV/adatom. Thus, it is the surface energy contribution that explains the FM growth found experimentally in this system[29].

Experimentally the growth mode can be determined by monitoring the Auger signal intensities of both the overlayer and the substrate as a function of deposition time, or coverage estimated with a thickness monitor or TPD, etc. It can be shown that the monolayer thicknesses of fcc(111) and bcc(110) films are $a_{fcc}/\sqrt{3}$ and $a_{bcc}/\sqrt{2}$ respectively. FM growth is characterized by linear segments or slope breaks at the completion of each layer, the SK mode by only one break followed by smooth exponential behavior, VW mode or interdiffusion by no break but a smooth curve. LEIS can also be used to determine the growth by monitoring the composition of the top layer as a function of coverage. Photoemission and LEED measurements on the evolution of the surface electronic and geometrical structure and work function can often provide complementary information about growth modes.

It should be kept in mind that equilibrium considerations have been applied in the description of growth in this section. In practice, the surface mobility of condensing atoms is frequently too small or the activation energy for restructuring of an aggregate once formed is too high to permit the equilibrium configuration to be reached. Pseudo-FM or pseudo-SK growth may then occur. This can be determined by studying growth at various temperatures or by annealing at higher temperatures.

3.2 Epitaxial Orientations at the fcc(111)/bcc(110) interfaces

The last section concerns the stacking of the overlayer along the direction perpendicular to the surface and the surface energies play a crucial role. This section deals the arrangement of the overlayer atoms within the plane parallel to the surface and the interface energy is the dominating factor. The fcc(111) and bcc(110) are the most closely-packed planes of fcc and bcc metals and they are the "bricks" of most bimetallic superlattices. The fcc(111)/bcc(110) interfaces have attracted great interest not only because of their own physical and chemical properties but also because they are the unit cells of superlattices. We will devote our attention to the epitaxial orientations at the fcc(111)/bcc(110) interface.

First, both the fcc(111) adlayer and the bcc(110) substrate are assumed to be rigid (rigid-lattice approximation) so that the total adsorbate-substrate interaction per adatom can be written as:

$$V_{as} = \frac{1}{N_a} \sum_{i}^{N_a} \sum_{j}^{N_s} V(\mathbf{r}_i, \mathbf{r}_j) = \frac{1}{N_a} \sum_{G} V_G \sum_{i}^{N_a} e^{-i\mathbf{G}.\mathbf{r}_i} \tag{3.10}$$

where **G** is the reciprocal lattice vector of the substrate surface, N_a and N_s are the total number of overlayer and substrate atoms respectively. Using the Morse potential as the two-body interatomic potential (in Lennard-Jones units)

$$V(r) = 4\,\varepsilon\, e^{-\frac{8}{3}(r^2-1)}\left[e^{-\frac{8}{3}(r^2-1)} - 1\right], \tag{3.11}$$

the Fourier coefficient of the substrate potential can be written as

$$\begin{aligned} V_G &= \frac{1}{v_s} \int d^2\mathbf{R}\; V(r)\, e^{-i\,\mathbf{G}\cdot\mathbf{R}} \\ &= \frac{3\pi}{4} \frac{\varepsilon}{v_s} \left[e^{-\frac{3}{64}|G|^2} e^{-\frac{16}{3}(z^2-1)} - 2\, e^{-\frac{3}{32}|G|^2} e^{-\frac{8}{3}(z^2-1)} \right] \end{aligned} \tag{3.12}$$

where v_s is the area of a unit cell of bcc(110) lattice, **r**=**R**+**z**, **R** is the two dimensional surface vector, **z** is perpendicular to the surface and $|z|=1$ is usually assumed.

Figure 16 shows V_{as} for $N_a=121$, as calculated by Kobayashi and Das Sarma[30] using the above procedure, as a function of atomic diameter ratio r=a/b [$a= a_{fcc}/\sqrt{2}$ and $b=(\sqrt{3}/2)a_{bcc}$] for $\theta=0°$, 5.26° (60-arctan$\sqrt{2}$) and 30° respectively. Four relative displacements (i.e., the central atom of the overlayer) are indicated by A, B, C and D. For $\theta=0°$, two major minimums are seen at 0.943 and 1.155, corresponding to the two cases of the Nishiyama-Wassermann (NW) orientation, NW-x and NW-y. For $\theta=5.26°$, only one major minimum is seen at 1.089, corresponding to the two equivalent Kurdjumov-Sachs (KS) orientations, $[1\bar{1}0]_{fcc} \parallel [1\bar{1}1]_{bcc}$ and $[\bar{1}01]_{fcc} \parallel [\bar{1}11]_{bcc}$. The major minimum seen at 1.333 for $\theta=30°$ is called the R30° orientation. All these basic orientation relationships correspond to the row matching of certain rows in fcc(111) and bcc(110) planes and they are shown in Fig. 17.

For over fifty years, KS and NW orientations were the only ones observed experimentally at the fcc(111)/bcc(110) interfaces. Recently the R30° orientation has been observed by Homma, Yang and Schuller[31] in studies of the growth of Ce(111)/V(110) and thereafter the R30° is also called HYS orientation.

It is interesting to note that the depth of energy minimum is largest for KS orientation because the atomic rows in KS layer pass through the substrate potential minimum (D) while the atomic rows in other orientations do not (B, C, C for NW-x, NW-y and HYS respectively). It should also be mentioned that the KS orientation is not suitable for crystalline superlattice formation because each stack of A or B adds additional azimuthal orientations.

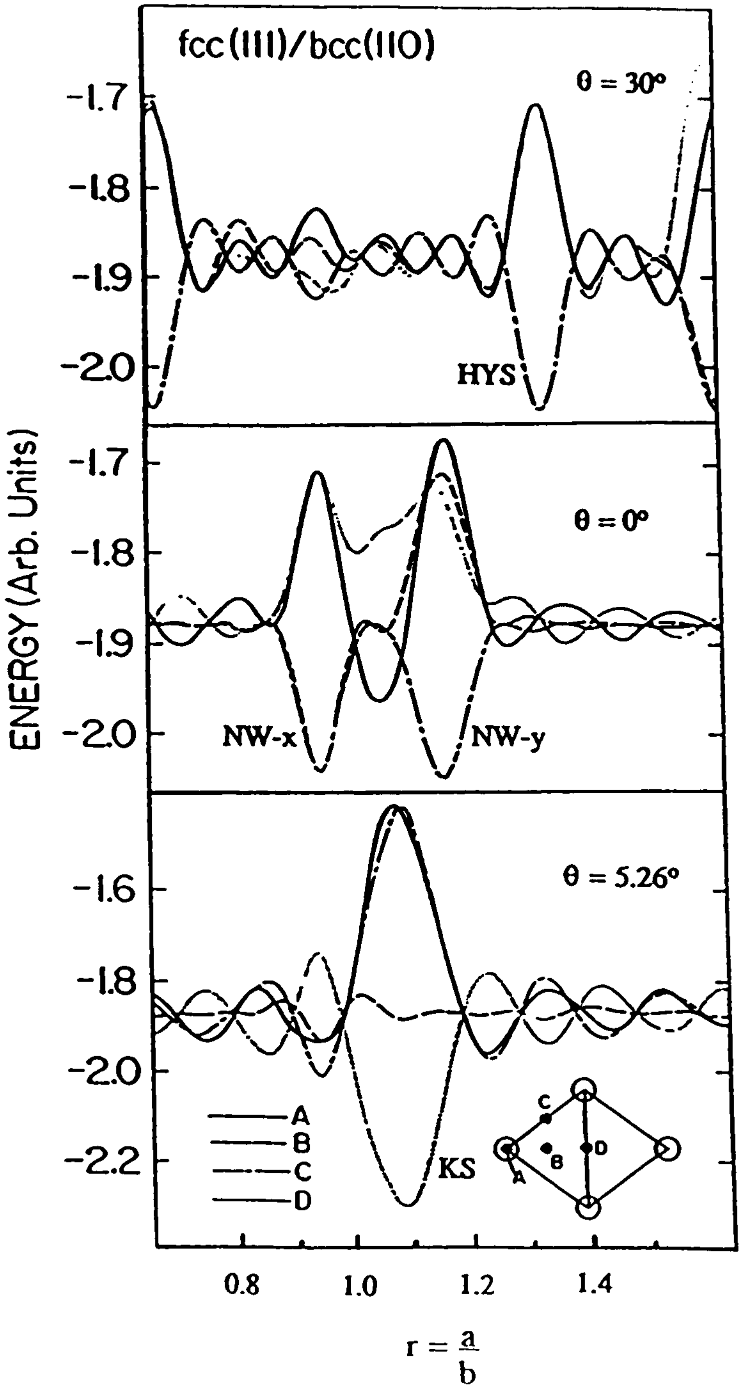

Figure 16. Interface energy vs atomic diameter ratio for various relative orientations and displacements.

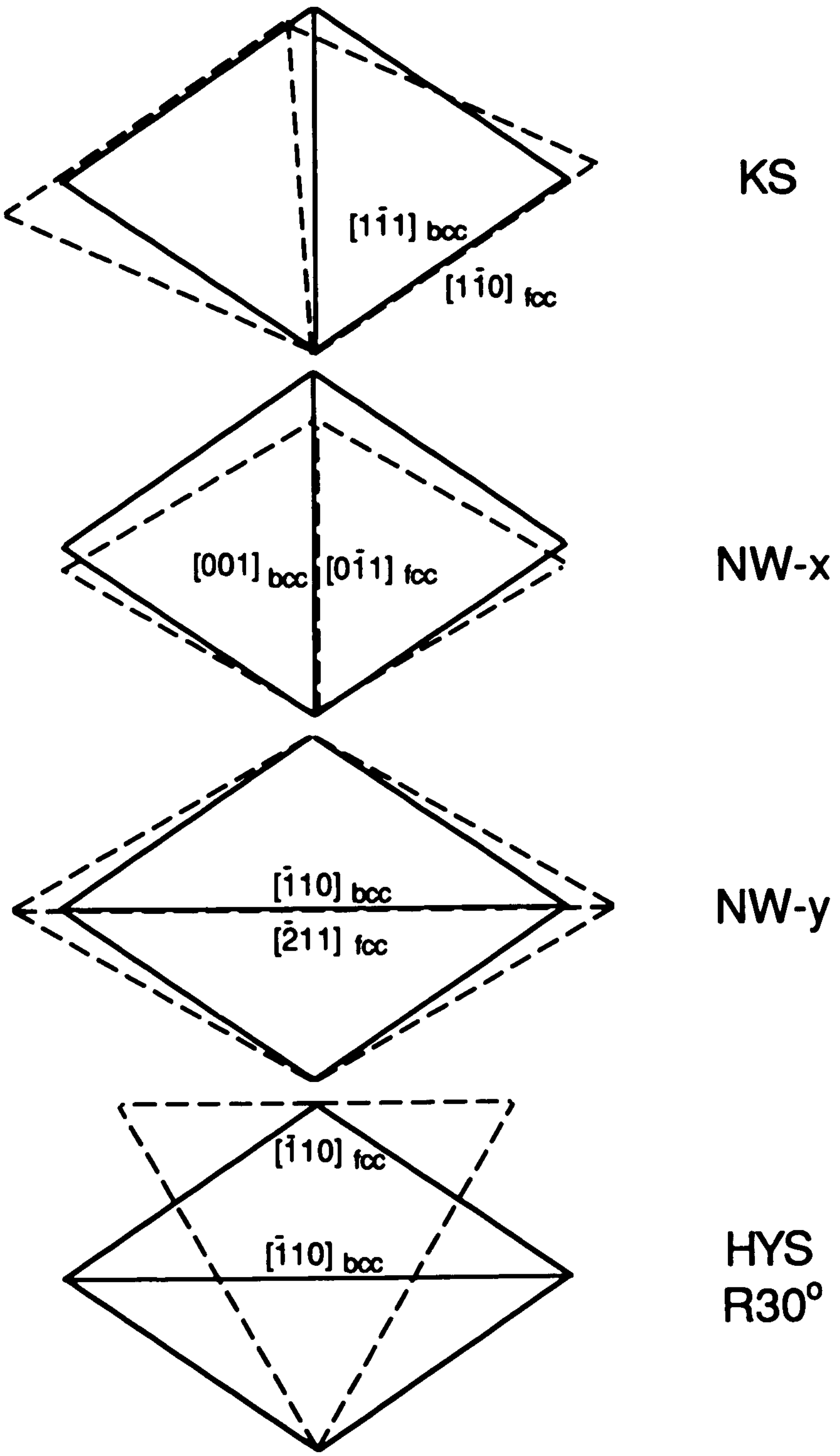

Fig. 17. Basic orientations at fcc(111)/bcc(110) interfaces

A more convenient way to calculate V_{as} is to map all the overlayer atoms into the substrate unit cell. For a large system, the summation over i can be converted to an integration over the unit cell:

$$V_{as} = \sum_{G} V_G \frac{1}{V_s} \int_{cell} dr\, f(r)\, e^{-iG.r}\, e^{-iG.r_o} \tag{3.13}$$

where f(r) is the distribution function and r_o is the origin of the overlayer. Applying this "mapping technique", recently introduced by Paik and Schuller[32], and defining "order" as the leading-order term in the Fourier series of the a-s interaction, KS and NW-x orientations have been found to correspond to first and second order axial commensuration, while NW-y and HYS are both third order. The depth of the energy minima for higher order axial commensuration are so small that they cannot be distinguished from incommensurate cases.

To find an explicit analytical formula for the size-dependent V_{as}, consider a circular fcc(111) island of radius R with an atomic diameter ratio r. The distribution function for this island in an orientation corresponding to the ideal value of r_c can be approximated by

$$f(r) = \begin{cases} \frac{4}{\pi x_o}\sqrt{1-\left(\frac{x'}{x_o}\right)^2}, & \left|\frac{x'}{x_o}\right| \le 1 \\ 0, & \left|\frac{x'}{x_o}\right| > 1 \end{cases} \tag{3.14}$$

along the commensurate axis (x'), while f(r) is constant along the incommensurate axis (y'). In this expression, x_o=cRb(r-r_c)/a, and c is a constant that depends on the epitaxial orientation. After integration of Eq. (3.13) with the above f(r), the size-dependent V_{as} becomes

$$V_{as} = 2\sum_{G} V_G \frac{J_1(\alpha_G \Delta r)}{\alpha_G \Delta r} \delta_{G_\perp} = 2\sum_{n=1}^{\infty} V_{G_n} \frac{J_1(\alpha_n |r-r_c|)}{\alpha_n |r-r_c|} \qquad (3.15)$$

where J_1 is the Bessel function of the first kind, G_n and $G_\perp$ denote the reciprocal-lattice vectors of the substrate surface parallel and perpendicular to the axial commensurate direction, and $\alpha_n = c|G_n| Rb/a$.

For a short range potential such as Morse potential, V_G converges rapidly to 0 as G increases. Thus, only the leading order term for each orientation is important and Eq. (3.15) provides an efficient way to calculate V_{as}. The key parameters for each orientation are listed in Table II where the leading order Fourier coefficient V_G is derived from Eq. (3.12) assuming z=1. The ratio of V_G between KS and NW-x orientation (8/3) agrees well with the ratio of the depth of energy minimum between KS and NW orientations in Fig. 16.

Table II. Parameters for the first four lowest-order axial commensurate fcc(111)/bcc(110) systems.

Orientation	θ	r_c	α_n	G_n	V_G^1
KS	5.26°	$\frac{4\sqrt{2}}{3\sqrt{3}}$	$\frac{3\sqrt{3}n\pi R}{2\sqrt{2}a}$	$\frac{\sqrt{3}n\pi}{b}(1,\frac{1}{\sqrt{2}})$	-0.08
NW-x	0°	$\frac{2\sqrt{2}}{3}$	$\frac{3\sqrt{2}n\pi R}{2a}$	$\frac{\sqrt{3}n\pi}{b}(0,\sqrt{2})$	-0.03
NW-y	0°	$\frac{2}{\sqrt{3}}$	$\frac{2\sqrt{3}n\pi R}{a}$	$\frac{\sqrt{3}n\pi}{b}(2, 0)$	-0.004
HYS	30°	$\frac{4}{3}$	$\frac{3n\pi R}{a}$	$\frac{\sqrt{3}n\pi}{b}(2, 0)$	-0.004

The experimental observation of KS, NW or HYS orientations does not mean that the natural atomic-diameter ratio precisely satisfies the row-matching condition. In general, there is a non-zero misfit and epitaxy occurs because the overlayer distorts somewhat to achieve row-matching. Clearly the approach has to be extended beyond the rigid-lattice approximation to predict the orientation of a given fcc(111)/bcc(110) interface. This is done by van der Merwe[33] who assumes harmonic interactions (harmonic approximation) between adatoms with the same structures and equilibrium distances as the closely packed fcc(111) plane in the bulk. The bcc(110) substrate is maintained rigid and the elastic interaction between the overlayer atoms competes with the periodic substrate potential which is approximated by a truncated Fourier series:

$$\begin{aligned}\frac{V(x,y)}{W} = A - A_1\cos\left[2\pi\left(\frac{x}{b_x}+\frac{y}{b_y}\right)\right] - A_2\cos\left[2\pi\left(-\frac{x}{b_x}+\frac{y}{b_y}\right)\right] \\ - A_3\cos\left[4\pi\frac{x}{b_x}\right] - A_4\cos\left[4\pi\frac{y}{b_y}\right]\end{aligned} \tag{3.16}$$

where $b_x=2\sqrt{2}b/\sqrt{3}$, $b_y=2b/\sqrt{3}$. The Fourier coefficients have been chosen as $A_1=A_2=0.4$, $A_3=0.12$, $A_4=0.08$, $A=A_1+A_2+A_3+A_4=1$ and they are proportional to the depths of energy minimum of the ideal epitaxial orientations under the rigid-lattice approximation:

$$\Delta\bar{V} = \begin{cases} WA, & \text{2DC} \\ WA_1 = WA_2, & \text{KS} \\ WA_{3,4}, & \text{NW-x, NW-y.} \end{cases} \tag{3.17}$$

The elastic energy between overlayer atoms can be written as:

$$\varepsilon = W\ell^2 r^2\left(e_x^2 + e_y^2 + 2Pe_xe_y + Re_{xy}^2\right) \tag{3.18}$$

where

$$\ell^2 = \frac{\Omega S}{Wr^2},\ S = \frac{c_{11}^2 - c_{12}^2}{2c_{11}},\ P = \frac{c_{12}}{c_{12}+c_{11}},\ R = \frac{c_{11}c_{44}}{c_{11}^2 - c_{12}^2},$$

and Ω is the volume per overlayer atom, e's are the strain components, c's are the elastic constants of the overlayer and they are assumed to be the same as the corresponding bulk values. Since S is a measure of the strain energy density for a given strain and W is a measure of the overlayer-substrate interaction, ℓ expresses the relative strength of the intralayer to layer-substrate interactions. The balance between the intralayer and layer-substrate interaction will yield the stability limit. A structural phase diagram obtained in this way by Bauer and van der Merwe[2] is shown in Fig. 18. If ℓ is very small, i.e., layer-substrate interaction is much stronger than the intralayer interaction, 2DC (pseudomorphic) will prevail independent of r. As ℓ increases, other configurations dominate depending on the exact value of r and ℓ. This diagram has successfully explained a vast variety of experimental findings including the observation of Pd(111) on Nb(110) ($r=0.963$) in NW-x orientation preceded by a pseudomorphic layer. If the rigidity modulus of a n layer film may be approximated by n times the monolayer elastic constants, the transition from monolayer to multilayer will be characterized by a change of $\ell \rightarrow \sqrt{n}\,\ell$. This allows an immediate prediction of the evolution of the film structure with thickness. Orientation change is allowed during growth for systems near the NW-y region. To the best of my knowledge, no clear cut experimental evidence exists in literature about the orientation change. In chapter 5, a first observation of a KS-NW (-x) orientation transition during the growth of Rh(111)/Mo(110) will be presented and it will be discussed in terms of this layer-thicking effect as well as the finite-size effect as indicated by Eq. (3.15) from the "mapping technique".

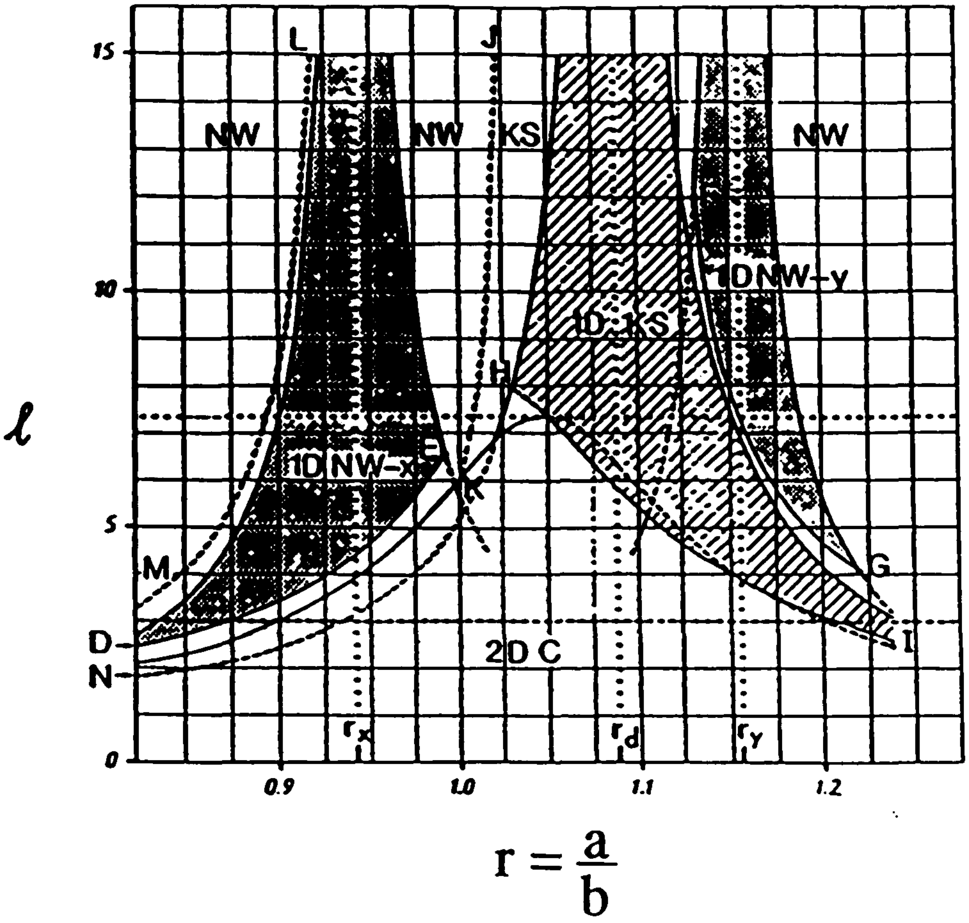

Figure 18. Theoretical structural phase diagram of fcc(111)/bcc(110) interfaces.

3.3 A Criterion for the Charge Transfer between an adatom and a metallic substrate

Charge transfer between atoms in molecules or solids is an important process in various physical phenomena and chemical reactions. The concept of electronegativity (X) has been proposed to describe the ability of an atom to attract electronic charge. X is a very useful concept in understanding the charge transfer process but is so poorly defined that many physics textbooks do not even mention it. There are many different definitions of X in the literature[34] and Pauling's electronegativity scale has been so far the most widely used. We are particularly interested in charge transfer between an adatom and a metallic substrate because the direction of this electronic charge transfer will determine the sign of the surface work function change, $\Delta\phi=-4\pi enp$, where n is the adatom density and p is the charge transfer induced dipole moment. If the electronic charge transfer is from the adatom to the substrate, p will be positive and ϕ decreases; if the charge transfer is from the substrate to the adatom, p will be negative and ϕ increases.

One complication of this picture comes from surface roughening which may give rise to the so-called Smoluchowski effect[35]. Figure 19 shows the electrical double layer at (a) an atomically smooth surface and (b) an atomically stepped surface. If a metal surface is completely planar as in Fig. 19(a), the electron cloud in the interior will not terminate there abruptly since this would correspond to an infinite kinetic energy. Instead, there will be a gradual decay to zero with the result that the electron cloud extends outside the metal surface, leaving an electron deficiency within the metal. This causes the work functions of close-packed crystal faces to be higher than loosely packed or atomically rough faces.

The measurement of the work-function change due to adsorption on a metallic substrate is one of the simplest techniques used in surface science. Although work-function changes have been routinely measured in studies of metal overlayers, its understanding is still poor. For example, Pd has a higher Pauling electronegativity than

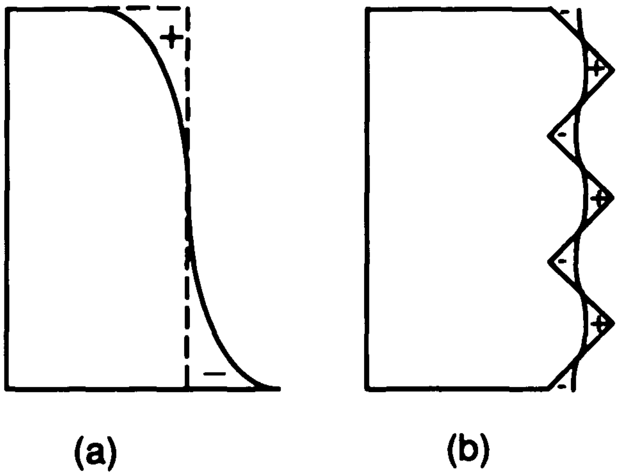

Figure 19. Charge distribution at a metal surface: (a) an atomically smooth surface; (b) an atomically stepped surface.

Nb and Pd(111) has a higher work function than Nb(110), yet the adsorption of Pd on Nb(110) actually reduces the work function initially[36]. This type of behavior is frequently observed for many other systems as well, e.g., Pd, Ni, Cu, and Ag on W(110), and it is a long-standing unanswered question[37]. Sometimes it is attributed to the adatom-induced roughening which may lower the work function as shown above. On the other hand, the adsorption of Au on W(110) increases the work function[37]. Obviously the electronic charge transfer between adatom and substrate, and especially whether the charge transfer is from the substrate or from the adatom, are important to explain the initial trends in the work-function changes and we emphasize that this is not properly described by the Pauling electronegativity or work function. In this section, a simple criterion will be proposed for the direction of electronic charge transfer between an adatom and a metallic substrate.

First, consider a point charge q at **r** in the presence of a grounded metal with a surface (S) of arbitrary shape, the charge distribution $\sigma(\mathbf{r}')$ over the metal surface induced by q will satisfy the image condition that the potential at any point ($\mathbf{r}'$) of the metal surface is zero:

$$\frac{q}{|\mathbf{r}-\mathbf{r}'|} + \int_S \frac{\sigma(\mathbf{r}'')}{|\mathbf{r}'-\mathbf{r}''|} dS'' = 0 \tag{3.19}$$

The image interaction energy is the total energy of the system:

$$V_i(\mathbf{r}) = q\int_S \frac{\sigma(\mathbf{r}')}{|\mathbf{r}-\mathbf{r}'|} dS' + \frac{1}{2}\int_S \int_S \frac{\sigma(\mathbf{r}')\sigma(\mathbf{r}'')}{|\mathbf{r}'-\mathbf{r}''|} dS' dS'' = \frac{1}{2}q\int_S \frac{\sigma(\mathbf{r}')}{|\mathbf{r}-\mathbf{r}'|} dS' = \frac{1}{2}V(\mathbf{r}) \tag{3.20}$$

where

$$V(\mathbf{r})=q\int_S \frac{\sigma(\mathbf{r}')}{|\mathbf{r}-\mathbf{r}'|} dS' \tag{3.21}$$

is the potential energy of q when $\sigma(\mathbf{r}')$ is a fixed charge distribution rather than the q-induced image charges. Eq. (3.20) can be considered as a theorem on image interaction energy because it is a general relationship between $V_i(\mathbf{r})$ and $V(\mathbf{r})$ independent of conductor shape. For an infinite planar surface, the factor 1/2 has been derived by direct calculations in many electrodynamics textbooks.

Now consider an atom near a metal surface (Fig. 20). The affinity level A will be shifted down due to the image attraction of the excess electron on the atom,

$$A' = A + |V_i|. \tag{3.22}$$

The ionization potential I of the neutral atom will be shifted up by the same amount because the ionized electron feels not only its own image, but also the image of the ion core which should be considered as a fixed charge distribution and contributes a repulsion energy $|V|=2|V_i|$ according to Eq. (3.20), as the ionized electron moves to infinity:

$$I' = I + |V_i| - |V| = I - |V_i|. \qquad (3.23)$$

In the case of a planar metal surface, $|V_i| = \frac{1}{2}\frac{e^2}{2d} = 3.6/d$ (eV) when the atom to the metal image plane distance d is expressed in (Å).

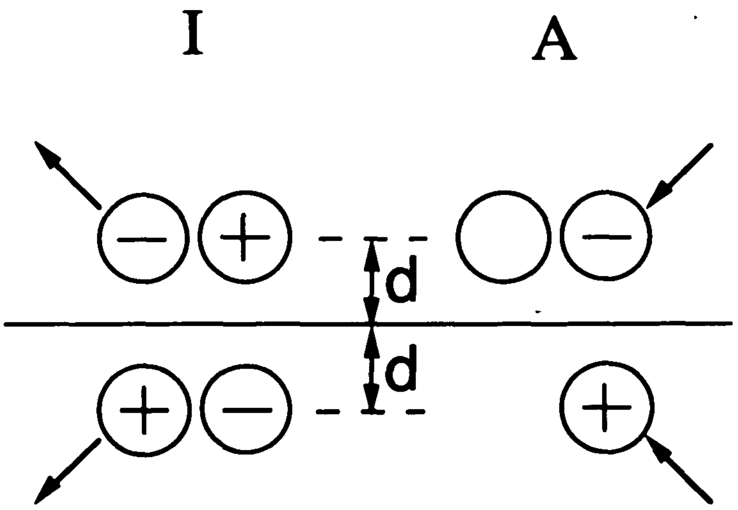

Figure 20. The ionization and electron attachment processes of an atom near a metal surface.

So far the shifts of A and I of an atom adsorbed on a metal surface have been derived by classical electrostatics. Its validity depends on the lifetime of an electron in the adatom orbital and the dielectric response of the metal surface. However, the quantum-mechanical treatments for the upward shift of I indicate that the classical result, which corresponds to instantaneous response, is a good approximation when the surface plasmon energy of the metal is significantly larger than $|V_i|$ and the energy spread, which is the case for most metals[38].

Next consider the electronic charge transfer between an adatom and a metallic substrate. Figure 21 shows the schematic diagram of the involved energy levels. The affinity level A and ionization potential I are shifted when an adatom is brought to a metal surface, $A'=A+|V_i|$ and $I'=I-|V_i|$. The energy changes due to electronic charge transfer are

$$E_{sa} = \phi - A' , \tag{3.24}$$

from substrate to adatom, and

$$E_{as} = I' - \phi , \tag{3.25}$$

from adatom to substrate. We introduce a charge transfer parameter,

$$J = (E_{as} - E_{sa})/2 = (I + A)/2 - \phi = X_m - \phi \tag{3.26}$$

where $X_m=(I+A)/2$ is the Mulliken electronegativity.[39] If $J<0$, electronic charge transfer from adatom to substrate is energetically favored, and the work function decreases. If $J>0$, electronic charge transfer from substrate to adatom will be favored, and the work function increases. As X_m is a constant and ϕ may change with coverage until $J=0$, the value of J can be roughly considered as an upper limit of possible work-function changes. Furthermore, a maximum or minimum in the plot of work-function change versus coverage may indicate the onset of a structural transition from individual adatoms to condensed islands.

For alkali metals X_m ranges from 2.2 to 3 eV[40] (Cs to Li), while ϕ is between 4 and 6 eV for most metal substrates, J is then between -1 to -3.8 eV, and thus the adsorption of alkali metals on metallic substrates could reduce the work function by 1 to 3.8 eV (Li to Cs). This trend agrees well with the experimental observations of, for example, maximum work function reductions of 2.65, 3.02 and 3.18 eV for the adsorption of Na, K and Cs respectively on Ta(110).[41] $|V_i|$ is known to be around 1.5 to 2.5 eV and I ranges from 3.9 to 5.4 eV for alkali metals, so the shifted valence level (3.9 - 1.4) is always above E_F, and charge transfer from alkali metals to the substrate is never a problem.

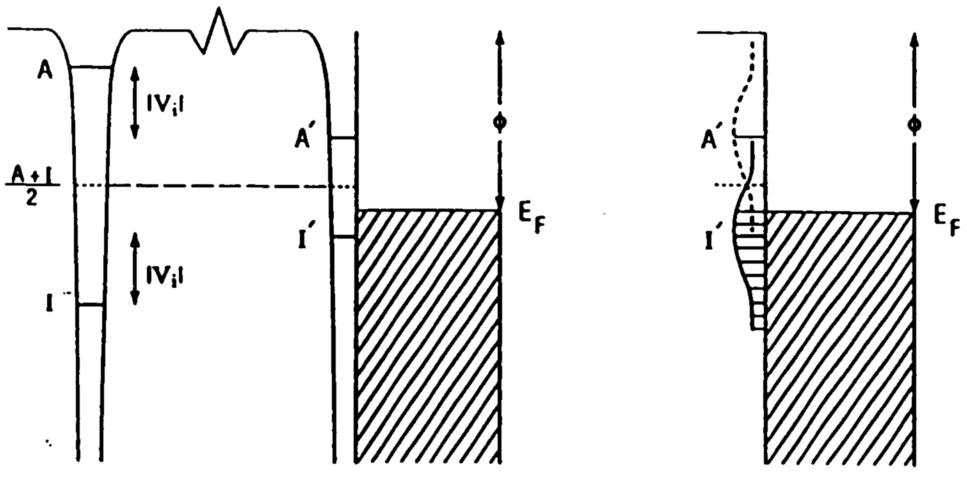

(a) (b)

Figure 21. Schematic representation of (a) shifts and (b) broadenings of electron affinity and ionization level due to adsorption on a metallic substrate.

The most frequently encountered case is shown in Fig. 21(a), i.e., I' lies below E_F and A' lies above E_F. The charge transfer will raise the system energy for both directions. However, one must note that the adatom-substrate interaction not only shifts A and I but also broadens them[42]; this is schematically shown in Fig. 21(b). It is seen that A' and I' now lie partially above and partially below E_F. In the special case of $J<0$ in the diagram, the unoccupied part of I' is larger than the occupied A' so that net charge transfer from adatom to substrate is expected. Some covalent and metallic character can also be seen from this diagram; however, the sign of J still points out the right direction of the net charge transfer. It is easy to show that this criterion holds, even considering the differences of the energy spread of A and I, if one remembers that tunnel broadening increases as the level moves closer to E_F. This criterion seems more reasonable if one notes that X_m is simply the work function of a small metal particle including a single atom[43].

As J can be calculated easily from the well-tabulated values of A, I,[40] and ϕ,[44] the sign of J serves as a very efficient criterion for the charge transfer in the adatom-substrate system. When these ideas are combined with appropriate considerations of roughening (for a smooth substrate) and smoothing (for a rough substrate), one can get a better understanding of the initial work-function change. As an illustration, Figure 22 shows the work-function change as a function of coverage for Ni, Pd, Pt, and noble metals on Nb(110). The Pt and Ni data are derived from Ref. 45 while the Pd and noble-metal data are taken from Refs. 36 and 29 respectively. The work-function increases at very low coverages of Pt and Au on Nb(110) can be explained by the positive values of J for these systems, while the initial decreases for Pd, Ni, Cu, and Ag on Nb(110) are supported by roughing as well as by their negative values of J. The initial work-function increases for Au on W(110) and decreases for Pd, Ni, Cu, and Ag on W(110)[37] can be understood similarly. The J criterion will be further tested against the experimental work-function changes of other systems in the following chapters and will also be used as a indication of the transition from an adatom gas to a condensed island.

Recently there has been much debate about the various definitions of electronegativity and a new definition, using only the ionization potentials, has been proposed.[34] We hope that our view of the charge transfer between adatom and metallic substrate will shed some new light on Mulliken's definition, which recognizes the importance of both electron affinity and ionization potential in an atom's ability to attract electronic charge.

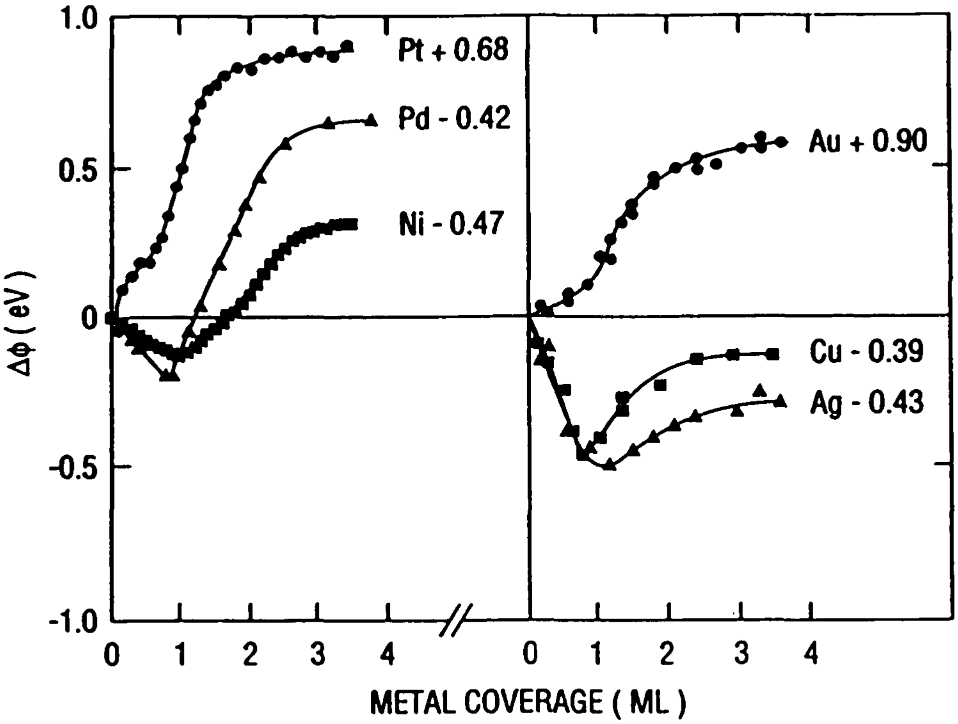

Figure 22. Work-function change vs coverage for Ni, Pd, Pt, and noble metals on Nb(110). The value of J calculated for each system is indicated.

Chapter 4. Evidence for room-temperature interface alloy formation

Alloying in many cases is related to high temperatures, and indeed most bulk alloys are formed by melting the constituents in a furnace. In studies of thin film growth, the data are routinely fitted into one of the three well-known growth mechanisms. Few worry about the possibility of alloying at room temperature or below. It fact, it has been generally assumed that alloying is insignificant up to the temperature at which volume diffusion sets in. However, thin films and interfaces represent new types of materials and they should not be expected to follow the bulk phase diagram. When a high surface energy metal is deposited on a low surface energy metal, one way to minimize the system energy is certainly the agglomeration of the adsorbate to reduce the surface area of the high surface energy material, which is why island growth is usually assumed in this case. This is expected for the growth of Nb on Ag because the surface energy of Nb is much higher than Ag and Nb-Ag is a nonbonding system. On the other hand, if the adsorbate-substrate is a strongly bonding system such as Pd/Al and Nb/Pd, another way of minimizing system energy becomes possible, i.e., by alloy or compound formation through interdiffusion. In this way, bonding energy can be gained while the surface energy cost can be reduced to some extent. Therefore island growth or alloying depends on the competition between the gain in bonding and the cost in surface energy.

Pd overlayers on Al(110) and Al(111) substrates have been studied by several groups and it has been claimed that Pd grows in layer-by-layer mode on Al(110) and in layer-plus-island mode on Al(111).[7] In both cases, a narrow, deep-lying *d* state centered at 4-5 eV below E_F was found and interpreted by assuming an atomiclike $4d^{10}5s^0$ configuration for Pd within the monolayer. Thus the interaction between Pd overlayer and Al substrates is considered weak due to the absence of strong *d-d* bonding and it is argued that the Pd monolayer on Al resembles an ideal free unsupported Pd monolayer. In this chapter, I will present evidence which actually suggests extensive intermixing between the deposited Pd and the Al substrate and the formation of Pd-Al intermetallic compounds at the surface. The alloying behavior is also discussed in the following section on Nb/Pd where comparison with first principle calculations will be made. The alloying at both interfaces demonstrates a common idea: when a high surface energy metal is deposited on a low surface metal and the bonding of the metal pair is strong, alloying may occur even at room temperature.

4.1 UPS studies of Pd/Al and Al/Pd

Figure 23 shows photoelectron energy distribution curves (EDC's) for a series of increasing Pd coverages on Al. These spectra are individually scaled to the maximum within the binding energy range shown. The Al substrate was prepared as a thin film on a Ta(110) foil and its spectrum is characterized by a small peak marked (f) extending from E_F to 4 eV below E_F due to the Al *sp* band. The absence of states 5-8 eV below E_F, where emission due to common impurities is often found, shows that the substrate is clean. The Pd coverages were monitored with a water-cooled quartz-crystal oscillator and calibrated with the UPS spectra of Pd/Ta(110)[25]. Depositing 1 ML of Pd reduces the intensity of peak (f) and induces a pronounced feature extending from 2.0 to 5.5 eV binding energy with centroid at 4.0 eV binding energy. Careful inspection of this feature suggests that it consists of at least two peaks, one at 4.8 eV marked (a) and the other at 3.6 eV marked (b). Doubling the Pd coverage increases the intensities of both peaks, and peak (b) grows faster and shifts to lower binding energy. At 4 ML coverage, a new Pd 4*d* induced peak centered at 1.3 eV binding energy marked (c) appears across E_F and dominates the spectrum, while peak (a) and (b) are still seen as shoulders on the high-binding-energy

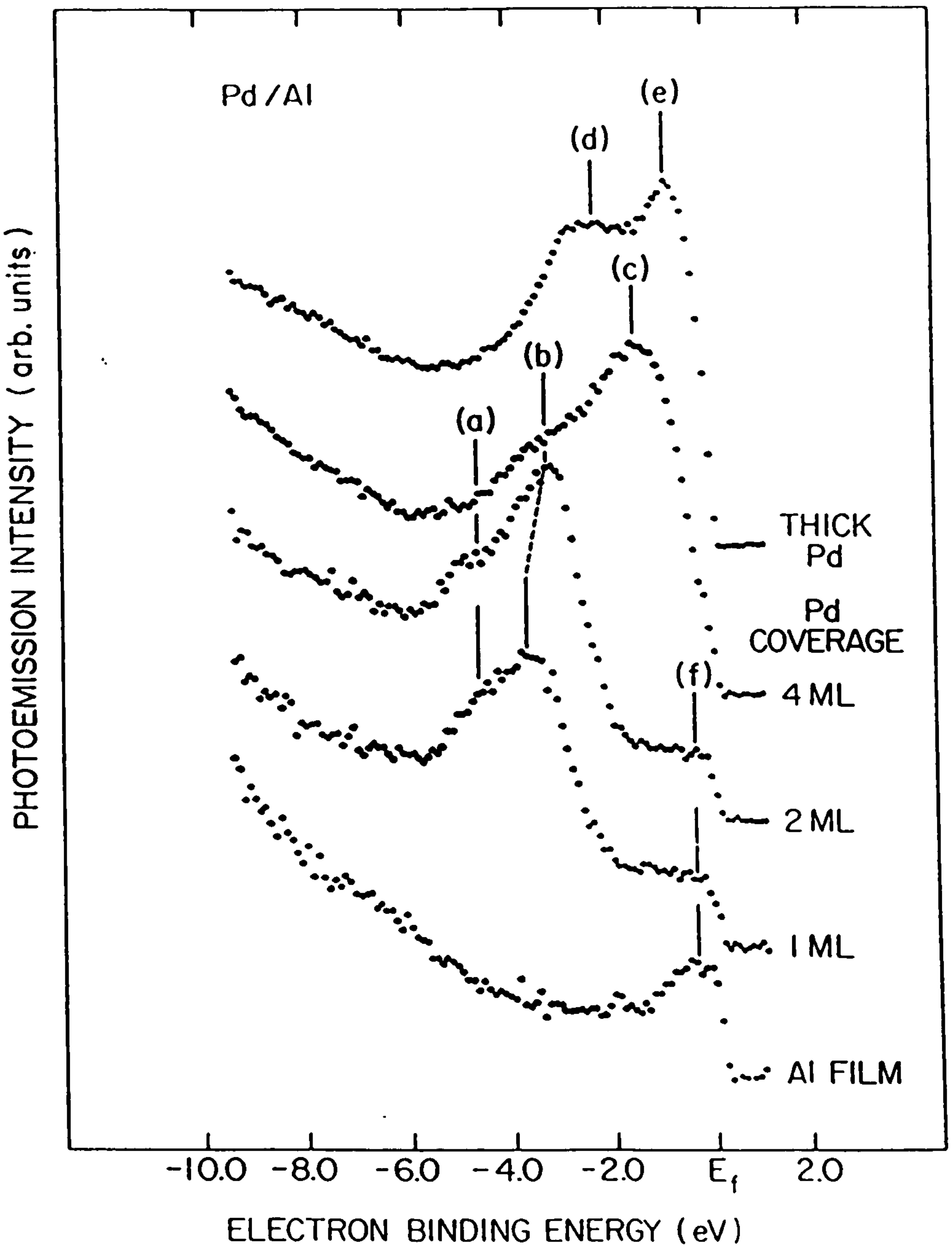

Figure 23. Photoemission spectra obtained with 21.2 eV photon energy for various coverages of Pd on Al.

side of peak (c). Between 2 and 4 ML coverage, the overall *d* band broadens and its centroid moves from 4.0 to 2.0 eV binding energy. For higher Pd coverages, peak (c) evolves into peak (e) and (d) seen for a thick Pd film as shown in the top curve. The spectra of Pd on a polycrystalline Al film are very similar to those found for Pd on an Al(111) single crystal[7]. The key feature of a Pd monolayer on Al is the deep-lying Pd 4*d* emission centered at 4 eV below E_F. The work function of this surface is 4.4 eV [Fig. 25(a)], so this *d* state is 8.4 eV below the vacuum level, very close to the 8.33 eV ionization potential of a Pd atom. The deep-lying Pd *d* state could thereby be explained by assuming atomiclike Pd within the monolayer and indeed this is the basis for the assignment by previous authors[7].

To further test this idea, EDC's for Al films on a Pd substrate were also taken and they were presented in Fig. 24. Since this experiment is meant to demonstrate the movement of the Pd *d* band as Al is deposited on the Pd substrate, only relative Al coverages are given by Al evaporation times. At a relatively small Al coverage (20 sec), the modified Pd states resemble those seen for 2 ML of Pd on Al in Fig. 23 and those for a 7-min Pd evaporation time on Al(111)[7]. At 90-sec Al coverage, this band is centered at 5.0 eV below E_F with a half width of 1.6 eV. For higher Al coverages, the Al *sp* band marked (b) starts to build up at E_F, and the *d* band remains at 5.0 eV binding energy with its intensity reduced. It is difficult to understand this similar deep-lying Pd 4*d* state observed for thick Al on Pd on the basis of atomic level model.

Figures 25(a) and 25(b) show plots of work function versus coverage for Pd on Al and Al on Pd, respectively. For Pd on Al, the work function is initially at 4.27 eV which agrees with the literature value for polycrystalline Al. It then increases slowly to 4.38 eV at 1-ML Pd coverage followed by a faster linear rise from 1- to 4-ML Pd coverage. The electron affinity and ionization potential of Pd are 0.56 and 8.34 eV respectively. J for Pd/Al is then 0.18 eV and thus the initial work function increase is consistent with the J criterion. For Al on Pd, the work function is initially at 5.1 eV which

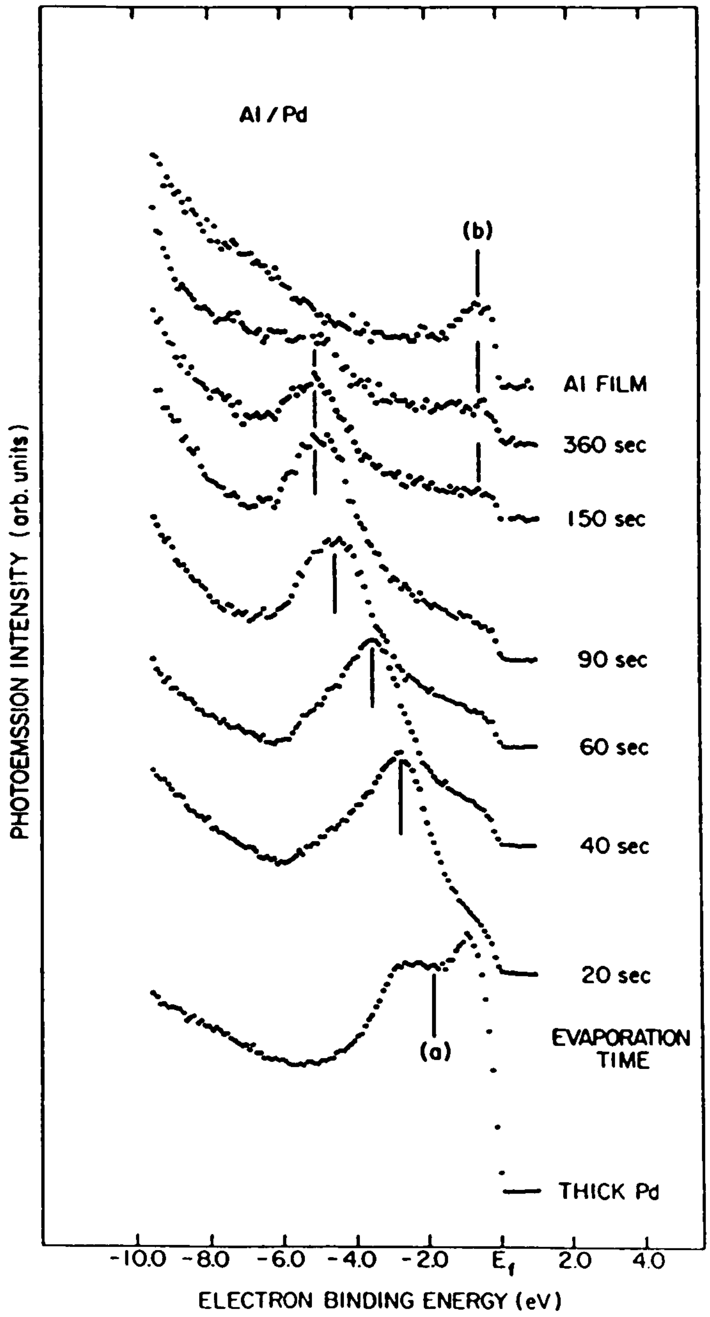

Figure 24. Photoemission spectra obtained with 21.2 eV photon energy for various coverages of Al on Pd.

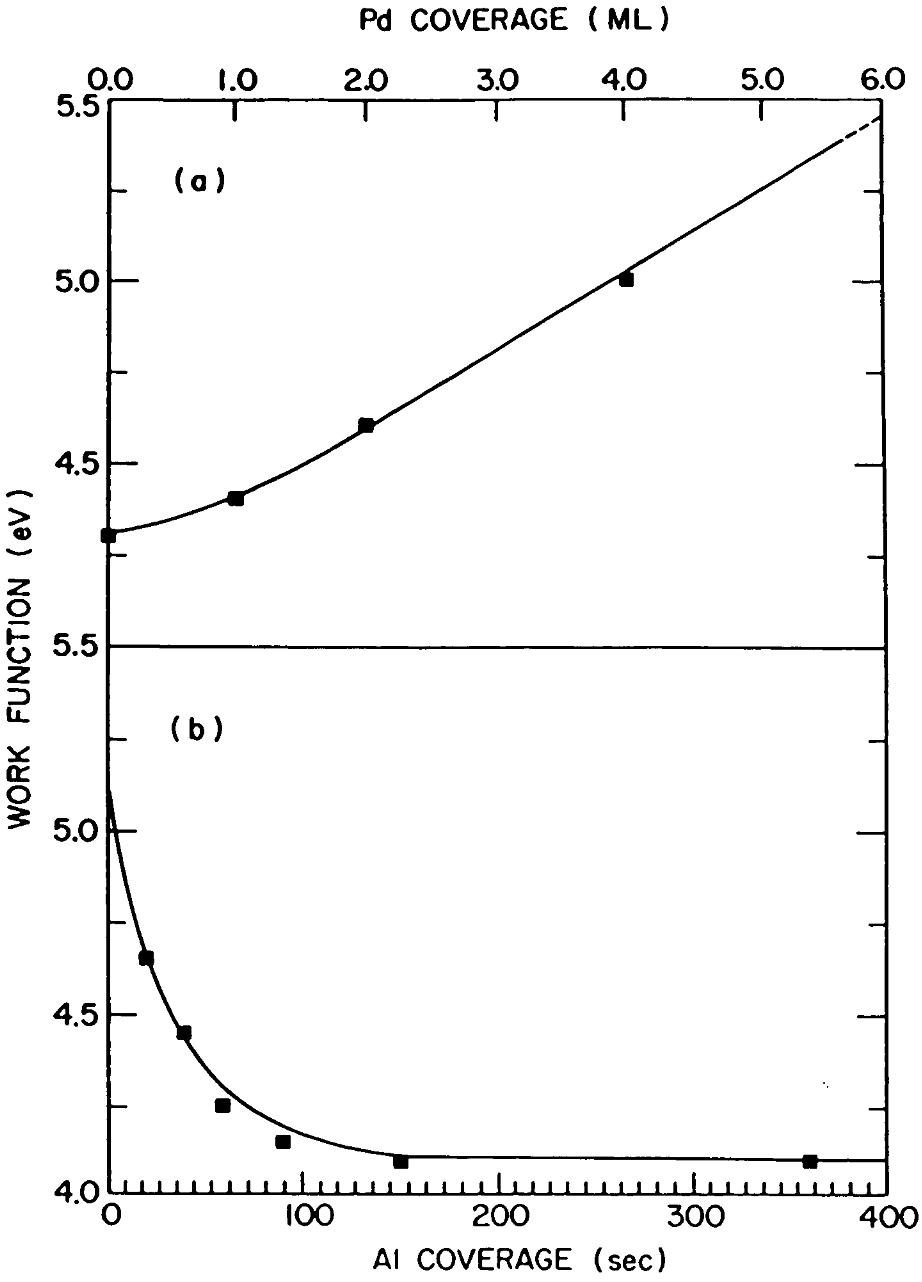

Figure 25. The work function of (a) Pd deposited on Al, (b) Al deposited on Pd as a function of coverage.

is the value expected for polycrystalline Pd. It then decreases rapidly with evaporation time and converges to 4.1 eV as the evaporation time exceeds 90 sec. The variation of work function and the modification of the valence band occur over the same range of Al coverages. The electron affinity and ionization potential of Al are 0.44 and 5.99 eV respectively. J for Al/Pd is then -1.89 eV and thus the initial fast work function decrease is also consistent with the J criterion.

4.2 LEIS studies of Pd/Al

Photoemission results show the existence of a strong interaction between Pd and Al but cannot establish the details of the overlayer growth. Both Auger and photoemission spectroscopy probe a surface region several layers thick and have difficulty in determining whether a deposited layer is actually the top layer or intermixes with the substrate to form a surface alloy over a more extended region. LEIS can resolve this problem in a direct way when combined with the information obtained from photoemission. Figure 26 shows LEIS data for a series of Pd coverages on Al. Using Eq. (2.18), $\theta=150^{\circ}$, $M_1=4$, $M_2=27$ and 106 for Al and Pd respectively, the normalized ion energy (E/E_o) due to the scattering by Al and Pd are found to be 0.576 and 0.869 respectively, which agree well with the low- and high-energy peaks. The Al peak shape is simply Gaussian-like and the approximately 30-eV width is mainly due to the energy spread of the incident ion beam. The Pd peak consists of three components which may be related to the details of the scattering process. The important feature is the observation of a measurable Al signal even at 8-ML Pd coverage. The normalized Pd and Al intensities are plotted as a function of Pd coverage in Fig. 27. Several growth regimes can be seen in this plot and the most noticeable one is from 1 to 3 ML where both Al and Pd signals change slowly.

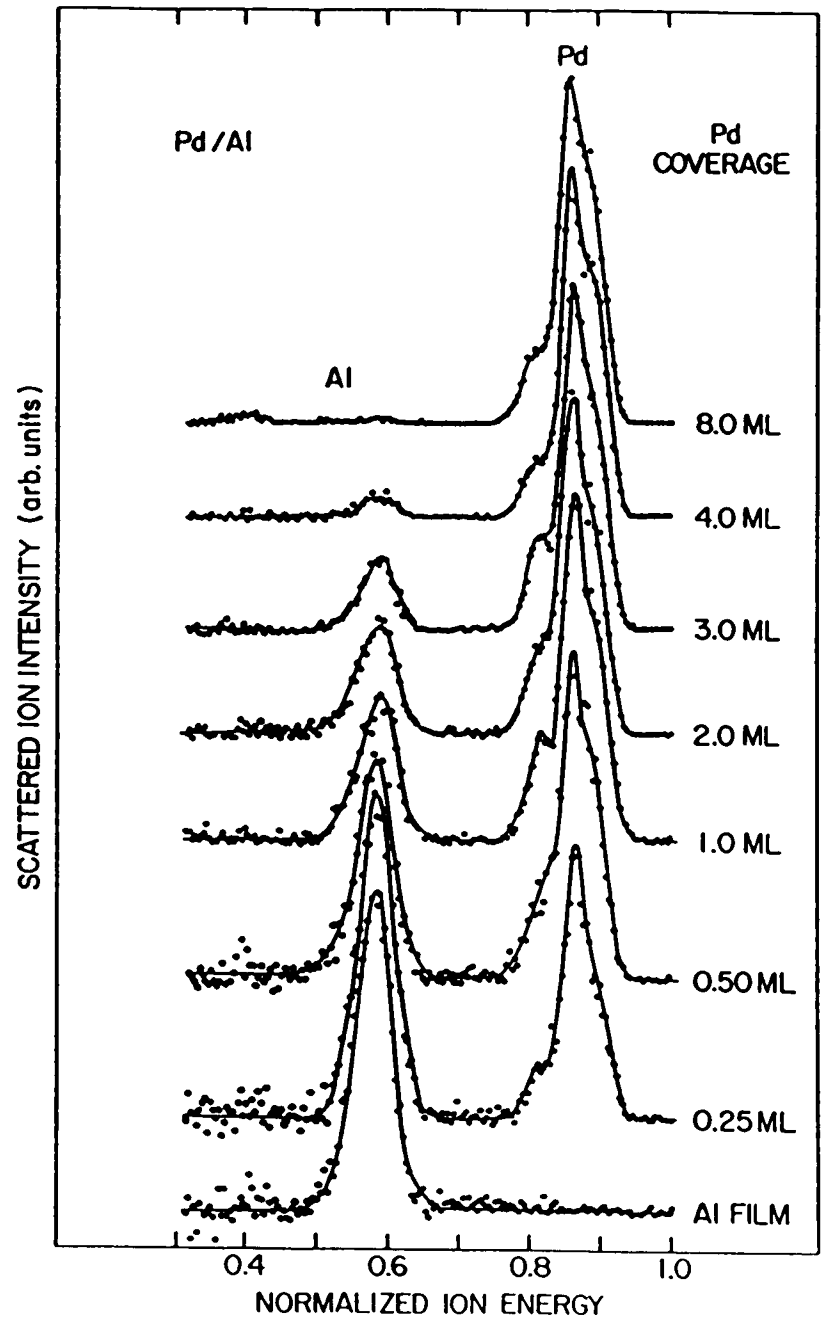

Figure 26. LEIS spectra for various coverages of Pd on Al.

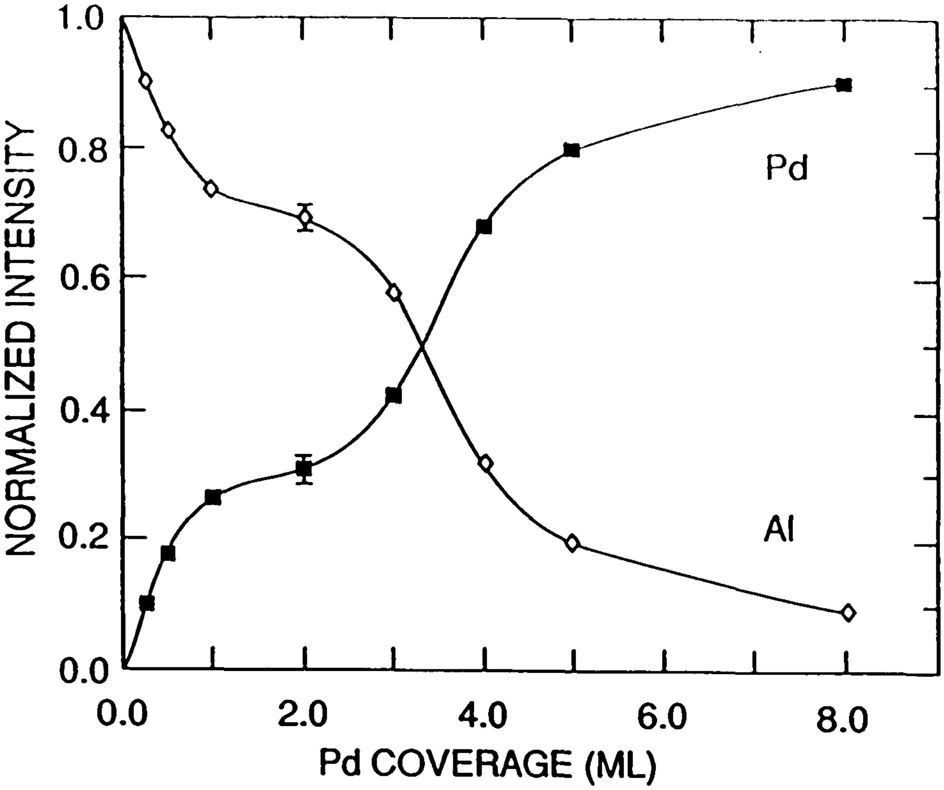

Figure 27. Normalized LEIS intensity of Pd and Al vs Pd coverage on Al.

The LEIS spectra in Fig. 26 show that significant amounts of Al persist in the top layer even after several Pd monolayers have been deposited on Al. The plots in Fig. 27 show that there is a big drop in the Al signal from 3- to 4-ML Pd coverage on Al. This is consistent with the corresponding photoemission result which indicates that bulklike Pd 4*d* states start to build up at E_F. These observations suggest that Pd either starts clustering before covering the substrate or intermixes with it forming a surface alloy about 5-ML thick. The photoemission result, however, rules out the possibility of simple Pd clustering because Pd bulk features should then build up at E_F well before 4-ML Pd coverage is achieved. It has already been shown that Pd bulk features with states near E_F can be seen when the cluster size approaches about 15 atoms[46], and much larger clusters would be expected at 4-ML Pd coverage. Thus, alloy formation at the Pd/Al interface is concluded and this finding was confirmed later by a high-resolution Rutherford backscattering spectroscopy study of the Pd/Al(111) and Pd/Al(110) interfaces.[47]

The alloying hypothesis is further supported by XPS studies on bulk alloys by Fuggle *et al.*[48] Their XPS spectra of several alloys are shown in Fig. 28. $PdAl_3$ has a filled *d* band centered at 4.8 eV below E_F. The *d* band for PdAl consists of two peaks at 4.6 and 3.6 eV below E_F and the centroid of the overall band is 4.1 eV below E_F. Peak (a) and peak (b), seen for 1-ML Pd coverage on polycrystalline Al and on Al(111), are separated by about 1 eV. This separation, which is too large to be explained by the spin-orbit splitting of 0.4 eV for *d* states in the Pd atomic $4d^{10}5s^0$ configuration, is now easily attributed to the compounds $PdAl_3$ and PdAl formed when a monolayer of Pd is deposited on Al. As more Pd is deposited, more Pd-rich compounds, such as PdAl, are formed relative to $PdAl_3$ and thus peak (b) grows faster than peak (a).

Although our experiments are on a polycrystalline substrate, the similarity of our photoemission results of Pd on Al to those found for Pd on Al(111),[7] and the fact that the complete development of the metallic Pd valence band on Al(111) and complete covering of the Al substrate by Pd in our LEIS study occur at the same high-Pd coverage (more than 8 ML), suggest that alloying or a strong interaction also occurs between Pd and the Al(111) substrate. This is also supported by the following argument, which shows that the deep-lying *d* states found for 1-ML Pd coverage on Al(111) cannot simply be assigned to the atomic $4d^{10}5s^0$ configuration for Pd. Self-consistent band-structure calculations on a free Pd(100) monolayer[49] show that the *d* band is no longer filled as in the atomic configuration $4d^{10}5s^0$. This means that the Pd-Pd interaction is already strong enough to start mixing $4d$ and $5s$ states which leads to $4d$ to $5s$ charge redistribution. The in-plane densities of atoms for Al(111) and Pd(111) are 0.138 and 0.154 (atoms/Å^2), respectively, both larger than that for Pd(100) which is 0.131 (atoms/Å^2). We therefore expect a stronger Pd-Pd interaction for either a commensurate or incommensurate Pd monolayer on Al(111) than a free standing Pd(100) monolayer. This should result in

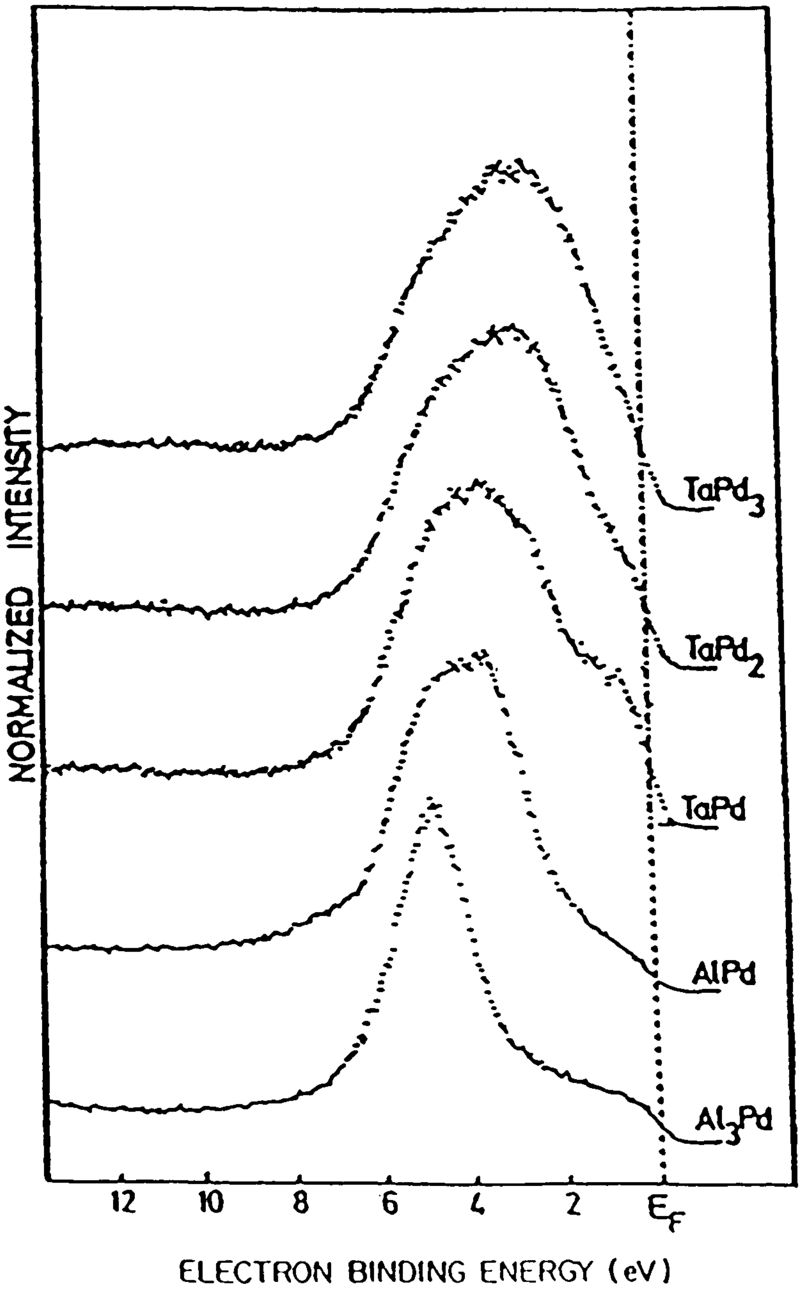

Figure 28. XPS (hv=1486 eV) spectra of bulk Pd-Al and Pd-Ta alloys.

more overlap between 4*d* and 5*s* states and lead to more 4*d* to 5*s* charge redistribution. Hence the *d* band of a Pd monolayer on Al(111) should not be filled, and thus a deep-lying *d* state is impossible without taking the interaction with the Al substrate into account.

In an attempt to better understand the relative strength of the Pd-Pd interaction and the origin of the deep-lying Pd 4*d* states, we calculate the interatomic matrix elements between a Pd atom and its nearest-neighbor Pd atoms. Since we are mainly concerned with the Pd 4*d* to 5*s* redistribution, we will only calculate the V_{ss},V_{sd}, and V_{dd} matrix elements. They are given by[50]

$$\begin{aligned} V_{ss} &= C_{ss}\, N/d^2\,, \\ V_{sd} &= C_{sd}\, N/d^{7/2}, \\ V_{dd} &= C_{dd}\, N/d^5, \end{aligned} \tag{4.1}$$

Where N is the number of Pd nearest neighbors and d is the nearest-neighbor distance. C_{ss}, C_{sd}, and C_{dd} are constants. Using (4.1) these matrix elements are calculated for various Pd arrangements and normalized to those for a Pd(100) monolayer. The results are summarized in Table III.

It is clear from this table that both for the Pd(111) monolayer and for a commensurate Pd monolayer on Al(111), the *ss*, *sd*, and *dd* interatomic matrix elements are all larger than those for a Pd(100) monolayer, and the Pd-Pd interaction is indeed stronger in an either commensurate or incommensurate Pd monolayer on Al(111) than in a Pd (100) monolayer. From Table III we also see that the Pd-Pd interaction in PdAl is about the same as in a Pd(100) monolayer. This means that in PdAl the *d* band should not be filled if we only consider the Pd-Pd interaction. The fact that the *d* band is filled in PdAl suggests that the origin of the deep-lying Pd 4*d* states is the Pd-Al interaction. This is confirmed by band-structure calculations which show that the Pd 4*d* states are filled in $PdAl_3$ and PdAl by *s* electrons from the electropositive Al.[48] This band filling is mainly due to the hybridization of the Pd *d* and Al *s* states as the calculations indicate that there is always Pd *d* character in the bands above E_F. This differs from the situation for Pd metal where all the unoccupied *d* states are near E_F; the unoccupied *d* states in $PdAl_3$ and PdAl alloys are more spread out which makes it difficult to detect them using inverse photoemission spectroscopy (IPS). This explains the flat IPS spectrum seen at 1ML Pd coverage on Al(111)[53] which was claimed as a proof for atomiclike Pd.

Table III. Pd-Pd interatomic matrix elements for various Pd arrangements normalized to those for a Pd(100) monolayer.

Pd arrangement	N	d (Å)	V_{ss}	V_{sd}	V_{dd}	Ref. for d and N
Pd(100) monolayer	4	2.75	1.00	1.00	1.00	51
Pd(111) monolayer	6	2.75	1.50	1.50	1.50	51
Al(111)* monolayer	6	2.86	1.39	1.31	1.23	51
PdAl compound	6	3.00	1.26	1.11	0.97	52

*Commensurate Pd monolayer on Al(111)

4.3 Electronic and CO adsorption properties of Nb/Pd(111)

Figure 29(a) shows energy distribution curves (EDC's) taken with He 21.2 eV excitation energy for Nb overlayers on Pd(111). The Pd 4*d* states move to higher binding energy with increasing Nb coverage. At 1 ML, the spectrum resembles that of a Pd monolayer on Nb (110)[25] and is characterized by strong Pd 4*d* emission 1-4 eV below E_F. At 2 ML, the Pd derived states are at -2.7 eV binding energy and are reduced in intensity compared to monolayer coverage.

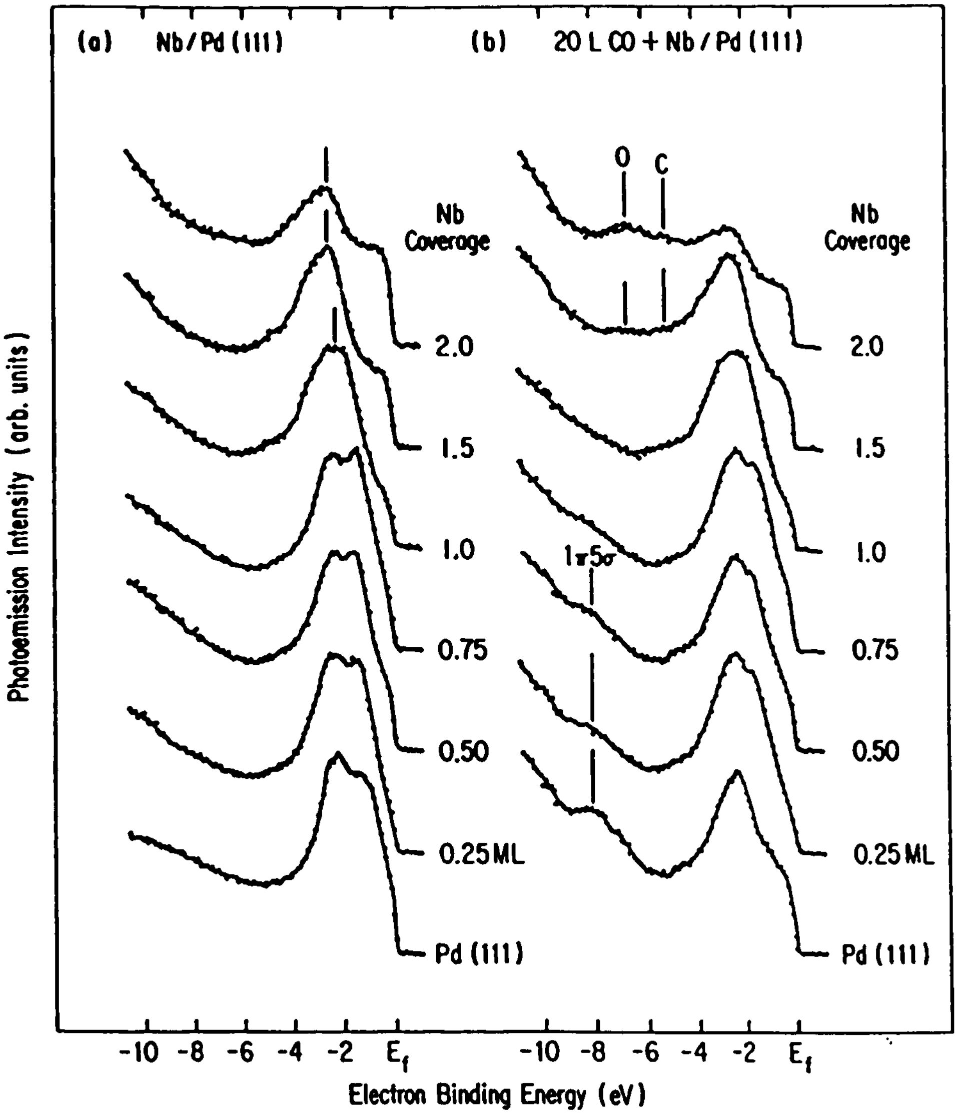

Figure 29. Photoemission spectra (hv=21.2 eV) for various coverages of Nb on Pd(111), (a) before (b) after exposure to 20 L CO.

In order to show the evolution of the density of states at E_F, two typical difference curves derived from the spectra in Fig. 29(a) are plotted in Fig. 30. Figure 30(a) is the difference curve between 1-ML Nb coverage and Pd(111) substrate. Figure 30(b) is the difference curve between 2-ML Nb coverage and 1-ML Nb coverage. Clearly the density of states at E_F at 1-ML Nb coverage is lower than the density of states at E_F for both the clean Pd (111) substrate and for 2-ML Nb coverage. Also the Nb 4*d* states start to build up at E_F above 1-ML Nb coverage.

Figure 29(b) shows the effects of 20 L CO exposure on these Nb films. Molecular CO chemisorption, as indicated by the CO1π-5σ peak at -8 eV, is seen for submonolayer Nb coverages. Dissociative CO chemisorption, as indicated by the O 2*p* and C 2*p* peaks at -6.3 and -4.8 eV is seen for greater than a monolayer Nb coverage. Features associated with adsorbed CO are very weak at monolayer Nb coverage. The reduced CO adsorption at room temperature was also found for a Pd monolayer on the (110) surfaces of W[54], Nb, and Ta[25]. Previous UPS work[25] involving CO adsorption on Nb(110) supported Pd monolayers suggests that the CO-Pd bond is weaker because the states ordinarily involved in the chemisorption bond as acceptor or donor states are not available for bond formation. The modification of these chemically active Pd states occurs because the Pd 4*d* band is filled due to the hybridization of Pd and Nb states at the interfaces. Therefore the heat of adsorption is smaller than that for unmodified Pd, and the surface behaves like a noble metal such as copper which has low sticking coefficient for CO at room temperature. The reduced CO adsorption at a monolayer of Nb on Pd is interesting because Nb is an early transition metal and its *d* band can hardly be filled at one monolayer. Hence the question of whether the deposited Nb monolayer really covers the Pd substrate is critical. LEIS was used to answer this question conclusively because it has the advantage of probing only the top atomic layer and therefore should be decisive in addressing this issue. The large mass difference between Pd and Ta allows us to resolve them in the simple LEIS setup used in this thesis. In view of the similarity in the physical and chemical properties of Nb and Ta, and the similarity in the photoemission results of Pd/Nb(110) and Pd/Ta(110), we believe that the results for Pd-Ta system can be extrapolated to the Pd-Nb system.

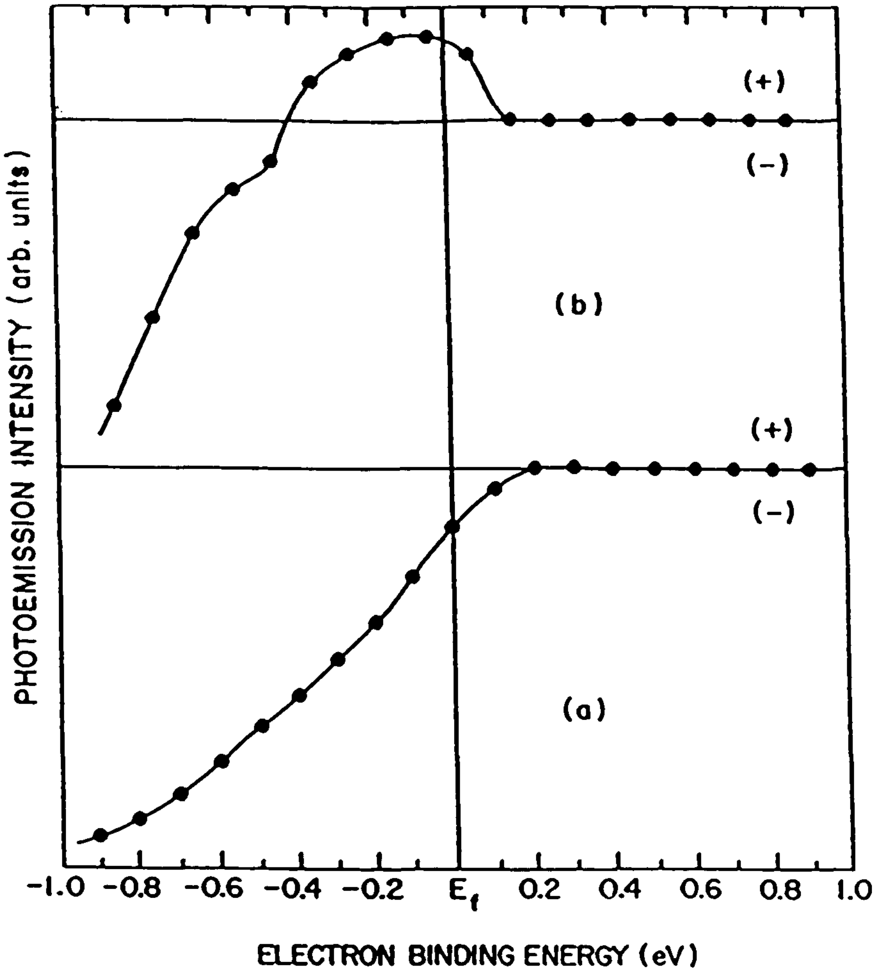

Figure 30. Photoemission difference curves (a) between 1-ML Nb/Pd(111) and Pd(111) substrate, (b) between 2 ML and 1 ML Nb on Pd(111).

4.4 LEIS Studies of Pd/Ta(110) and Ta/Pd(111)

Figure 31(a) shows the LEIS spectra for Pd/Ta(110) as a contrast. Simple calculations using Eq. (2.18) ($\theta=150°$, $M_1=20$ for Ne^+, $M_2=106$ and 181 for Pd and Ta respectively) indicate that the low- and high-energy peaks at 0.52 and 0.68 are due to scattering from Pd and Ta respectively. The Ta signal is completely suppressed at 1 ML, implying that the Ta substrate is covered. Heating the Ta surface covered by more than a monolayer of Pd to temperatures up to the desorption temperature of ~1000 °C did not change the LEIS spectra, indicating the stability of Pd monolayer. These results are consistent with FM growth at room temperature and SK growth at an elevated temperature of Pd on Ta(110) as suggested by Koel *et al.*'s AES study[55]. Figure 31(b) shows the LEIS spectra for Ta on Pd(111). The Pd signal is stronger than the Ta signal at 1 ML and is observable even at 8 ML, implying that Ta is not covering the Pd substrate and therefore Ta either clusters on Pd or intermixes with the Pd substrate.

Simple clustering cannot explain the Pd 4*d* states moving significantly below E_F with increasing Nb coverage and the reduced CO chemisorption at monolayer Nb coverage on Pd(111). On the other hand, the valence electronic structure of Pd-Ta (same as Pd-Nb) compounds shown in Fig. 28 have a similar trend as the spectra in Fig. 29(a). The Pd 4*d* band moves to higher binding energies as the compound becomes more Ta rich and the spectrum for $TaPd_2$ or $NbPd_2$ resembles that for a monolayer Nb or Ta coverage on Pd(111). Coincidentally LEIS also shows a composition of ~1 Ta:2 Pd for a monolayer Ta coverage on Pd(111). These observations suggest that deposited Ta or Nb intermixes with the Pd substrate forming a surface alloy which becomes more Ta or Nb rich as more Ta or Nb is deposited. LEED examination shows that the hexagonal Pd(111) pattern becomes weaker with increasing Nb coverage, and it disappears by 2 ML, indicating that the surface alloys are disordered. At 1-ML coverage, the surface appears to be mostly $TaPd_2$ or $NbPd_2$ which has a noble-metal-like electronic structure and therefore has a small sticking coefficient for CO at room temperature. It should be noted that Nb or Ta deposition can be controlled to tailor Pd(111) to molecularly or dissociatively adsorb CO and further TPD experiments should be conducted to investigate CO-metal bond energies in these systems. It is interesting that the Nb or Pd atoms on the alloy surface seem to have lost their chemical identity because both Nb and Pd surfaces readily adsorb CO. We therefore conclude that it is the overall surface electronic structure, instead of a mere superposition of individual elements, that dominates the chemisorptive properties.

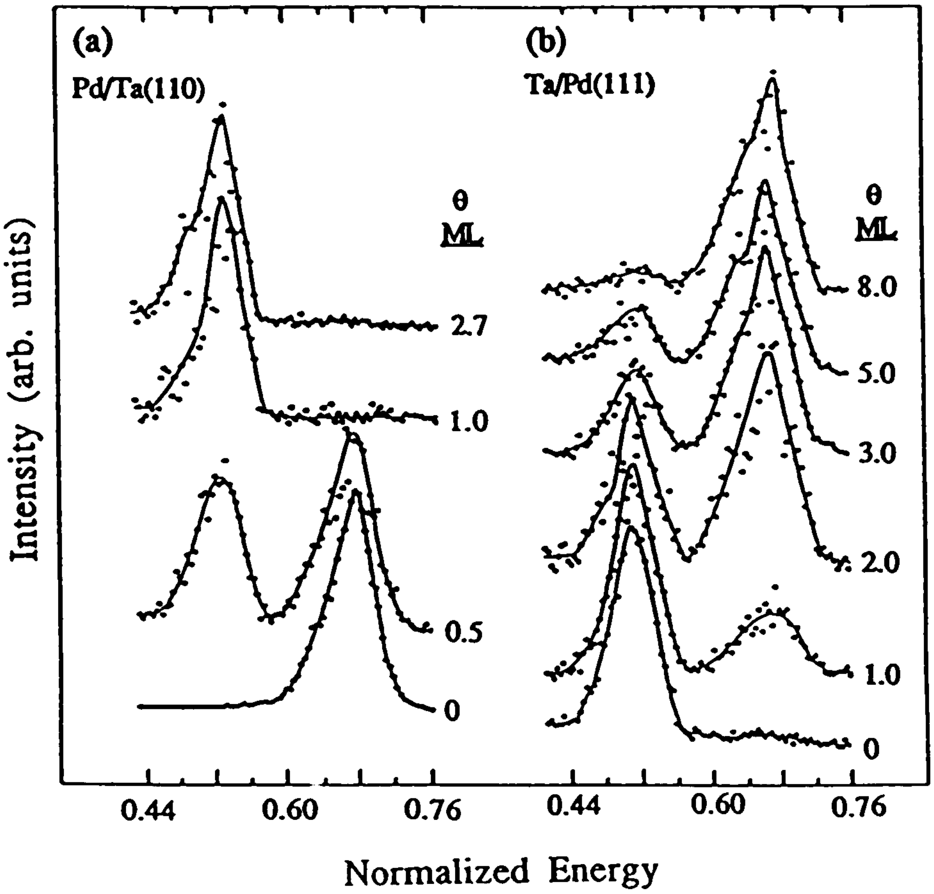

Figure 31. LEIS spectra for various coverages of (a) Pd on Ta(110), (b) Ta on Pd(111).

Next we turn to the interpretation of the intermixing between deposited Nb or Ta and the Pd(111) substrate. The energetics of the Pd-Nb multilayer systems have been investigated by Watson *et al.*[3] using first-principle total energy calculations outlined in section 3.1. An interface energy of ~-3/8 eV per Nb-Pd pair and a distortion energy of ~1/4 eV have been found in a lattice constrained to be commensurate with Nb(110). Thus, according to Eq. 3.6, at 1.5 ML coverage of Pd on Nb(110), these bulk terms indicate a net zero binding, a circumstance encouraging the Pd overlayer to reorganize into an energetically more favorable lattice. This agrees well with the experimental observation that a commensurate-incommensurate transition occurs near 1.5 ML Pd coverage[9]. Using the atomic densities appropriate to the close-packed planes (Eq. 3.2), the surface energies can be converted from J/m^2 to the more convenient unit of eV/atom, and their room-temperature value are found to be 0.84 and 1.44 eV/atom for Pd(111) and Nb(110) respectively. Thus, according to Bauer's criteria, the surface energy contribution favors the FM growth of Pd/Nb(110) which is indeed observed[55] to continue after the structural transition near 1.5 ML until several layers. On the other hand, for Nb/Pd(111), the surface energy contribution will be a significant energy cost (0.6 eV/atom) which is larger than the sum of the interface and distortion energy terms and is therefore against FM growth. The question now is whether VW growth or alloy formation is energetically more favorable. The heat of formation for bulk $NbPd_2$ has been calculated[3] to be -0.41 eV/atom which is comparable to the interface energy. Clearly both the interfacial bonding energy and the heat of formation terms are larger than the distortion energy cost term, so clustering is not favored at the Pd-Nb interface. On the other hand, by alloy formation, the surface energy can be reduced to that of the Nb-Pd alloy while gaining about the same amount of Nb-Pd bonding energy by the heat of compound formation. The intermixing behavior between the deposited Nb and Pd(111) is thus energetically justified. Since the surface energy of Al (0.48 eV/atom) is less than Pd by 0.36 eV/atom and the heat of formation for PdAl compound is huge (-0.96 eV/atom), the intermixing behavior between deposited Pd and an Al substrate can also be understood.

Chapter 5. Growth and Electronic Properties of Rh Overlayers on Ta(110) and Mo(110)

Rhodium is an important industrial catalyst and is also used in automotive catalytic converters to reduce nitrogen oxides[56]. Although surface techniques are used in a number of ways to examine single-crystal Rh surfaces and their interaction with small molecules and hydrocarbons[57], little is known about Rh thin films. Recently Koel *et al.*[55] reported TPD measurements showing a 19.6 kcal/mol reduction in the activation energy for CO desorption from Pd monolayer on Ta(110) compared to Pd(111). This behavior along with the interesting hydrogen uptake[8] and catalytic properties (section 2.23) of Pd/Ta(110) are attributed to the novel surface electronic properties, especially the changes in the density of states near the Fermi level. The Rh *d* band has one less electron than Pd, a comparative study of Rh films will allow the examination of the trends in the electronic properties and the associated effect on adsorption.

So far the structural phase diagram (Fig. 18) discussed in section 3.2 can predict epitaxial orientations with a high degree of reliability in the region near the optimal atomic diameter ratio corresponding to the natural matching of atomic rows, while great uncertainties exist for in-between systems where the energetics do not strongly favor one over the other. Rh/Ta(110) and Rh/Mo(110) represent typical cases near NW(-x) region and in-between NW(-x) and KS regions, and it will be of value to compare their growth with theoretical predictions. By changing the substrate from Ta to Mo, the lattice-mismatch is also reduced so that it is comparable to that of Pd/Ta(110) (Fig. 15) and its influence on the growth can then be investigated. Although the possibility of an orientation change during growth has been raised by theoretical modeling,[2,32] to the best of my knowledge, no clear experimental evidence exists in literature. In this chapter, the results on the growth and electronic properties of Rh films on Ta(110) and Mo(110) will be presented. An orientation transition from KS to NW orientation during the growth of a Rh(111) monolayer on Mo(110) is observed for the first time and it will be discussed in light of current views of the structure of fcc(111)/bcc(110) interfaces.

5.1 Characterization of Rh films on Ta(110)

The dependence of the Rh 302 eV and Ta 179 eV Auger peaks as a function of Rh evaporation time is shown in Fig. 32. The growth of the Rh peak and the attenuation of Ta peak is linear up to 2 min. At about 2 min, the slope of each curve changes and the curves are nonlinear for longer evaporations. Figure 32 indicates that a break occurs in the gradient at 2 min deposition time and this is usually taken as indication that a monolayer has formed. The observation of no further breaks suggests the layer-plus-islanding, i.e., Stranski-Krastanov (SK) growth mechanism. The curve in Fig. 32 was obtained by monitoring the changes of Auger peak height with time during deposition while the analyzer was set at the electron kinetic energy of 179 (302) eV corresponding to the position of Ta (Rh) Auger peak. This method has the least change of experimental variable and the advantage of getting the uptake curve in one scan. The disadvantage is that any chemical shift of the Auger peak will influence the signal and make it deviate from the peak height. The Auger spectra of different Rh coverages have been taken to check this and no appreciable shift of Auger peaks are found, and thus the reliability of Fig. 32 is assured. However, due to their different elemental sensitivity, the Rh and Ta curves are in different scale and therefore the Auger ratio is not reflected in Fig. 32.

The Auger ratio is an important calibration of coverage because it does not change sensibly with experimental parameters such as primary beam intensity, electron multiplier gain, etc. A series of Auger spectra at different Rh coverages on Ta(110) have been taken and the more conventional uptake curve, obtained by plotting the peak-to-peak amplitudes of Rh and Ta versus deposition time, agrees well with Fig. 32 after normalization. The Auger intensity ratio can be derived in this uptake curve (Fig. 33) and again only one break is seen. The mean free path of Ta Auger electron (179 eV) is about 2 ML and therefore the Ta substrate signal should be attenuated by 40-60% ($e^{-1/2}$) by one monolayer of Rh. The Ta attenuation is very slow in Fig. 32 or 33 and it is only near 30% at the break point.

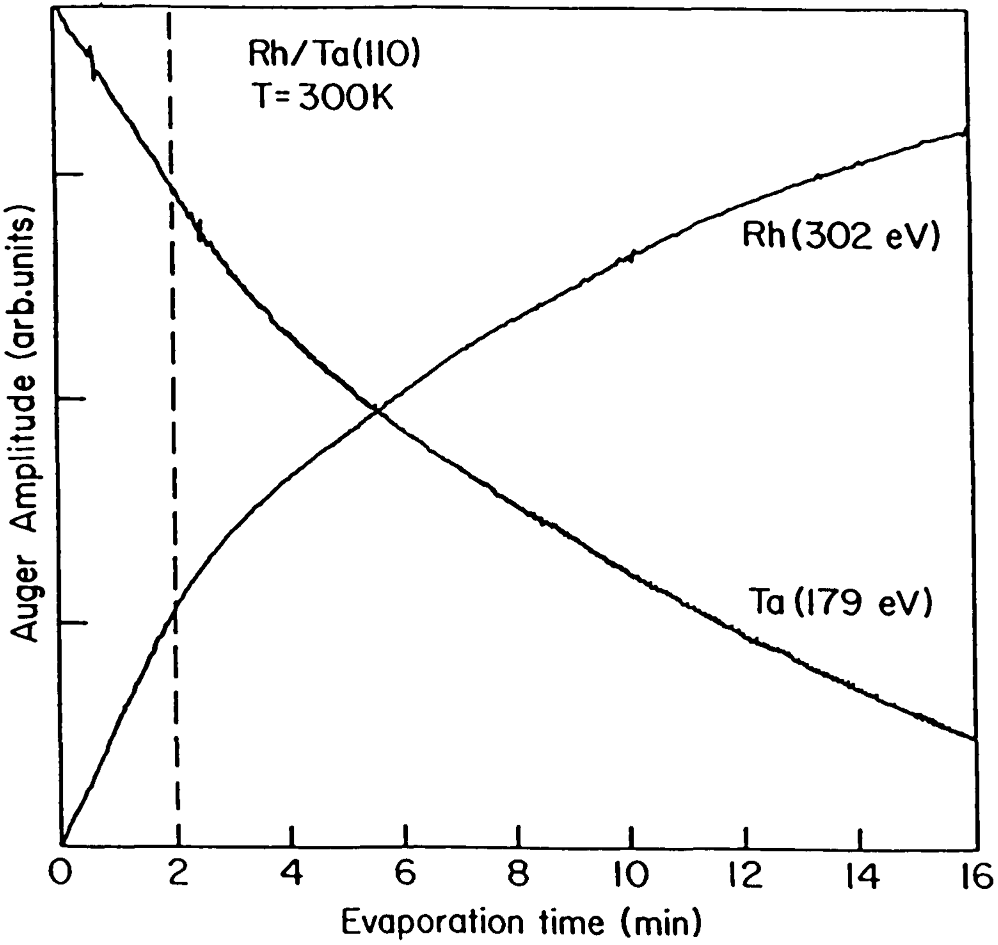

Figure 32. Rh and Ta Auger peak amplitudes as a function of Rh evaporation time. Rh and Ta are in different scale.

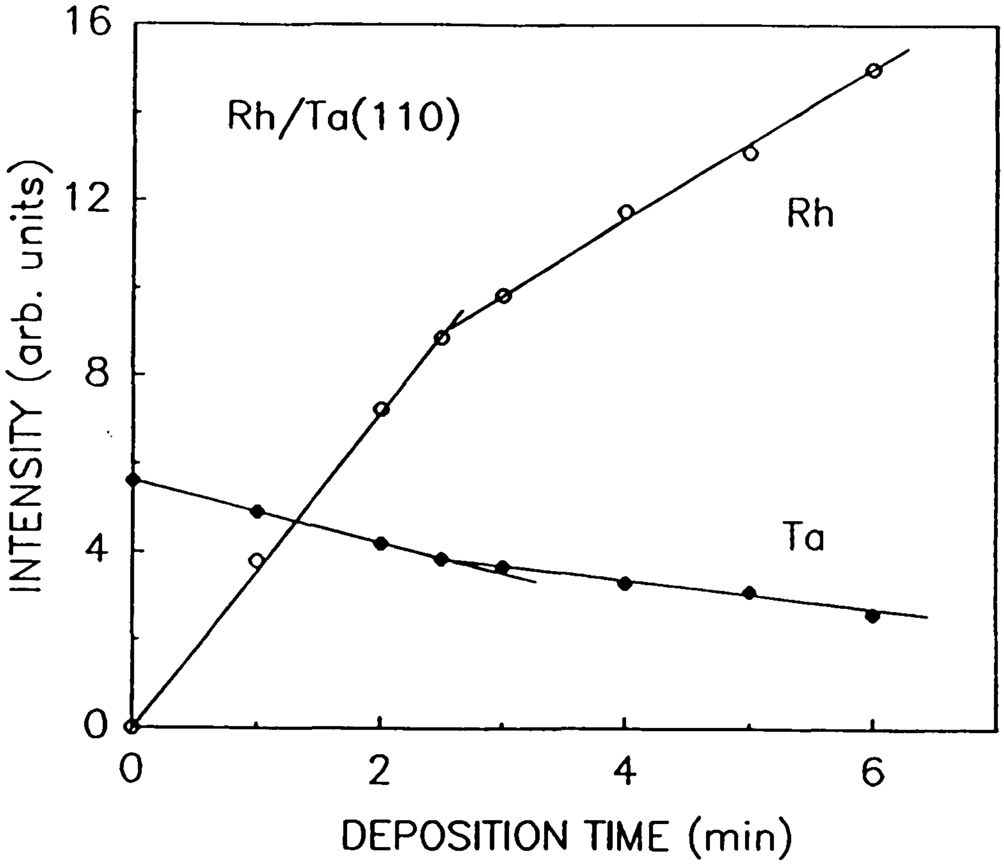

Figure 33. Rh and Ta Auger peak-to-peak amplitudes as a function of Rh deposition time. Rh and Ta are in same scale.

LEIS was done to reexamine the conclusion derived from the AST curve concerning the SK growth mechanism. Figure 34(a) shows a LEIS spectrum obtained for a 2 min Rh deposition corresponding to the AST break point. Here 500 eV He^+ ions are scattered from this surface at two distinct energies and a simple calculation using Eq. (2.18) (θ=150°, M_1=4, M_2=103 and 181 for Rh and Ta respectively) shows that the component at 0.865 is due to Rh and the other component at 0.92 is due to Ta. The failure to completely cover the surface at 2 min evaporation time indicates that Rh clustering begins before the first monolayer is completed. In Fig. 34(b), the normalized intensity of

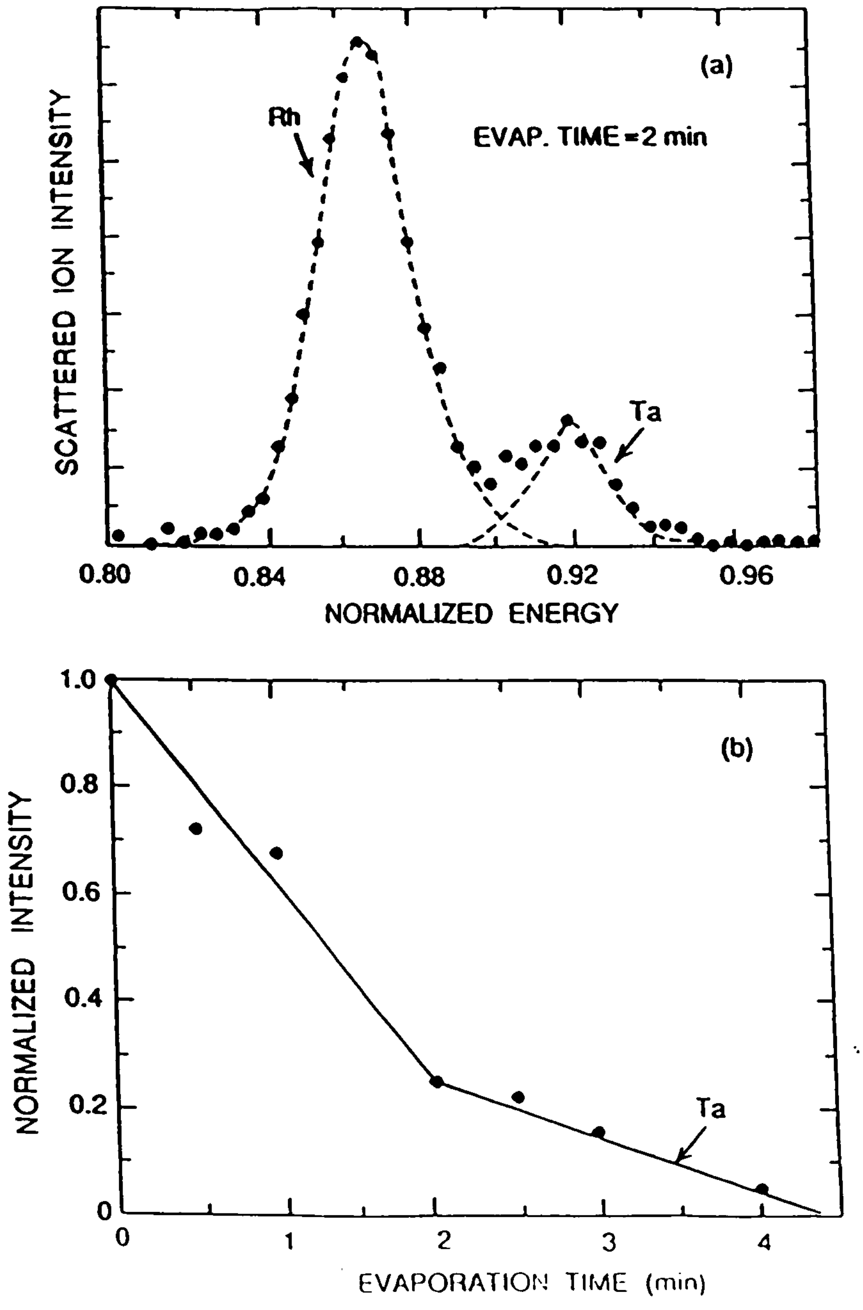

Figure 34. (a) LEIS spectrum for 2 min Rh on Ta(110), (b) Normalized intensity (I/I_o) of the 0.92 Ta LEIS peak as a function of Rh evaporation time.

the Ta peak is plotted as function of evaporation time. Consistent with the AES results, the Ta LEIS signal decreases linearly with Rh evaporation time up to 2 min where the attenuation is 75%. Only the (1X1) LEED pattern [Fig. 35(a)] is seen in this submonolayer range with an increase in background. This suggests that Rh grows pseudomorphically on Ta(110) in a layer-by-layer mode only to 0.75 ML, probably because of the limited mobility of Rh on Ta(110). Above 0.75 ML, the Ta LEIS intensity attenuates with a smaller slope and more than 1.5 ML (4 min) of Rh is needed to completely cover the surface. The (1X1) LEED pattern is almost completely lost in the diffuse background in the coverage range between 0.75 and 1.5 ML. As predicted by the structural phase diagram in Fig. 18 [r=0.939 for Rh(111)/Ta(110)], LEED pattern corresponding to Rh(111) in NW-x orientation [Fig. 35(b)] becomes visible above 1.5 ML but also with a significant background, indicating that clustering and/or disordering plays a major role in the growth of Rh overlayer on Ta(110). We conclude that the growth of Rh films on Ta(110) is an example of an incomplete SK growth mechanism or may be more appropriately described by the Volmer-Weber (3D islanding) growth mechanism.

Heat treatment offers another way of creating new materials besides thin film epitaxy and it can also be used to obtain important information such as the thermal stability of interfaces. Annealing Rh/Ta(110) for 1 min at all coverages above 0.5 ML leads to complete disorder at temperatures below 500 °C. At slightly higher temperatures between 500 and 800 °C, the surface reorganizes and displays a (2X1) structure [Fig. 35(c)]. Near 800 °C, the (2X1) spots broaden (elongate) along Ta $[\bar{1}10]$ direction and finally a more stable (3X1) structure [Fig. 35(d)] results at higher temperatures with an almost constant Rh/Ta Auger ratio of 1.2 before Rh completely disappears at T>1200 °C. Sometimes the LEED pattern changes from complete disorder upon low temperature annealing directly to the (3X1) structure with increasing temperature without passing through the intermediate (2X1) structure and this is more likely for the annealing of very thin (<1/2 ML) and thick (>4ML) Rh films on Ta(110).

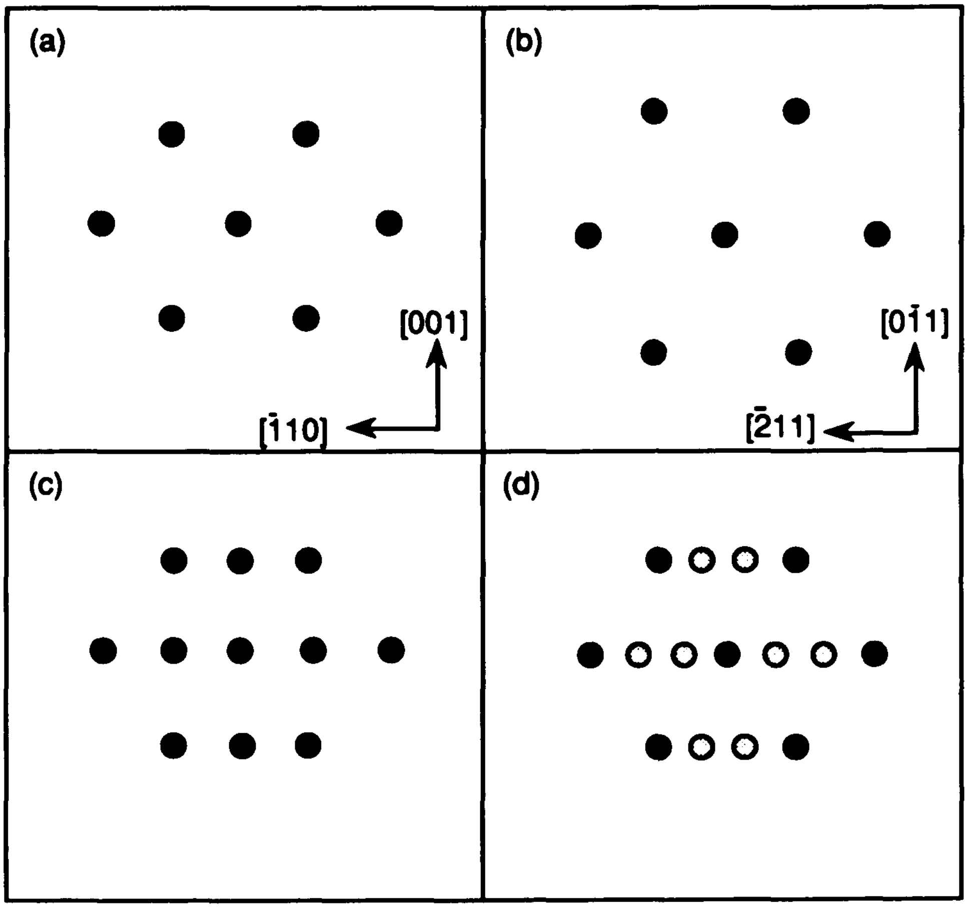

Figure 35. Schematics of LEED patterns observed for Rh/Ta(110): (a) submonolayer coverage, (b) multilayer coverage, (c) and (d) annealing of (b) to 700 and 1000 °C respectively.

Figure 36 shows the variation in work function (ϕ) with Rh coverage. For Rh/Ta(110), I=7.46 eV, A=1.14 eV, ϕ=4.8 eV, and J=-0.5 eV<0. Thus the initial decrease in ϕ is just as predicted by the J criterion. ϕ does not converge to the Rh(111) single crystal value of 5.4 eV even at coverages beyond 4 ML. This is consistent with the fact that the growth of Rh is not the FM mode and the surface is significantly roughened and disordered.

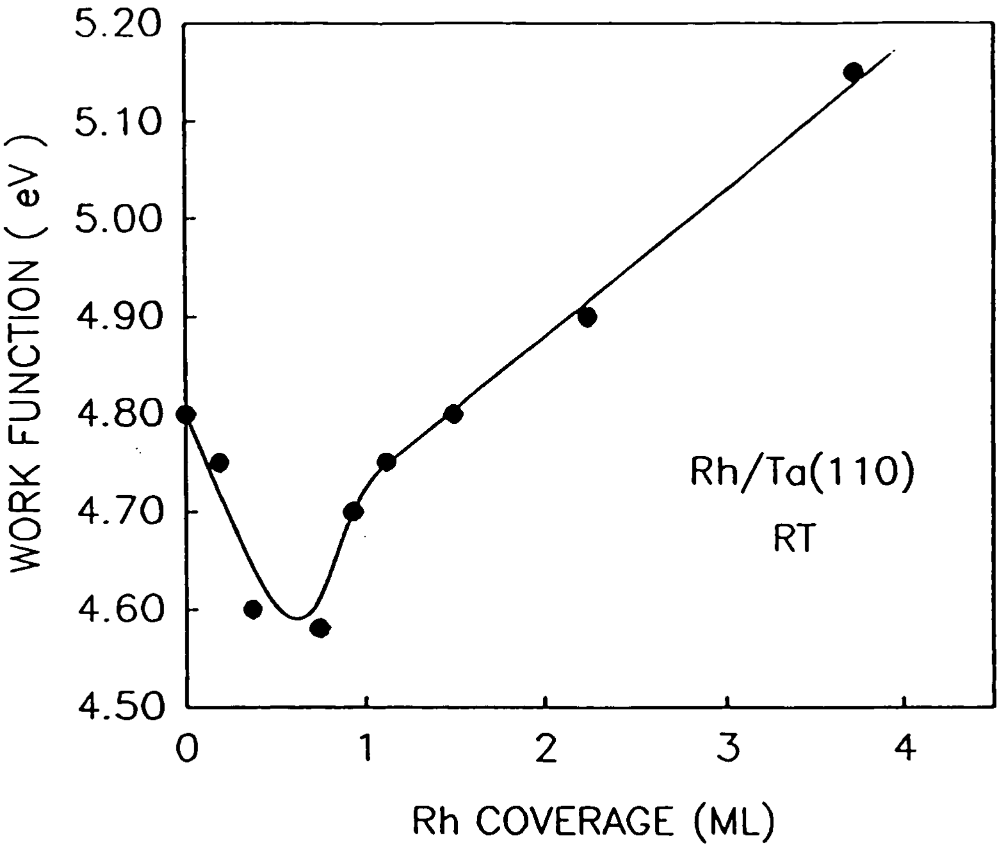

Figure 36. Variation of work function vs Rh coverage on Ta(110).

The evolution of electronic structure is shown in Fig. 37 by the photoemission spectra [He (21.2 eV)] for a range of Rh coverages on Ta(110). Interpretation of the photoemission spectra is more difficult for Rh/Ta(110) than for Pd/Ta (110) because the islanding produces a wider range of Rh adatom environments. Rh adsorption produces a single peak near -2.5 eV binding energy at low coverages when the islands are small or the Rh sits on the surface as adatoms. A second peak near -1.5 eV becomes visible between 0.38 and 0.47 ML Rh coverage. New states near -2 eV become the strongest feature at monolayer Rh coverage and the density of states just below E_F increases significantly upon further deposition of Rh.

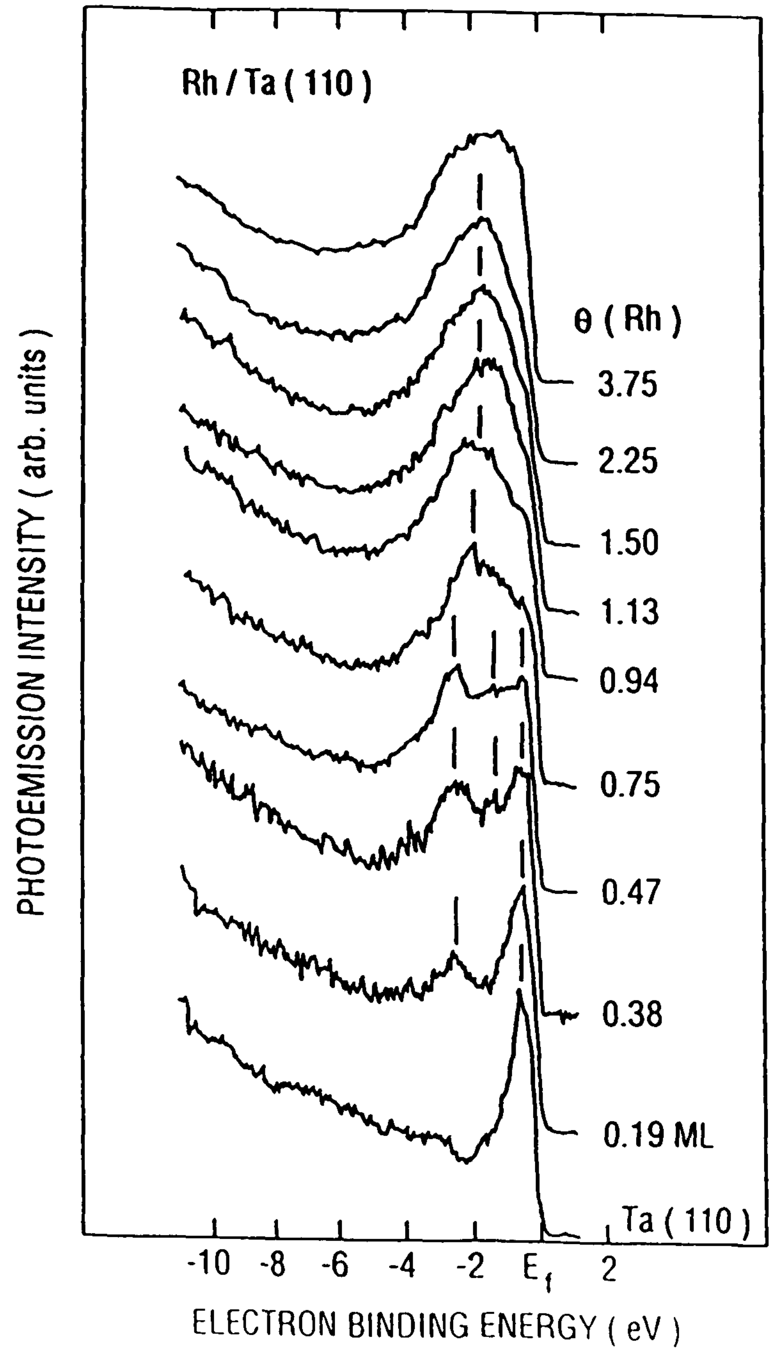

Figure 37. Photoemission spectra (hν=21.2 eV) for various Rh coverages on Ta(110).

Synchrotron radiation photoemission allows detailed examination of the cross-sectional dependence which can be used to identify the relative contributions of the component metals to valence band features. Spectra for a thick (θ~10 ML) Rh film are shown in Fig. 38(a). The Rh 4*d* valence-band emission exhibits a resonant minimum (marked by the arrow) as the photon energy reaches the 4*p* ($4p^64d^n$ + hv $\rightarrow 4p^54d^{n+1}$) threshold ~47 eV. This Fano-like resonance has been observed previously on the Rh(111) single-crystal surface[58]. On the other hand, the spectra for clean Ta(110) indicate an enhancement of its valence band features at -0.8 and -3.2 eV binding energies near this photon energy [Fig. 38(b)].

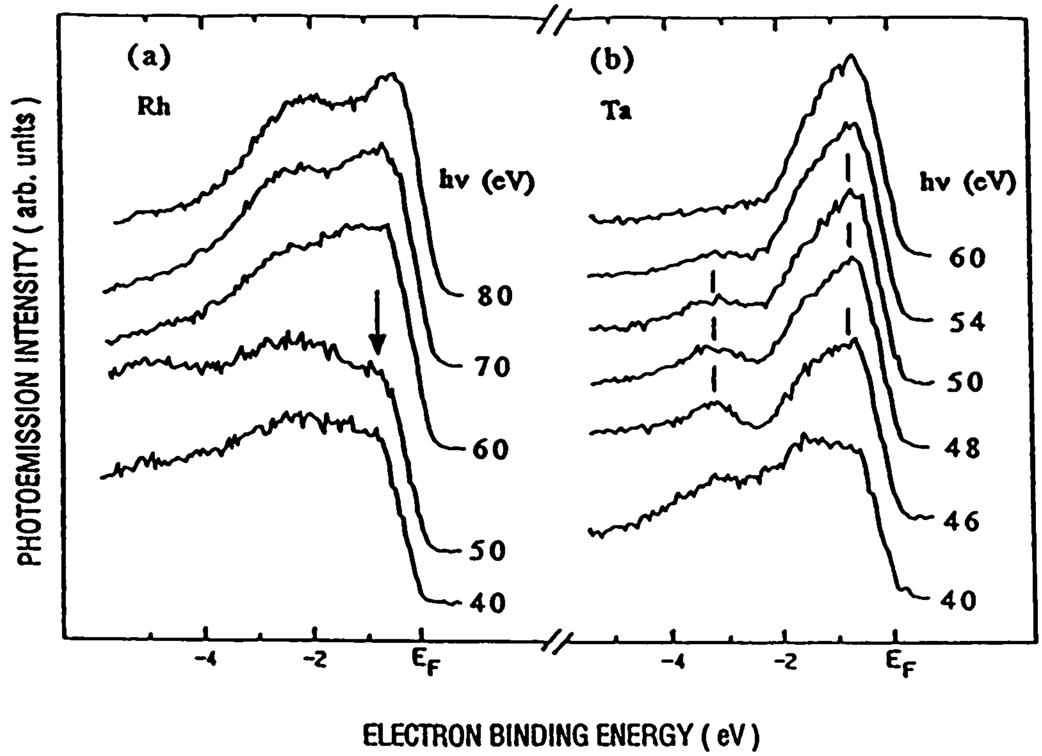

Figure 38. Photoemission spectra of (a) a thick Rh film (b) Ta(110) substrate for various photon energies.

This provides the basis for the analysis of the spectra for a Rh coverage of 1 ML [Fig. 39(a)] as a function of photon energy. The peaks near -0.8 and -3 eV are most intense between 46 and 53 eV photon energy and are therefore attributed to the Ta 5*d* states because they are strongest at the photon energy corresponding to the resonant minimum of Rh 4*d* states and the maximum of Ta 5*d* states. These two states are not as strong in the 2 ML spectra of Fig. 39(b) because they are attenuated more by the Rh overlayer. The states near -3 eV have been previously[59] assigned to a Rh-Ta interface bonding state and this is likely a mistake because its intensity does not grow with coverage in Fig. 37 up to 1 ML as expected for an interface state.

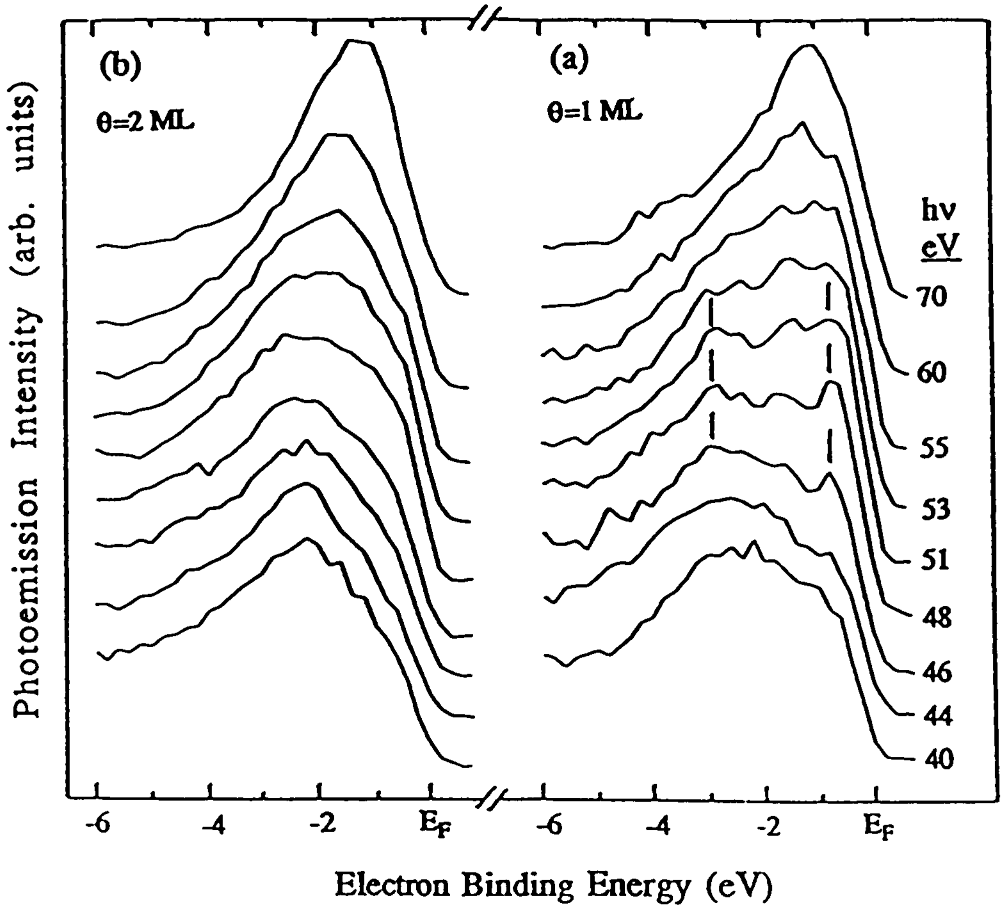

Figure 39. Photoemission spectra of (a) 1 ML (b) 2 ML Rh on Ta(110) for various photon energies.

Figure 40 shows the valence band photoemission spectra of the (2X1) and (3X1) surfaces formed by annealing 2.25 ML Rh/Ta(110) at 750 and 1000 °C respectively. The spectrum of the (2X1) surface resembles that of the unannealed surface near 1 ML coverage and is characterized by a small peak near E_F and a big peak about 2 eV below E_F. The (3X1) surface has a valence band similar to that of the unannealed surface near 0.4 ML coverage and is characterized by a Rh-derived sharp feature at -2.8 eV binding energy and the Ta-derived state near E_F.

Figure 41 shows photoemission spectra for 20-L CO exposure of Rh/Ta(110) surfaces at room temperature. Vertical lines going from higher to lower binding energy mark the CO 4σ, 1π-5σ, and the O $2p$ peaks respectively. CO dissociates on Ta(110) and molecular CO features are absent. Castner *et al.*[57] reported that CO adsorbs on Rh(111) molecularly but dissociates on stepped Rh surfaces and argue that CO should dissociate on rough Rh surfaces. Yates *et al.*[60] presented data which argue that the dissociation of CO on stepped or rough surfaces is unlikely. For our thickest Rh overlayer (10 ML) which consists mainly of Rh(111) crystallites with considerable roughness as indicated by LEED, we find only the molecular CO photoemission features and see no evidence of significant CO dissociation, and thus support Yates *et al.*. The observation of the CO 4σ feature at θ=0.6 ML, where Rh still grows in layer-by-layer mode, suggest that CO adsorbs molecularly on Rh monolayer islands covered Ta(110) surface. This differs from Pd/Ta(110) where monolayer covered surface is inert to CO adsorption at room temperature[25], and is the direct consequence of the less occupation of Rh 4*d* band which can not be filled to be noble-metal-like through the interaction with Ta. The intensity of the O 2*p* feature decreases with increasing Rh coverage. The persistence of CO dissociation to above 1.3 ML supports the conclusion of the growth characterization (particularly by LEIS) that the Ta(110) is not covered until the Rh coverage is larger than 1.5 ML (4 min). At 2.5 ML Rh coverage, where the surface is almost fully covered, the

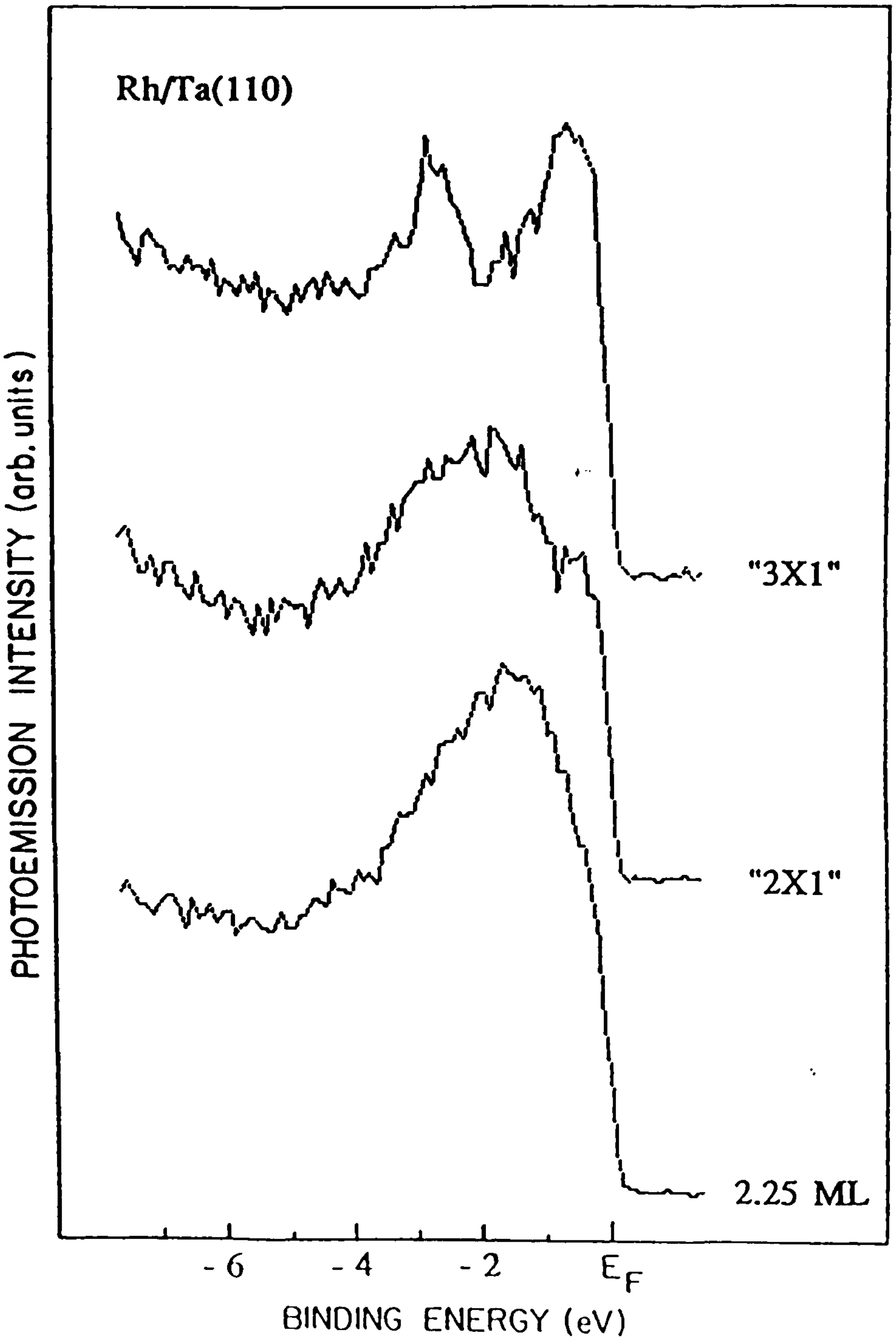

Figure 40. Photoemission spectra (hv=21.2 eV) for the (2X1) and (3X1) surfaces formed by annealing 2.25 ML Rh/Ta(110) at 750 and 1000 °C respectively.

molecular CO peaks dominate CO-related features but they are much weaker than those for the thick Rh film.

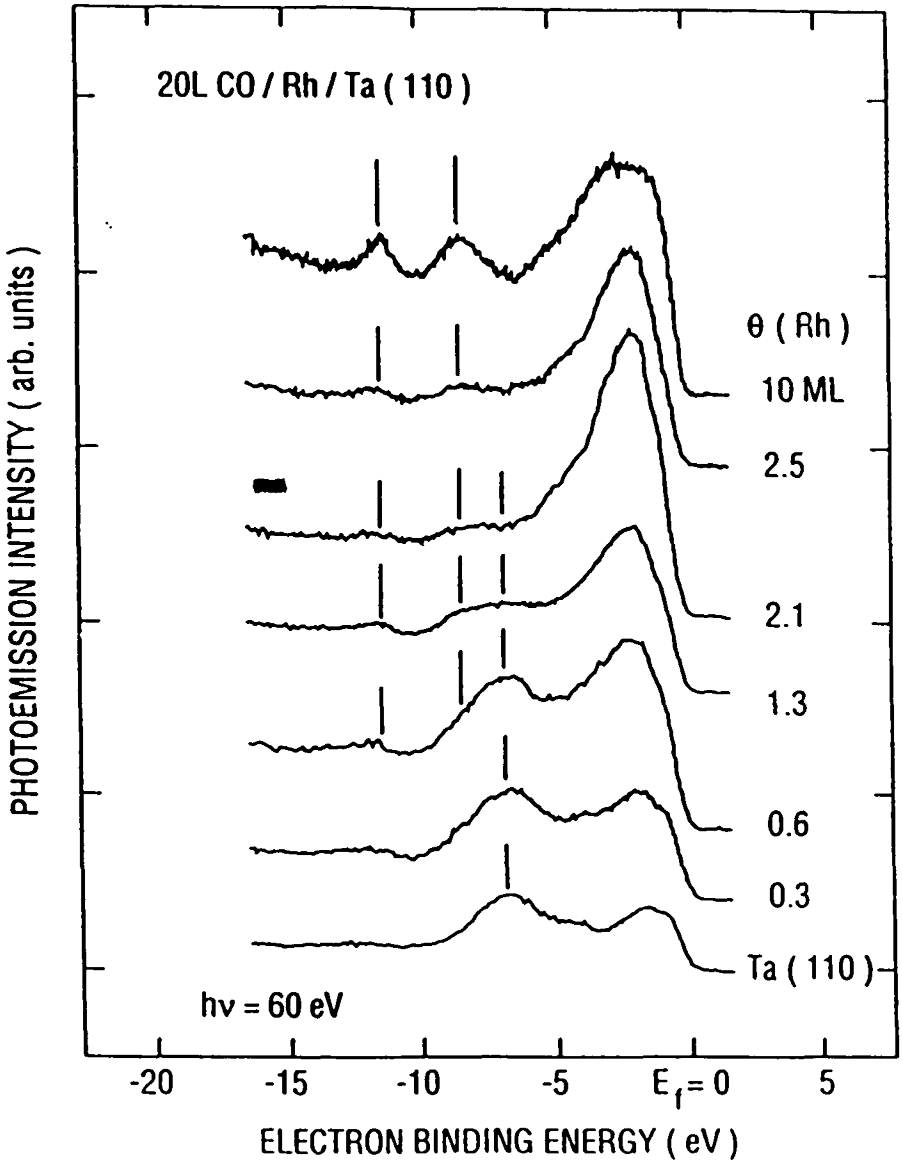

Figure 41. Photoemission spectra (hν=60 eV) for various Rh coverages on Ta(110) after 20-L CO exposure.

5.2 Atomic Structure of Rh Overlayers on Mo(110)

The Auger peak-to-peak amplitudes (AA) of Rh at 302 eV and Mo at 186 eV are shown in Fig. 42 as a function of deposition time at room temperature. The Mo AA decreases linearly with rather well defined breaks at the completion of each layer, indicating two-dimensional layer-by-layer (FM) growth of Rh on Mo(110). The Rh AA increases in a similar way, but an extra segment is seen between 0.71 and 1.14 ML. The significance of this segment becomes evident by inspection of the LEED patterns.

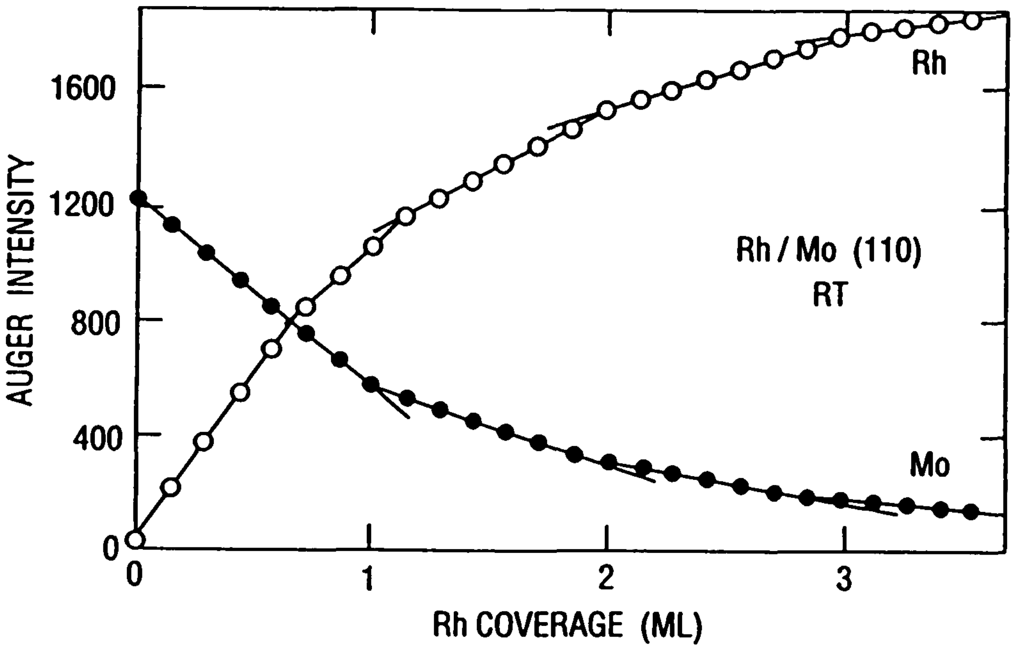

Figure 42. Rh and Mo Auger intensities vs Rh coverage.

Figure 43(a) is the LEED pattern for a clean Mo(110) substrate and Fig. 44(a) shows the real-space unit mesh of both Mo(110) and Rh(111) to serve as a reference. At Rh coverages up to 0.71 ML, the satellite LEED spots in Fig. 43(b) increase in intensity. This pattern can be derived from the real-space unit mesh shown in Fig. 44(b) and it is a distorted Rh(111) plane with Rh[$1\bar{1}0$] rows aligned with Mo[$1\bar{1}1$] rows. The interatomic distance of Rh along the Rh [$1\bar{1}0$] rows needs only a slight expansion of 1.4% to match Mo along the Mo[$1\bar{1}1$] rows and the Rh-Rh distance in the Mo[001] direction is increased so that Rh [$1\bar{1}0$] row spacing (2.329 Å) matches the Mo[$1\bar{1}1$] row spacing (2.57 Å). δ in Fig. 44(b) is found to be b/11 using the measured satellite spacing and thus Rh [$1\bar{1}0$] rows coincide with Mo[$1\bar{1}1$] rows every 11 rows. This structure was present in two equivalent orientations, Rh[$1\bar{1}0$] ‖ Mo[$1\bar{1}1$], and Rh[$\bar{1}01$] ‖ Mo[$\bar{1}11$], and is an example of the KS relationship. Figure 43(b) was obtained at 0.7 ML, followed by a 3-min anneal at 500 °C. We emphasize, however, that the unannealed surface displays essentially the same LEED pattern but with reduced spot sharpness due to the smaller island size [Fig.43(e)]. This differs from the behavior of Pd/Mo(110) studied by Park *et al.*[61] who observed the Pd(111) monolayer in the KS orientation only after annealing at 450 °C and the Pd monolayer was pseudomorphic on Mo(110) at room temperature.

For Rh coverages exceeding 0.71 ML, the LEED pattern changed to that shown in Fig. 43(c), which was taken at 1 ML. This structure can be explained by the real-space unit mesh in Fig 44(c) and Δ is found to be a/7 by using the measured beat spacing. It is a distorted Rh(111) plane with its [$0\bar{1}1$] row spacing decreased by 4.4% to match the Mo [001] rows and a slight expansion (0.34%) along the Rh[$0\bar{1}1$] row to form a 7:6 coincidence lattice in the Mo[001] direction: $(6a-7b)/6a=0.0034$, where $a=3.148$ Å and $b=2.689$ Å are the interatomic distances of Mo in the [001] direction and Rh in the [$0\bar{1}1$] direction respectively. It indicates that the orientation of the Rh(111) monolayer has transformed into the NW (-x) relationship with Rh[$0\bar{1}1$] ‖ Mo[001]. This transition leads to a rotation of the Rh(111) monolayer relative to Mo(110) substrate and also to a

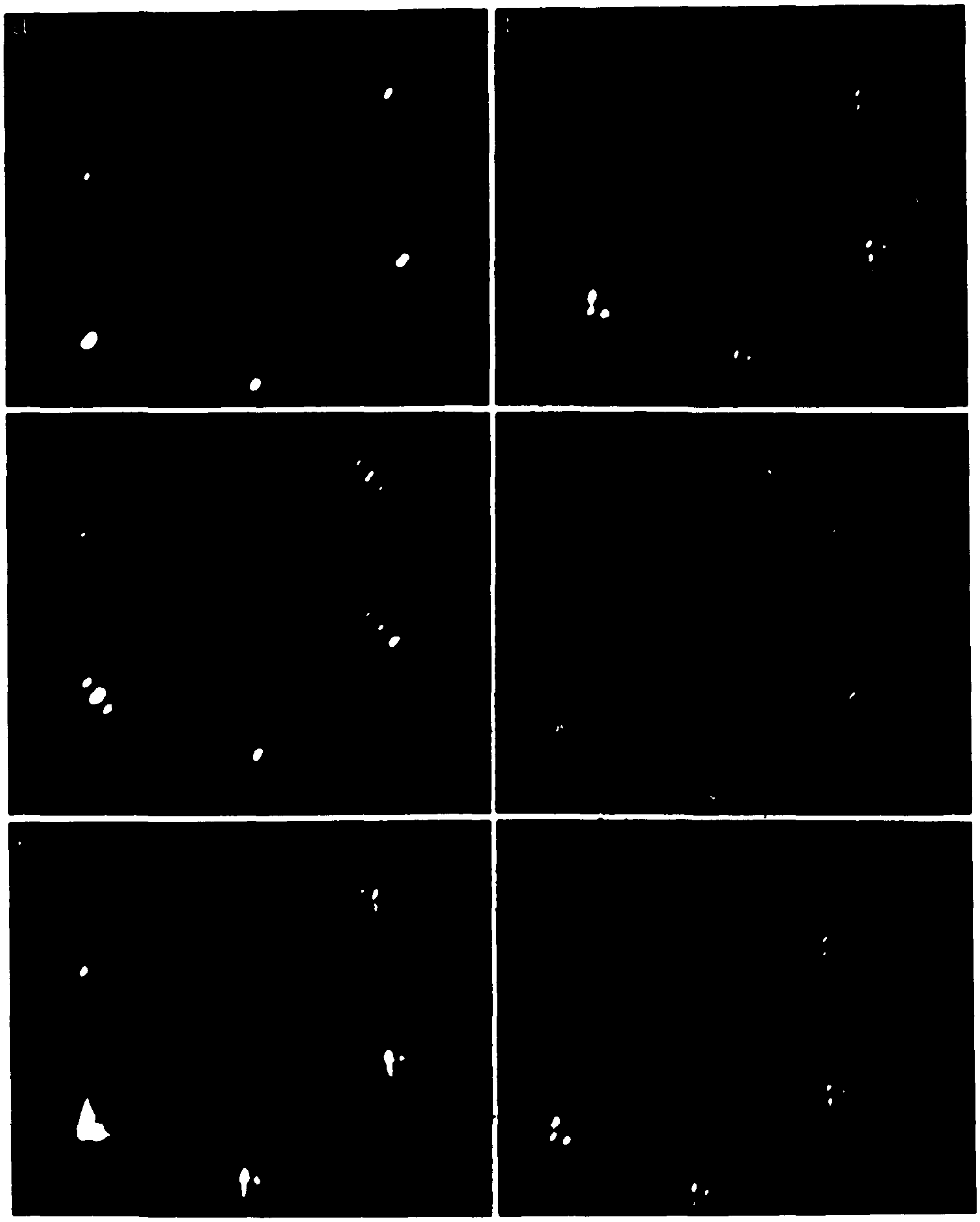

Figure 43. LEED patterns of Rh on Mo(110) obtained with 50-eV electrons: (a) clean Mo(110), RT; (b) 0.7 ML, 500 °C; (c) 1 ML, RT; (d) 3.37 ML, RT; (e) 0.7 ML, RT; (f) 3.37 ML, 900 °C.

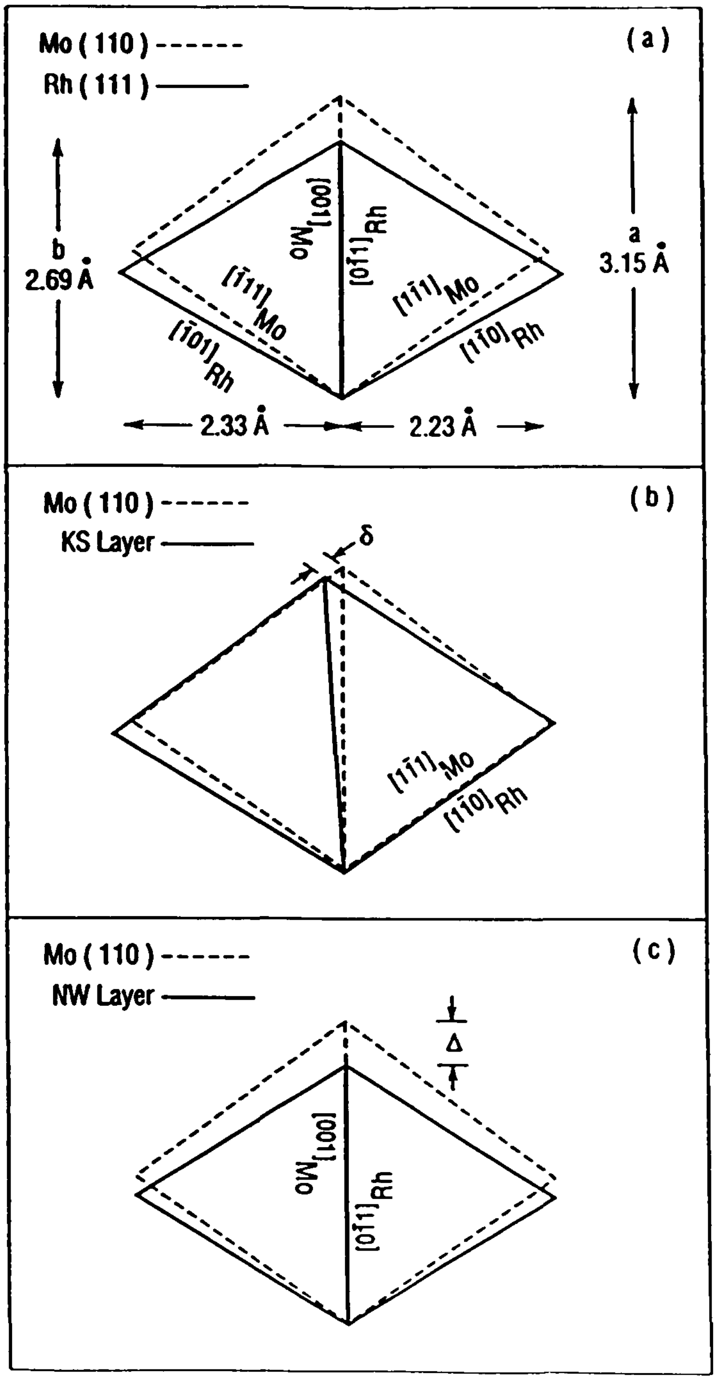

Figure 44. Real-space unit meshes of Rh overlayers in contrast to Mo(110): (a) unstrained Rh(111), (b) KS layer, (c) NW layer.

considerable reduction (14.7%) in the Rh[1$\bar{1}$0] row spacing. Thus, the extra segment in the Rh Auger uptake curve mentioned earlier coincides with the onset of a KS to NW orientation transition of the Rh(111) monolayer and the completion of Rh(111) monolayer in the NW orientation. A similar segment has been observed previously in studies of the pseudomorphic (P) to coincidence (C) transition of a Ni monolayer on W(110).[62] Although the angular distribution of Auger emission from a monolayer may be quite complicated due to the interference of side- and back- scattered electrons,[63] the major effect of the side neighbors is the forward focusing which reduces the number of Auger electrons that can reach the analyzer. The model calculations by Idzerda *et al.*[64] indicate that near-neighbor scattering results in a decrease in the slope of the first layer Auger uptake curve compared to no scattering. Since the packing density of a Rh(111) monolayer in NW orientation (NW layer) and a coincidence Ni layer are higher than a Rh(111) monolayer in KS orientation (KS layer) and a pseudomorphic Ni layer respectively, stronger scattering and forward focusing by side neighbors are expected for the former. Therefore the smaller slope of the extra segment in the first layer Auger uptake curve is consistent with the orientation transition of a Rh(111) monolayer on Mo(110) and the P-C transition of a Ni monolayer on W(110). The observation of coexistence of the two orientations of Rh(111) monolayer on Mo(110) suggests that it is a first-order structural transition. We believe this transition is caused by the increases in the intralayer forces relative to the layer-substrate interaction induced by the second-layer atoms. The mechanisms behind the orientation transition of the Rh monolayer will be discussed in more detail in section 5.4.

At higher coverages, Rh(111) continues to grow in the NW orientation and the superstructure weakens. Figure 43(d) was obtained at 3.37 ML and it exhibits mostly the usual hexagonal LEED pattern of a fcc(111) surface. The FM growth, the eventual NW orientation of Rh/Mo(110), and its small surface-energy mismatch suggest that Rh(111)/Mo(110) is a good candidate for crystalline superlattice formation. The ML defined in Fig. 42 and referred to subsequently is a monolayer in the NW orientation which has an atomic density of $1.667X10^{15}$ atoms/cm^2. It can be seen from Fig. 44(b) and 44(c) that the atomic densities of a KS layer and the Mo(110) substrate are the same and they correspond to 0.86 ML.

The thermal stability of the Rh/Mo system is studied by annealing it at different temperatures for 5 min. Figure 45 is a plot of the ratio of the Rh (302 eV) and Mo (186 eV) peaks as a function of annealing temperatures for 1.03 and 2.25 ML. The AES ratio starts decreasing above 450 °C and this is due to the agglomeration or interdiffusion of Rh layers in excess of 1 ML. The curve flattens above 800 °C, indicating the increased stability of 1 ML. The high- temperature shoulder above 1000 °C is due to the desorption of the stable monolayer which is characterized by the flat plateau in Fig. 45. The LEED pattern corresponding to this plateau region is shown in Fig. 43(f) which is essentially the same as that in Fig. 43(b). This indicates that the stable monolayer produced by heating is in the KS orientation. We found that the KS monolayer can be obtained in this way for all higher initial coverages. The fact that the KS layer obtained by annealing a NW layer will transform back into a NW layer upon the deposition of an additional small amount of Rh (0.14 ML), suggests that it is a monolayer on top of the Mo substrate, instead of a surface alloy with Mo. This observation is consistent with surface energy considerations.

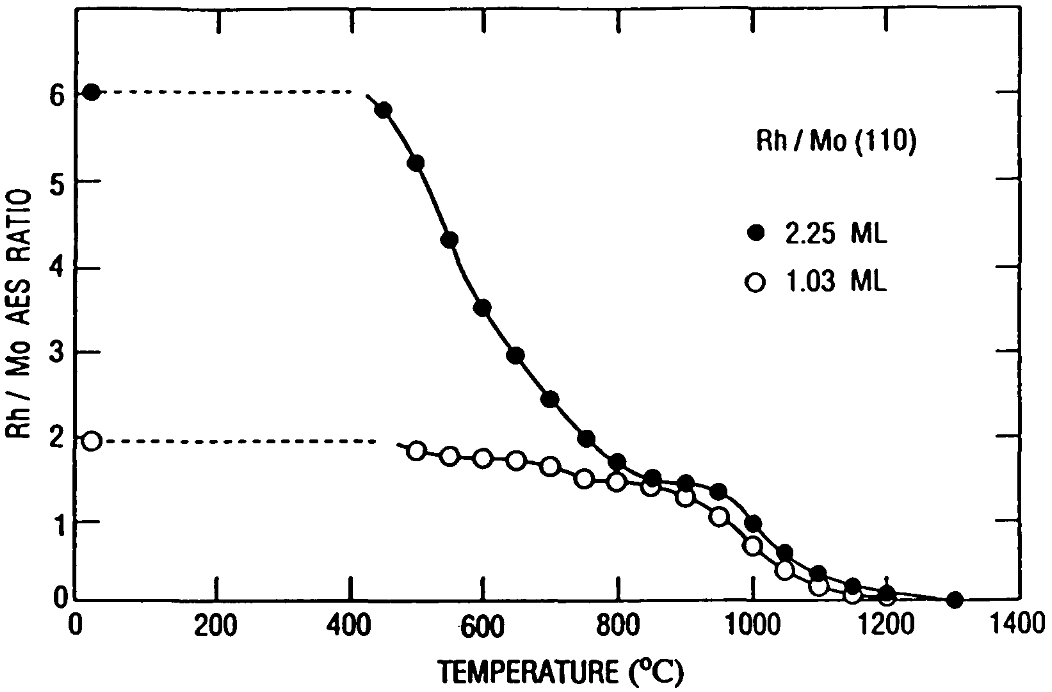

Figure 45. Thermal stability of Rh/Mo(110) showing the variation of AES intensity ratio I[Rh(302 eV)]/I[Mo(186 eV)] for 5-min anneals at each temperature for 1.03 and 2.25 ML.

5.3 Electronic Properties of Rh Overlayers on Mo(110)

Figure 46 shows the variation in work function (ϕ) with Rh coverage. For Rh/Mo(110), I=7.46 eV, A=1.14 eV, ϕ=4.95 eV, and J=-0.65 eV<0. Thus the J criterion is consistent with the initial decrease in ϕ. The fact that the work-function decrease stops at 0.3 ML and then increases, suggests that some Rh adatoms have already formed islands at coverages below 0.3 ML. This is further supported by the LEED pattern at 0.3 ML, which shows extra spots corresponding to KS islands. With further addition of Rh, ϕ increases slowly up to 0.86 ML, followed by a fast rise after the transition to the densely packed (smooth) NW layer. Consistent with uniform FM growth, ϕ saturates at coverages beyond 2 ML to 5.36 eV, which is quite close to the value for a Rh(111) single crystal.

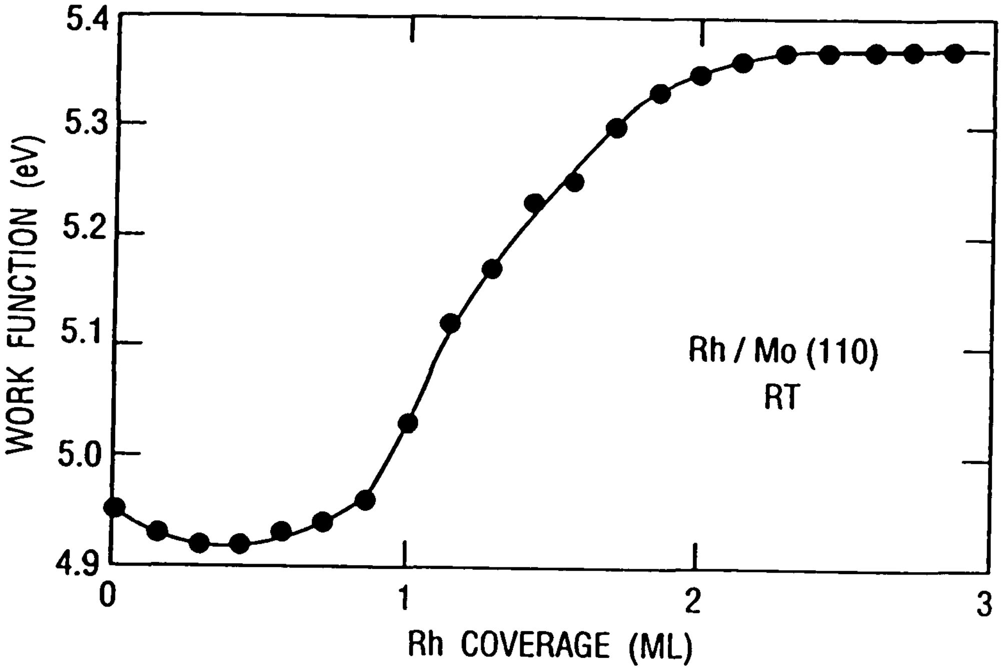

Figure 46. Variation of work function vs Rh coverage on Mo(110).

Figure 47 shows the evolution of the electronic structure for 0-4-ML Rh films on Mo(110) obtained with valence band photoemission using 21.2-eV light. All spectra were scaled to best display their shape instead of their absolute intensities. The spectrum for clean Mo(110) is characterized by three peaks at -0.3, -1.8, and -4.3 eV in general agreement with an earlier study of this surface[65]. Both Rh and Mo are near the middle of the transition-metal series, and the large overlap of their band structure makes it difficult to locate the first-and second-layer Rh-induced features from the direct photoemission. However, it can still be seen that states near -0.9 and -2.5 eV grow steadily upon the deposition of Rh up to 1 ML, and the second-layer growth develops states at -0.5 and -2.2 eV. The surface electronic structure starts to evolve into that of Rh(111) beyond 2 ML.

The most noticeable phenomenon occurs beyond 2 ML where we observe a new state emerging at -0.9 eV. Its intensity increases rapidly with coverage, without changing the energy position, and saturates at about 4 ML. This result is shown in Fig. 48 where the intensity of this state is plotted as a function of Rh thickness. It is found that the state at -0.9 eV is very sensitive to contamination and the adsorption of CO removes it. This state was not seen in the study of Rh films on Ta(110), where the overlayer is disordered. We attribute this state to a surface state(resonance). A similar surface state(resonance) at -0.7 eV has been found for a Pd(111) overlayer on Nb(110)[36] and it also commences with the deposition of a third atomic layer. The existence of surface states (resonances) on the (111) faces of late transition metals and particularly on Pd(111) has been predicted by self-consistent pseudopotential calculations[66].

The unique features of the ultrathin Rh layers are more clearly depicted in the difference spectra of Fig. 49. The attenuations are calculated using the 51% drop of the Mo Auger peak at 186 eV by 1 ML and the universal curve (Fig. 2) of the energy dependence of electron escape depths. This results in an 84% and 63% scaling of the clean Mo spectrum by 1 ML of Rh, for hv=21.2 and 40.8 eV, respectively. The second-

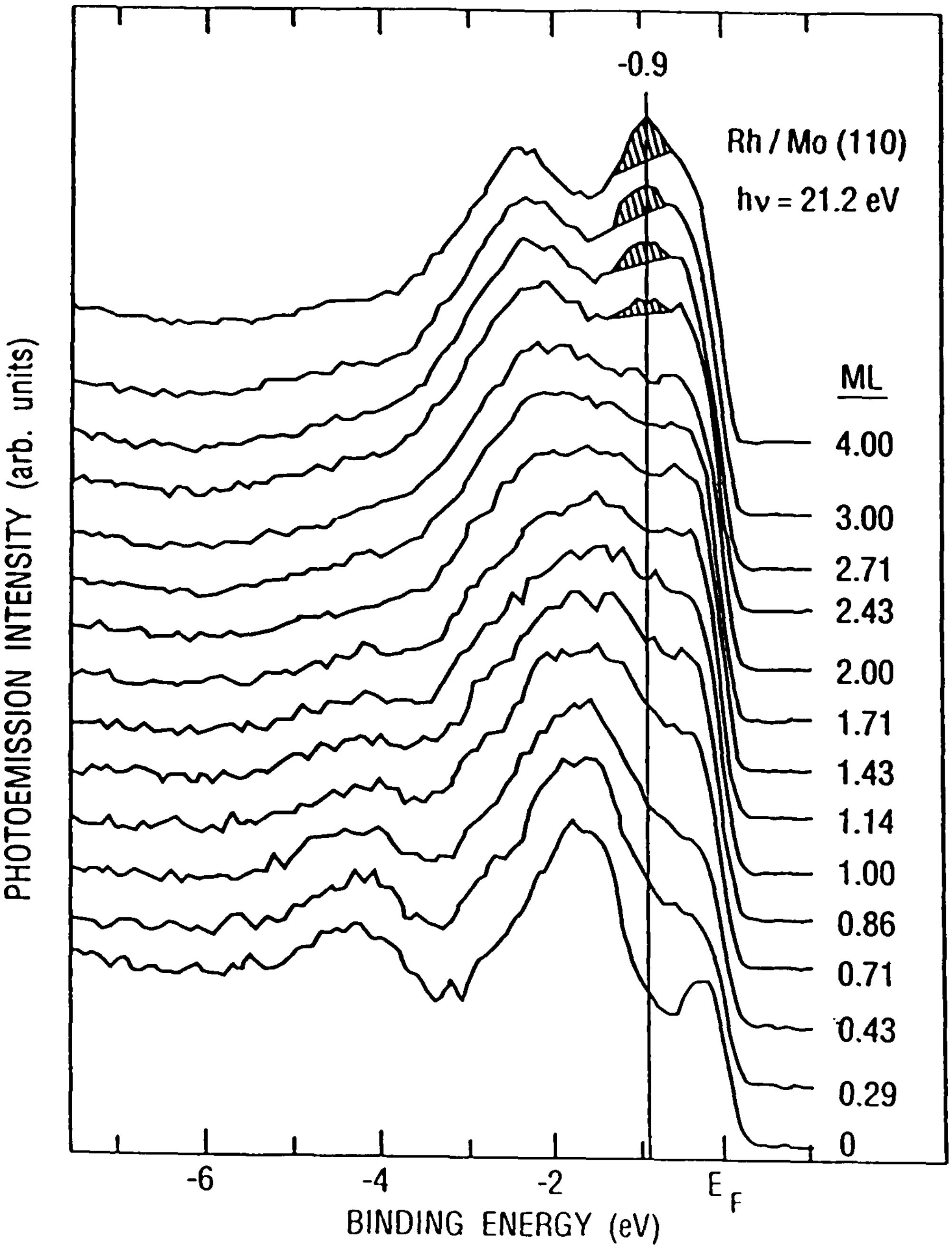

Figure 47. Photoemission spectra (hv=21.2 eV) for various coverages of Rh on Mo(110).

layer attenuation is derived in a similar way with partial monolayers attenuating the signal proportionately. Up to 1 ML, the difference curves maintain the same shape with increases in the intensities, and no abrupt change of electronic structure accompanies the orientation transition. So only the difference curves between 1 ML and the clean substrate and the difference of 1.7 and 1 ML are plotted to show the effects of the first and second layers. We mention that straight difference curves, without taking into account the attenuation, basically display the same peaks and the density of states near E_F is higher for the Rh monolayer on Mo(110) than for the bare Mo(110) surface. The spectra for hv=40.8 eV are multiplied by a factor of 5 to better compare the shape of the 21.2- and 40.8- spectra.

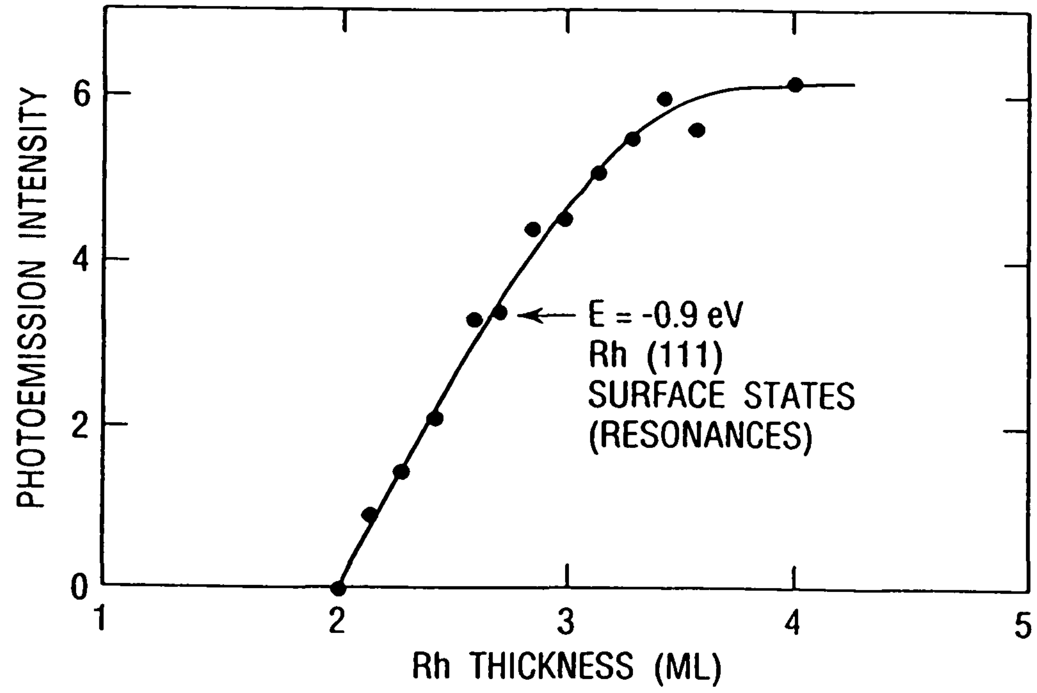

Figure 48. Photoemission intensity of the surface states (resonances) on Rh(111) as a function of thickness.

Figure 49 clearly shows that the relative intensities of peak (a) and peak (b) are reversed as the photon energy changes from 21.2 to 40.8 eV. The photoionization cross sections of Rh and Mo are 22.8 and 26.3 at hv=21.2 eV and 27.8 and 8.5 at 40.8 eV, respectively[17]. This suggests that the photoemission spectra at 40.8 eV will enhance the Rh features and reduce Mo features significantly. The intensity variation in Fig. 49 thus indicates that states (a) centered at -0.9 eV are mostly Mo derived and states (b) centered at -2.5 eV are mostly Rh derived. Second-layer growth induces three peaks (c), (d), and (e) at -0.5, -2.2, and -3.4 eV, respectively, and the density of states at E_F increases much faster than for monolayer growth. This suggests that states (b) and (a) are likely localized at the Rh/Mo interface, probably due to a bonding-antibonding pair of Rh(4*d*)-Mo(4*d*)-derived interface states.

Interface states at -1.5 and -3.5 eV have been found for Cu adsorbed on Ru(0001) and confirmed by band structure calculations which also show a 0.1-eV upward shift when Cu is moved from hcp sites to threefold hollows[67]. There are two more *d* electrons for Cu than Rh, and for Ru compared to Mo, it therefore seems reasonable that the interface states for Rh/Mo(110) are closer to E_F than are those for Cu/Ru(0001). It should be noted that a number of inequivalent sites exist for a Rh overlayer on Mo (11 for a KS layer and 7 for a NW layer) and each has a different Mo coordination. This explains part of the breadth for the Rh/Mo(110) interface states compared to those for pseudomorphic Cu on Ru(0001), which has only one site and all adatoms have the same substrate environment.

An unoccupied interface state (resonance) has been observed for Pd/Nb(110) and confirmed by band structure calculations which also identify its mostly Nb-derived character[68]. Considering the smaller *d* count of Nb compared to Mo and Ru, it is understandable that the antibonding partner of the Pd(4*d*)-Nb(4*d*) interface state is pushed up to above E_F and the bonding partner with Pd character deeper to below E_F. This results in a lower density of states near E_F for a Pd monolayer on Nb(110) than for bare Nb, and

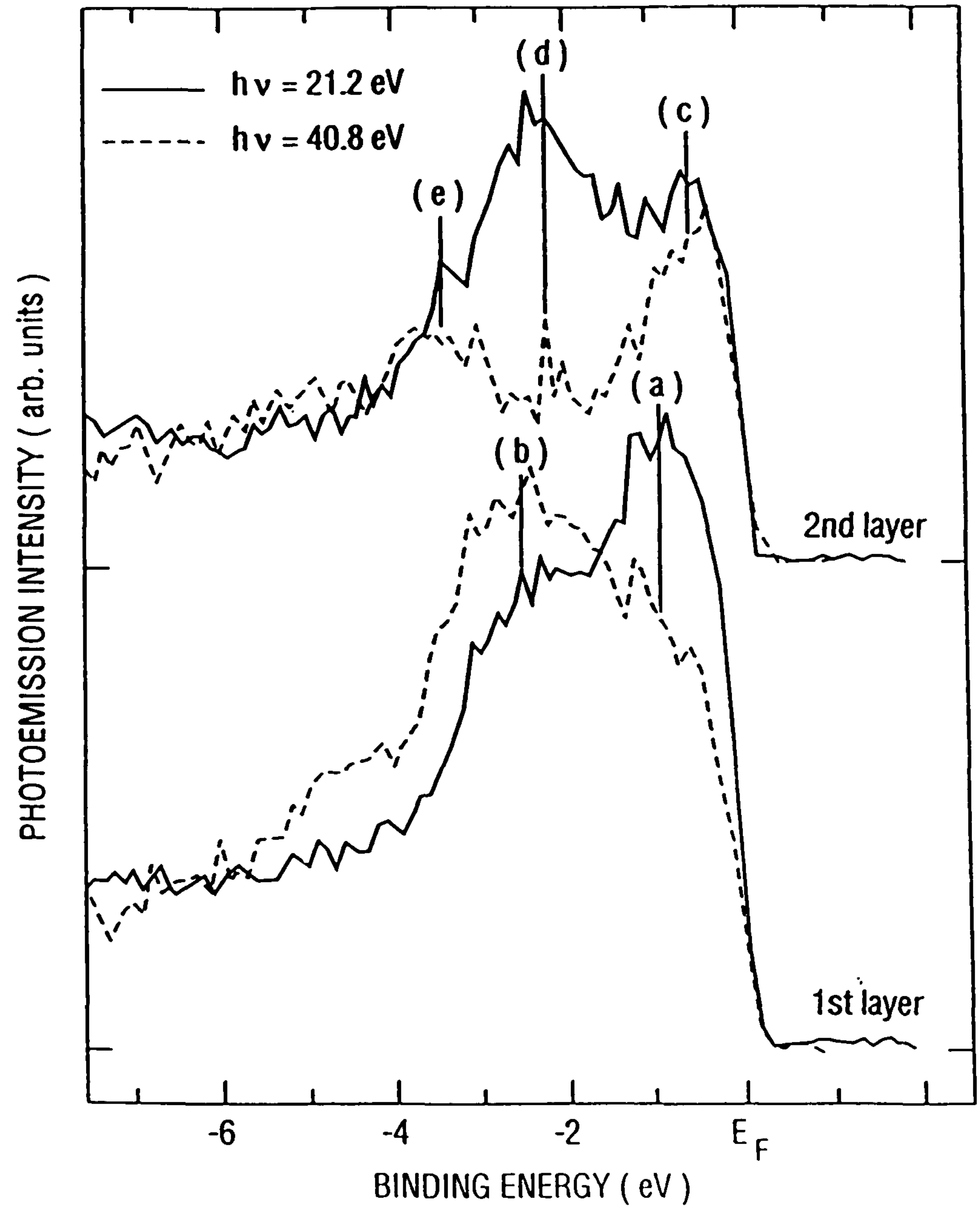

Figure 49. Difference spectra showing the contributions of the first and second layers and their variation with photon energy.

indeed this surface is found to be inert to CO at room temperature[25]. In contrast to Pd/Nb(110), the density of states near E_F for the Rh monolayer on Mo(110) is higher than the bare Mo surface and it increases faster upon second-layer growth. This is correlated to the following CO adsorption properties.

Figure 50(a) shows the effects of 20-L CO on Mo(110) and different Rh overlayers at 40.8 eV photon energy. CO dissociates into individual C and O atoms on the Mo(110) surface, and states due to the O $2p$ orbitals are clearly seen at -6.3 eV. Covering the surface with only 0.3-ML Rh already reduces the intensity of the O $2p$ states and induces peaks attributable to molecular CO, namely, the 4σ- and 1π-5σ-derived states at -11 eV and -8 eV, respectively. This differs from CO adsorption on Pd/Nb(110) where the molecular CO features appear only after the substrate is completely covered by over a monolayer of Pd. The peak heights of CO $1\pi+5\sigma$ and O $2p$ obtained by the difference curves before and after CO exposure at $h\nu=21.2$ eV are summarized in Fig. 50(b). The amount of molecular CO adsorbed on the surface increases slowly up to 0.7 ML followed by a faster rise. We believe this slope change is because the density of states near E_F increases faster for second-layer growth than for first-layer growth. Fig. 50(b) also shows that CO dissociation decreases linearly with Rh coverage and stops at 0.7 ML, just before the orientation transition.

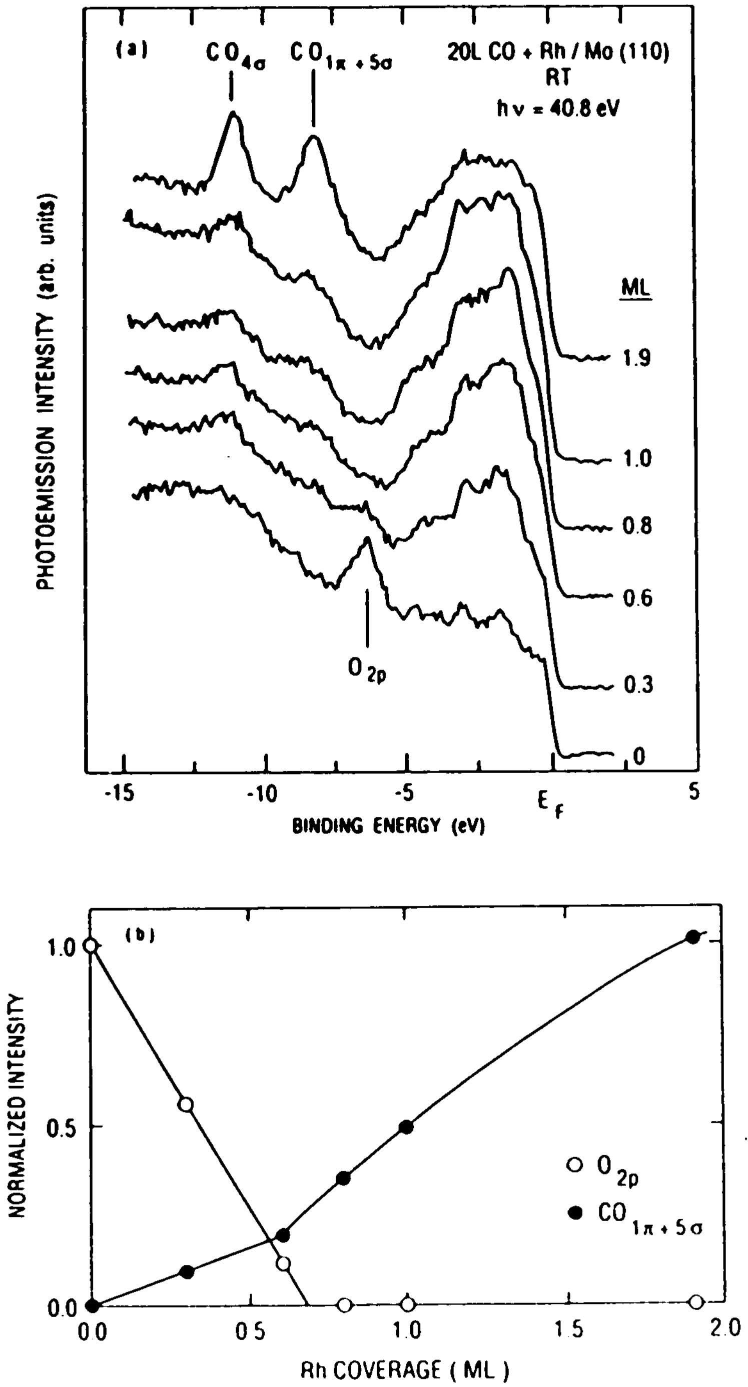

Figure 50. (a) Photoemission spectra (hv=40.8 eV) for selected Rh coverages on Mo(110) after exposure to 20-L CO; (b) normalized intensity of O 2*p* and CO 1π +5σ peaks as a function of Rh coverage on Mo(110).

5.4 On the Orientation Transition of Rh monolayer on Mo(110)

Metallic first layers are frequently observed to be pseudomorphic at room temperature, for example, Ni on W(110)[62] and Pd on Nb(110).[9] The novel behavior of a Rh(111) monolayer on Mo(110) may be related to the details of its electronic structure. Rh lies closer to the middle of the transition metal series than Pd or Ni and is more strongly bonded. In order to be pseudomorphic on Mo(110), Rh(111) has to be compressed by 4.4% along Mo[$\bar{1}$10] direction and stretched by 17.1% along Mo[001] direction. This involves considerable strain which may not be sustained by the interfacial bonding that can be achieved in a pseudomorphic layer. Interfacial bonding is stronger for a KS layer than a NW layer because the atomic rows in the KS layer pass through the substrate potential minimum while those in a NW layer do not (section 3.2). It is plausible that the higher strain energy associated with a KS layer because of its larger absolute strain compared to that of a NW layer, is compensated by its stronger bonding with the substrate, making a KS layer on Mo(110) the most energetically favorable case. In other words, the energies of a KS layer E(KS), a NW layer E(NW) and a pseudomorphic layer E(P) on Mo(110) are related as follows:

$$E(KS) < E(P) \quad \text{and} \quad E(KS) < E(NW). \tag{5.1}$$

It should be noted that anharmonic effects, which may be quite significant for the Rh-Rh interaction over the strain range discussed here, would favor (5.1) because it leads to a lower strain energy for a stretched layer compared to a compressed layer given the same absolute value of strain.

The microscopic mechanism behind the orientation transition might be similar to that suggested for the P-C transition observed for a Pd monolayer on Nb(110).[69] Although previously called a commensurate to incommensurate transition, a P-C transition might be a more appropriate notation. When the KS islands are large enough, which is more likely as the coverage approaches a monolayer, it becomes inevitable, due to limited mobility, that some Rh atoms start occupying sites in the second layer. This increases the strain of the overlayer and the bonding between first and second layer Rh atoms weakens the interaction of Rh with the Mo substrate significantly. The lateral interaction between Rh atoms then becomes more important and induces the orientation transition in the first layer to the less strained and densely packed NW layer. The second layer atoms are incorporated into the monolayer during this process. This explanation implies

$$E(2NW) < E(2KS) \text{ and } E(2NW) < E(NW/KS) \qquad (5.2)$$

where E(2NW), E(2KS), and E(NW/KS) are the energies of two NW layers, two KS layers, and one NW layer on top of a KS layer on Mo(110) respectively.

This second layer effect can be quantified by a transition from ℓ to $\sqrt{2}\ell$ (Section 3.2) in Bauer and van der Merwe's theoretical structural phase diagram (Fig. 18) which successfully predicted the structure of many fcc(111)/bcc(110) interfaces. The absence of pseudomorphic growth for Rh/Mo(110) can be explained by a large value of ℓ. The observed orientation transition is not allowed in this diagram at the atomic diameter ratio corresponding to Rh/Mo(110) (r=0.986) for any value of ℓ. This discrepancy may be due to the anharmonic effect in the intralayer interaction which is left out of the theory, or the underestimated Fourier coefficient ($A_1=A_2=0.4$) in the Fourier series used to model the layer-substrate interaction. Since the depth of energy minimum for KS orientation is proportional to A_1 and A_2, the stability limit NK would lie above DE in Fig. 18 if A_1 and A_2 were large enough, a KS to NW orientation transition then becomes possible during growth for systems such as Rh/Mo(110).

The orientation transition might also be prompted by 2D-grain boundary formation, which has been argued by Kolaczkiewicz and Bauer[62] to be the driving force for the P-C transition of Ni monolayer on W(110). Adsorption sites must have lower

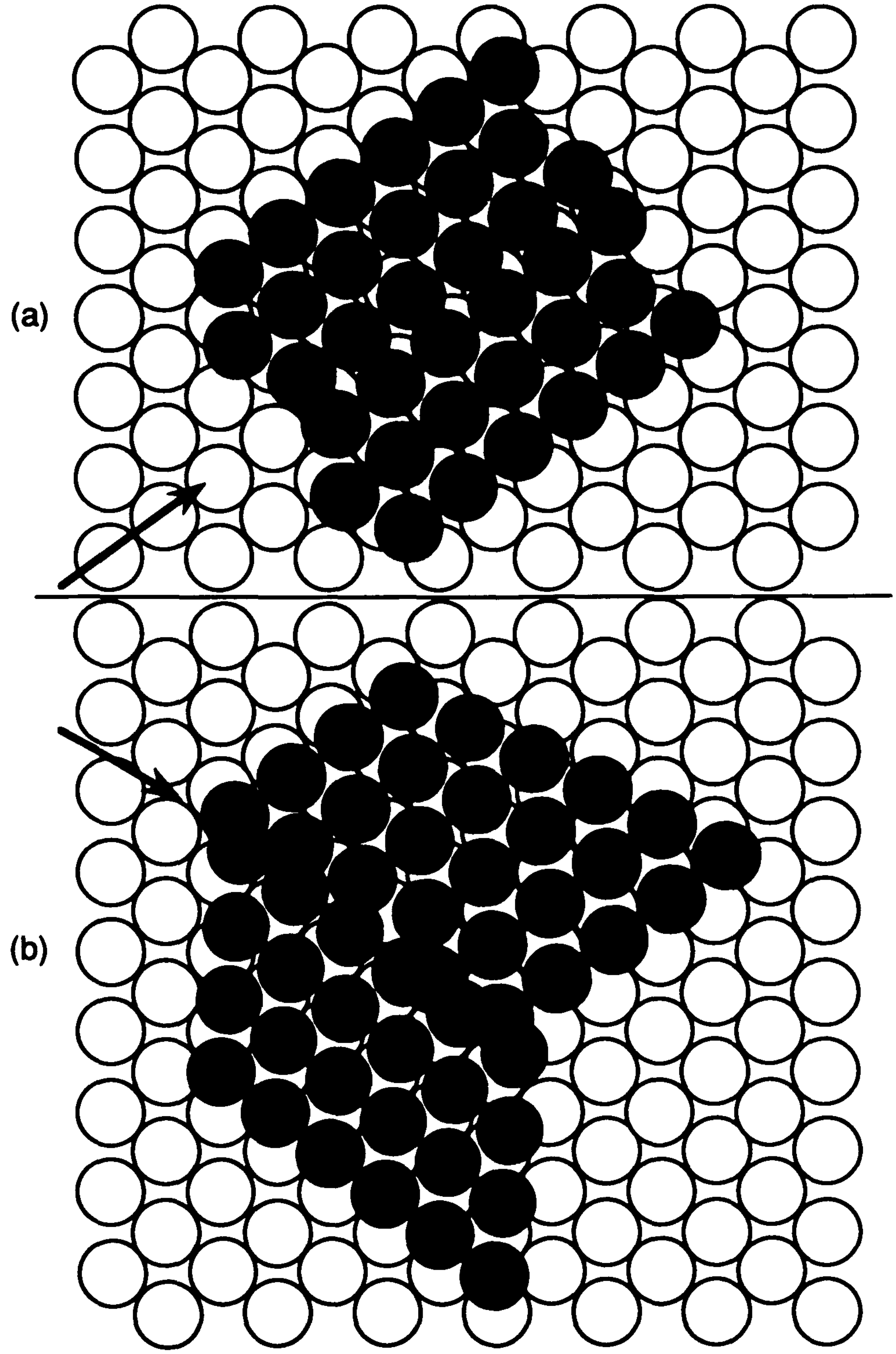

Fig. 51. Model for the grain boundary interactions between domains of (a) same (b) different KS orientations.

symmetry than normal lattice sites in order to form grain boundaries. This is the case for a KS layer but is energetically unfavorable for a pseudomorphic layer. We therefore believe that grain boundaries are more important for the orientation transition than for the P-C transition. A KS layer consists of two type of grains, one with Rh$[1\bar{1}0]$ ॥ Mo$[1\bar{1}1]$ and the other with Rh$[\bar{1}01]$ ॥ Mo$[\bar{1}11]$. The grain boundary atoms are squeezed together when the coverage is high enough so that two grains meet (Fig. 51). We argue that this causes considerable repulsion, which forces a KS layer to pack more densely and transforms it into the uniquely oriented and less strained NW layer.

Using the "mapping technique" discussed in section 3.2, the epitaxial energy can be calculated as a function of system size. The total number of atoms, N, for a circular fcc(111) island of radius R with an atomic diameter a is given by

$$N = \frac{\pi R^2}{\frac{\sqrt{3}}{2}a^2}$$

and thus

$$\frac{R}{a} = \sqrt{\frac{\sqrt{3}}{2\pi}N}\,. \tag{5.3}$$

For Rh(111)/Mo(110), r=0.986. Using the data in Table II, we have

$$\alpha_1|r-r_c| = \begin{cases} \frac{3\sqrt{3}\pi}{2\sqrt{2}}\left(\frac{R}{a}\right)|0.986-1.089| = \frac{3^{7/4}\sqrt{\pi}}{4}\,0.103\sqrt{N} = 0.31\sqrt{N}\,, & \text{KS;} \\ \frac{3\sqrt{2}\pi}{2}\left(\frac{R}{a}\right)|0.986-0.943| = \frac{3^{5/4}\sqrt{\pi}}{2}\,0.043\sqrt{N} = 0.15\sqrt{N}\,, & \text{NW.} \end{cases}$$

Taking the leading-order contribution in Eq. (3.15) and using the values of V_G in Table II, the energy difference for the Rh(111) island in KS and NW orientation can then be written as

$$\Delta E = V_{as}(KS) - V_{as}(NW) = 0.4\frac{J_1(0.15\sqrt{N})}{\sqrt{N}} - 0.51\frac{J_1(0.31\sqrt{N})}{\sqrt{N}}\,. \tag{5.4}$$

ΔE is plotted in Fig. 52 as a function of N. It can be seen that below a critical island size of 81 Rh atoms, $V_{as}(KS)<V_{as}(NW)$, and above this size, $V_{as}(KS)>V_{as}(NW)$. Thus, the KS to NW orientation transition during Rh(111) monolayer growth can be explained by this size induced crossover of epitaxial energy.

So far all the mechanisms proposed above may provide the driving force for the orientation transition during the growth of a Rh(111) monolayer on Mo(110). However, the fact that the KS layer produced by annealing a NW layer, will transform back into a NW layer upon the deposition of an additional amount of Rh, suggests that the second layer Rh atoms are more likely to be responsible for the orientation transition.

In summary, the orientation transition observed for a Rh(111) monolayer on Mo(110) is believed to be the result of increases in the intralayer forces relative to the layer-substrate interaction induced by the second layer atoms, or possibly also by the grain boundary atoms and finite-size effects. Further work is called for, and in particular, experiments capable of measuring the structure at atomic resolution as well as first principle calculations to test relation (5.1) and (5.2).

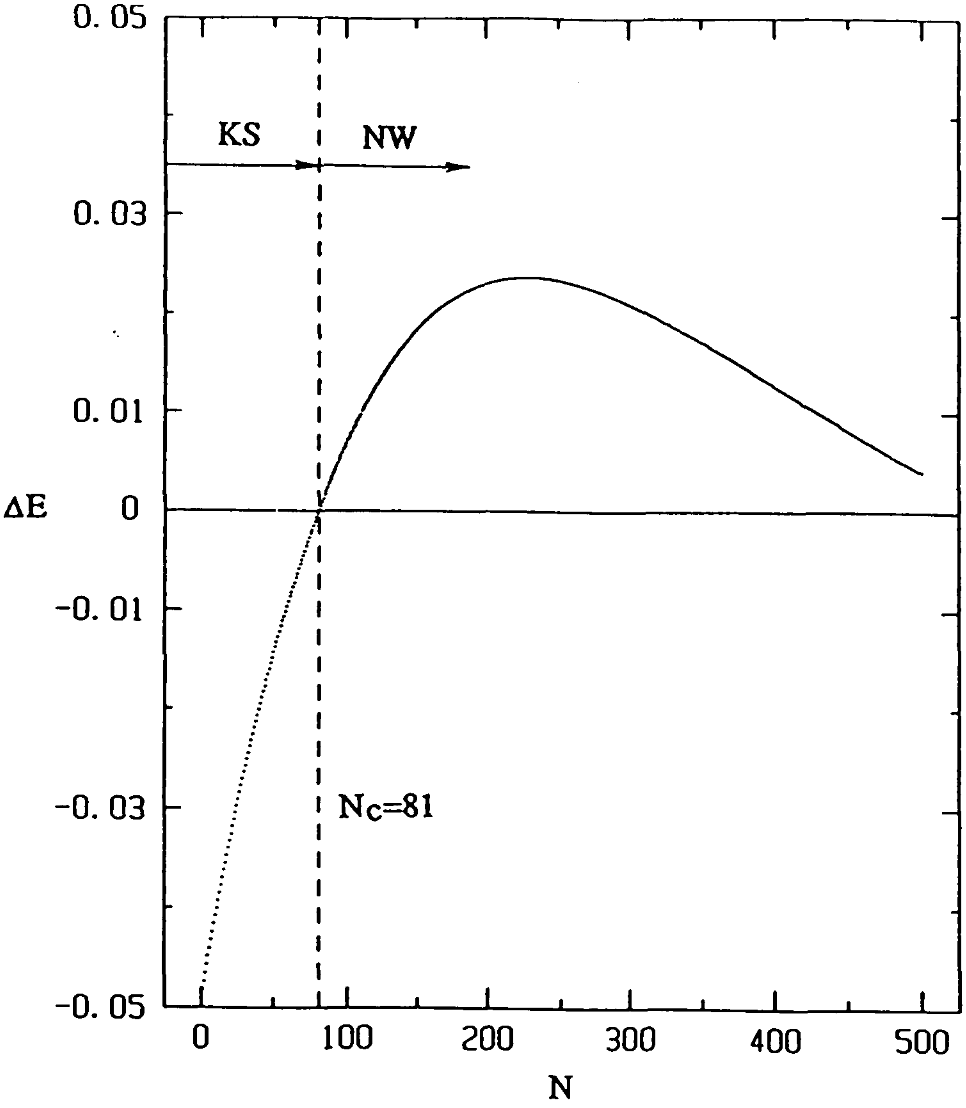

Figure 52. Energy difference for Rh(111) island on Mo(110) in KS and NW orientation as a function of island size.

Chapter 6. Summary

The growth, electronic and chemisorptive properties of several class of bimetallic interfaces have been studied using surface techniques. These studies are not only of fundamental interest in the better understanding of complex surface and interface phenomena, but also have great implications in modifying the surface for desired properties, and in the design and fabrication of artificial multilayer and superlattice materials afforded by the current MBE machines. The techniques used are mainly AES, LEED, LEIS, photoemission, and to a lesser extent, TPD. These techniques are reviewed to illustrate why and how they can be used to obtain complementary information about the composition, structure, electronic and adsorption properties of surfaces and interfaces. The catalytic activities of modified surfaces are demonstrated with a deuteration reaction of propylene (C_3H_6) and D-H exchange over Pd/Ta(110) at relatively high pressures.

The current theories of thin film growth modes and epitaxial orientations are critically reviewed. A criterion is proposed to show that the direction of electronic charge transfer between adatoms and metallic substrates is determined by the sign of $J=(I+A)/2-\phi$, where I and A are the ionization potential and affinity level of the adatom, and ϕ is the substrate work function. If $J<0$, the charge transfer will be from the adatom and a positive dipole will be formed which reduces the work function; if $J>0$ the charge transfer will be from the substrate and a negative dipole will be formed which increases the work function. This criterion is applied successfully to the understanding of the initial work function changes of the various systems studied in this thesis as well as other systems that have not been explained previously. As $(I+A)/2$ is a constant, ϕ may change with coverage until $J=0$, the value of J may roughly represent the upper limit of possible work function change. Furthermore, the maximum or minimum in the plot of work-function change versus coverage may indicate the onset of a structural transition from individual adatoms to condensed islands. These theoretical aspects provide the basis for a unified understanding of the growth modes, orientations, and the trends of initial work function changes of a vast variety of systems by the simple picture of energetics.

The studies of Pd/Al disproved the previous conclusion of SK growth for this system and demonstrated that alloying may occur even at room temperature when a high surface energy metal is grown on a low surface energy metal and the bonding of the metal pair is strong. This idea is further supported by the alloying of Nb/Pd(111), which is also understood by comparing to the first principles calculations available for this system. The dominant role of electronic effects on chemisorptive properties is shown by comparing the similar electronic structure and weakened CO adsorption of the alloy surface obtained by depositing 1 ML Nb on Pd(111) and the surface of a Pd monolayer on Nb(110). This point is further investigated by extending the study to Rh which has one less *d* electron than Pd, and supportive results are obtained concerning the trends in electronic and CO chemisorptive properties.

It is shown that Rh agglomerates on Ta(110) but grows layer-by-layer on Mo(110) which has less lattice mismatch with Rh(111). A KS to NW orientation transition has been observed for the first time during the growth of Rh on Mo(110) near 1 ML and the possible mechanisms are discussed in terms of second-layer effects, grain boundary interactions and finite-size effects. It is suggested that the increases in the intralayer forces relative to the layer-substrate interaction induced by second-layer atoms are mainly responsible for the orientation transition. However, the theories need to be further refined to correctly predict the orientation behavior of Rh/Mo(110).

Some final remarks seems appropriate. Generally the ideas of surface, interface and lattice mismatch induced distortion energies can provide guidelines concerning the growth modes including alloying. The epitaxial orientations of fcc(111)/bcc(110) interfaces can be predicted quite well based on the minimum interface energy principles in the region near the optimal atomic diameter ratio corresponding to the natural matching of atomic rows. More work is needed in order to predict the complex orientation behavior of in-between systems reliably. The chemisorptive properties are mainly determined by the surface valence band electronic structure, and are particularly correlated to the density of states near E_F which are the "frontier orbitals"[70] directly involved in the bonding and antibonding interactions. The analog of the occupied and unoccupied states near E_F of a metal are the ionization and affinity levels near the Mulliken electronegativity of an atom. The charge transfer in the adsorbate-substrate system implies that the electron affinity plays an equally important role as the ionization potential in an atom's ability to attract electronic charge and therefore should not be neglected in defining electronegativity or related concepts.

Appendix: Modeling of the TDO Measurement of $\lambda_L(0)$

This thesis work was conducted during the explosion period of the high T_c superconductors which have attracted the attention of many physicists including myself. One of the most fundamental parameters in superconductivity is the London penetration depth, $\lambda_L(0)$. Among the various methods of measuring $\lambda_L(0)$, e.g., muon spin relaxation, etc., tunnel diode oscillator (TDO) based inductance measurements are perhaps the simplest and least costly. In the TDO setup, the sample serves as a core of a solenoid whose inductance (L) changes with the penetration depth and controls the LC oscillator frequency which can be measured precisely. The details can be found elsewhere[71]. For elemental superconductors, e.g., Nb, Ta, the sample is usually a long cylinder so that

$$\delta L/L=2\pi R\Delta\lambda/A$$

where R and A are the sample radius and the flux containing area in the solenoid respectively. Since $f=1/2\pi\sqrt{LC}$, the following can be obtained,

$$\delta f/f=-\delta L/2L=-\pi R\Delta\lambda/A.$$

For high T_c superconductors, the samples are usually small compared to the solenoid and the simple relation of the inductance being proportional to flux containing area becomes more complex. I take this opportunity to present calculations for modeling this case which are crucial in order to make *quantitative* measurements of $\lambda_L(0)$.

Faraday's law requires the total magnetic flux across any plane be zero,

$$\Phi_i + \Phi_o = 0$$

where Φ_i and Φ_o are the flux across inside and outside of the solenoid respectively. The inductance is given by

$$L = \Phi_i/I = -\Phi_o/I. \qquad (A.1)$$

Thus the change in L can be found out by calculating the sample induced flux outside the solenoid which is much easy to do due to the simplified boundary. As an example, I will calculate for a spherical superconducting sample at the center of a solenoid (Fig. 53), in which case an analytical solution can be derived.

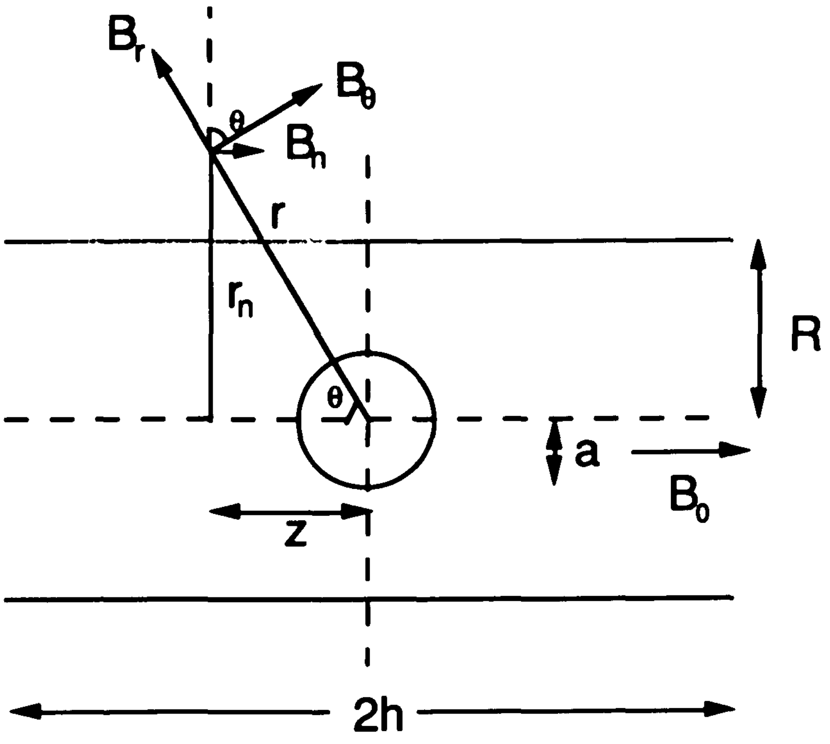

Figure 53. A spherical superconductor of radius a at the center of a solenoid of radius R and length 2h.

The magnetic field due to the superconducting sample is $\mathbf{B}_0$ inside the sphere to cancel the external field of $-\mathbf{B}_0$ due to the solenoid, outside the sphere, it is described by

$$B_r = \frac{B_0 a^3 \cos\theta}{r^3}, \qquad B_\theta = \frac{B_0 a^3 \sin\theta}{2r^3}.$$

The inductance due to the sample, L_s, can be calculated using Eq. (A.1) relative to the solenoid inductance of L_o which corresponds to the total inductance when the sample is not superconducting. Let m be the number of turns per unit length of the solenoid and neglect the edge effect,

$$\frac{L_s}{L_0} = \frac{\Phi_s}{\Phi_0} = - \frac{m \int_{-h}^{h} dz \int_{R}^{\infty} 2\pi r_n dr_n \, B_n}{B_0 \, \pi R^2 \, 2hm}$$

$$= - \frac{1}{B_0 R^2 h} \int_{-h}^{h} dz \int_{R}^{\infty} r_n \, dr_n \left(B_\theta \sin\theta - B_r \cos\theta \right)$$

$$= - \frac{1}{B_0 R^2 h} \int_{-h}^{h} dz \int_{R}^{\infty} r_n \, dr_n \left[\frac{B_0 a^3}{2r^3} \sin^2\theta - \frac{B_0 a^3}{r^3} \cos^2\theta \right]$$

$$= - \frac{a^3}{R^2 h} \int_{0}^{h} dz \int_{R}^{\infty} \frac{dr_n^2}{2} \, \frac{r_n^2 - 2z^2}{\left(r_n^2 + z^2 \right)^{5/2}}$$

or

$$\frac{L_s}{L_0} = - \frac{a^3}{R^2 h \sqrt{1 + \left(\frac{R}{h} \right)^2}} \, . \qquad \text{(A.2)}$$

Use f_0 to denote the oscillator frequency when the sample is not superconducting, we have

$$\frac{f_0}{f} = \sqrt{\frac{L}{L_0}} = \sqrt{1 + \frac{L_s}{L_0}}$$

which can be combined with Eq. (A.2) for exact analysis after multiplying L_0 by the coil correction factor to take the finite length of the solenoid into account.

Define $\Delta f = f - f_0$ and in practice, $\Delta f \ll f_0$, because $a^3 \ll R^2 h$ is usually satisfied. Thus,

$$\frac{\Delta f}{f_0} = -\frac{L_s}{2L_0} = -\frac{a^3}{2R^2 h\sqrt{1+\left(\frac{R}{h}\right)^2}}\,. \qquad \text{(A.3)}$$

Since $d\lambda = -da$, $\lambda(T) = \lambda_L(0)Z(T)$, where $Z(T)$ is a theoretical temperature dependence given by BCS or the phenomenological theory,

$$\lambda_L(0) = \frac{d\lambda}{dZ} = -\left(\frac{2R^2\, h\sqrt{1+\left(\frac{R}{h}\right)^2}}{f_0}\right)^{1/3} \frac{d(\Delta f)^{1/3}}{dZ} \qquad \text{(A.4)}$$

which enables the determination of $\lambda_L(0)$ by the measured temperature dependence of oscillator frequency. The linearity in the plot of $(\Delta f)^{1/3}$ versus Z from different models also provide an independent test of theories.

It is instructive to write (A.3) in a more general form:

$$\frac{\Delta f}{f_0} = \frac{3}{4\sqrt{1+\left(\frac{R}{h}\right)^2}}\,\frac{V_s}{V_0} \qquad \text{(A.5)}$$

where V_s and V_0 are the volume of the sample and solenoid respectively.

For other sample shapes and configurations, Eq. (A.5) serves as a starting point for an estimate. Full calculations using similar procedures can be done for an exact solution and numerical evaluation seems inevitable.

References

1. F. C. Frank and J. H. van der Merwe, Proc. R. Soc. London, Ser. A **198** (1949) 205; **198** (1949) 216; **200** (1949) 125.
2. E. Bauer and J. H. van der Merwe, Phys. Rev. B **33** (1986) 3657.
3. M. Weinert, R. E. Watson, J. W. Davenport, and G. Fernando, Phys. Rev. B **39** (1989) 12585.
4. J. G. Gay, J. R. Smith, F. J. Arlinghaus, Phys. Rev. B **25** (1982) 643.
5. P. J. Feibelman and D. R. Hamann, Phys. Rev. B **28** (1983) 3092.
6. R. M. Morra, F. J. D. Almeida, and R. F. Willis, Physica Scripta. **41** (1990) 594.
7. B. Frick and K. Jacobi, Phys. Rev. B 37 (1988) 4408; M. Xu and R. J. Smith, J. Vac. Sci. Technol. A **6** (1988) 739.
8. M. Pick, J. W. Davenport, M. Strongin, and G. J. Dienes, Phys. Rev. Lett. **43** (1979) 286.
9. M. Sagurton, M. Strongin, F. Jona, and J. Colbert, Phys. Rev. B **28** (1983) 4075.
10. M. W. Ruckman, V. Murgai, and M. Strongin, Phys. Rev. B **34** (1986) 6759.
11. D. A. Shirley in *Photoemission in Solids I*: Topics in Applied Physics Vol. 26, edited by M. Cardona and L. Ley (Springer-Verlag, Berlin, 1978) p. 193.
12. A. Zangwill, *Physics at Surfaces* (Cambridge University, Cambridge, 1988) p. 21.
13. L. J. Clark, *Surface Crystallography-An Introduction to Low Energy Electron Diffraction* (Wiley, New York, 1985) p. 13.
14. D. P. Woodruff and T. A. Delchar, *Modern Techniques of Surface Science*, (Cambridge University, Cambridge, 1986) p. 34, 223, 286.
15. W. E. Spicer, Phys. Rev. **112** (1958) 114.
16. R. H. Williams, G. P. Srivastava and I. T. McGovern, Rep. Prog. Phys. **43**, (1980) 1357.
17. J. J. Yeh and I. Lindau, At. Data Nucl. Data Tables **32** (1985) 1.
18. P. D. Johnson, S. L. Qiu, L. Q. Jiang, M. W. Ruckman, M. Strongin, S. L. Hulbert, R. F. Garrett, B. Sinkovic, N. V. Smith, R. J. Cava, C. S. Jee, D. Nichols, E. Kaczanowicz, R. E. Salomon, and J. E. Crow, Phys. Rev. B **35** (1987) 8811.
19. S. L. Qiu, C. L. Lin, L. Q. Jiang, and M. Strongin, Phys. Rev. B **39** (1989) 1958.
20. Th. Fauster, Vacuum, **38** (1988) 129.

21. O. S. Oen, Surf. Sci., **131** (1983) L407.

22. H. Niehus and E. Preuss, Surf. Sci. **119** (1982) 349.

23. P. A. Redhead, Vacuum, **12** (1962) 203.

24. K. Nagai, Surf. Sci. **176** (1986) 193.

25. M. W. Ruckman and S. Strongin, Phys. Rev. B **29** (1984) 7105.

26. P. J. Berlowitz, C. H. F. Peden, and D. W. Goodman, in *Physcal and Chemical Properties of Thin Metal Overlayers and Alloy Surfaces*, edited by D. M. Zehner and D. W. Goodman (MRS, Pittsburgh, 1987) p. 161.

27. E. Bauer, Z. Kristallogr. **110** (1958) 372; Appl. Surf. Sci **11/12** (1982) 479.

28. L. Z. Mezey and J. Giber, Jpn. J. Appl. Phys. **21** (1982) 1569.

29. M. W. Ruckman and L. Q. Jiang, Phys. Rev. B **38** (1988) 2959.

30. A. Kobayashi and S. Das Sarma, Phys. Rev. B **35** (1987) 8042.

31. H. Homma, K. Y. Yang and I. K. Schuller, Phys. Rev. B **36** (1987) 9435.

32. S. M. Paik and I. K. Schuller, Phys. Rev. Lett. **64** (1990) 1923.

33. J. H. van der Merwe, in *Chemistry and Physics of Solid Surfaces V*, edited by R. Vanselow and R. Howe (Springer-Verlag, Berlin, 1984) p. 365.

34. L. C. Allen, J. Am. Chem. Soc. **111** (1989) 9003.

35. R. Smoluchowski, Phys. Rev. **60** (1941) 661.

36. S. L. Weng and M. El-Batanouny, Phys. Rev, Lett. **44** (1980) 612.

37. J. Kolaczkiewicz and E. Bauer, Surf. Sci. **160** (1985) 1.

38. A. C. Hawson and D. M. Newns, Jpn. J. Appl. Phys., Suppl. 2 Part 2 (1974) 121.

39. R. S. Mulliken, J. Chem. Phys. **2** (1934) 782.

40. A. A. Radzig and B. M. Smirnov, *Reference Data on Atoms, Molecules, and Ions*, Springer Series in Chemical Physics, Vol. 31 (Springer-Verlag, Berlin, 1985) p87, p130.

41. R. W. Gurney, Phys. Rev. **47** (1935) 479.

42. D. L. Fehrs and R. E. Stickney, Surf. Sci. **24** (1971) 309.

43. J. P. Perdew, Phys. Rev. B **37** (1988) 6175.

44. H. B. Michaelson, J. Appl. Phys. **48** (1977) 4729.

45. X. Pan, M. W. Ruckman, and M. Strongin, Phys. Rev. B **35** (1987) 3734; X. Pan, Ph. D. thesis, City University of New York, 1987.

46. J. Colbert, A. Zangwill, M. Strongin, and S. Krummacher, Phys. Rev. B **27**, (1983) 1378.

47. R. J. Smith, A. W. Denier van der Gon, and J. F. van der Veen, Phys. Rev. B **38** (1988) 12712.

48. J. C. Fuggle, F. U. Hillebrecht, R. Zeller, Z. Zolnierek, and P. A. Bennet, Phys. Rev. B **27**, (1983) 2145.

49. J. Noffke and L. Fritsche, J. Phys. C **14** (1981) 89.

50. W. A. Harrison, *Electronic Structure and Properties of Solids* (Freeman, San Francisco, 1980).

51. C. Kittel, *Introduction to Solid State Physics*, 5th ed. (Wiley, New York, 1976).

52. F. A. Shunk, *Constitution of Binary Alloys*, 2nd ed. (Butterworths, London, 1976).

53. B. Frick, K. Jacobi, J. A. Wilder, H. J. Sagner and K. H. Frank, Surf. Sci. **193** (1988) 529.

54. D. Prigge, W. Schlenk and E. Bauer, Surf. Sci. **123** (1982) L698.

55. B. E. Koel, R. Smith, and P. J. Berlowitz, Surf. Sci. **231** (1990) 325.

56. K.C. Taylor, in Catalysis and Automotive Pollution Control, Vol. 30 of Studies in Surface Science and Catalysis, edited by A. Crucq and A. Rennel (Elsevier, Amsterdam, 1987), p. 97.

57. D. G. Castner, B. A. Sexton, and G. A. Somorjai, Surf. Sci. **71** (1978) 519.

58. H. Hochst and M. K. Kelly, Phys. Rev. B **30** (1984) 1708.

59. L.Q. Jiang, M. R. Ruckman and M. Strongin, J. Vac. Sci. Technol. A **8**(3) (1990) 2682.

60. J. T. Yates Jr., E. D. Williams, and W. H. Weinberg, Surf. Sci. **91** (1981) 562; **115** (1982) L93.

61. Ch. Park, E. Bauer, and H. Poppa, Surf. Sci. **154** (1985) 371.

62. J. Kolaczkiewicz and E. Bauer, Surf. Sci. **144** (1984) 495.

63. S. A. Chambers, S. B. Anderson, and J. H. Weaver, Phys. Rev. B **32** (1985) 4872.

64. Y. U. Idzerda, D. M. Lind, and G. A. Prinz, J. Vac. Sci. Technol A **7** (1989) 1341.

65. R. C. Cinti, E. Al Khoury, B. K. Chakraverty, and N. E. Christensen, Phys. Rev. B **14** (1976) 3296.

66. S. G. Louie, Phys. Rev. Lett. **40** (1978) 1525.

67. J. E. Houston, C. H. F. Peden, P. J. Feibelman, and D. R. Hamann, Phys. Rev. Lett. **56** (1986) 375.

68. X. Pan, P. D. Johnson, M. Weinert, R. E. Watson, J. W. Davenport, G. W. Fernando, and S. L. Hulbert, Phys. Rev. B **38** (1988) 7850.

69. V. Kumar and K. H. Bennemann, Phys. Rev. B **26** (1982) 7004; B **28** (1983) 3138.

70. R. Hoffman, Rev. Mod. Phys. **60** (1988) 601.

71. C. D. Varmazis, Ph. D. Thesis, Columbia University, 1974.